JOURNAL OF MATERIALS RESEARCH AND TECHNOLOGY 2021;13:1441–1484

Available online at www.sciencedirect.com

jmr&t Journal of Materials Research and Technology

journal homepage: www.elsevier.com/locate/jmrt

Review Article

Characterization of interfacial properties between fibre and polymer matrix in composite materials – A critical review

Silu Huang [a,**,1], Qiuni Fu [a,***,1], Libo Yan [a,b,*], Bohumil Kasal [a,b]

[a] Department of Organic and Wood-Based Construction Materials, Technische Universität Braunschweig, Hopfengarten 20, 38102 Braunschweig, Germany

[b] Center for Light and Environmentally Friendly Structures, Fraunhofer Institute for Wood Research Wilhelm-Klauditz-Institut, Bienroder Weg 54E, 38108 Braunschweig, Germany

ARTICLE INFO

Article history:
Received 2 January 2021
Accepted 26 May 2021
Available online 3 June 2021

Keywords:
Fibre reinforced polymer
Interface mechanism
Characterization methodology

ABSTRACT

Synthetic fibre reinforced polymer (FRP) composite materials have been widely used in engineering fields, e.g., civil, automotive, and aerospace industry, due to their high specific modulus and strength, corrosion resistance, and relatively high durability. The interface between fibre and polymer matrix is critical for the short-term and long-term performance of the FRP composite materials due to the shear lag stress transfer from the matrix to the fibre via their interface. This paper presents an overview of the fibre–matrix interface and interfacial properties. First, the interface mechanisms (i.e., interdiffusion, chemical bonding and mechanical interlocking) of FRP composites are discussed. Next, the methodology for measuring interfacial properties, characterizing interface morphology and chemical composition, and numerical simulations on FRP interface are introduced. Lastly, the challenges for the characterization of interfacial properties are highlighted.

© 2021 The Author(s). Published by Elsevier B.V. This is an open access article under the CC BY-NC-ND license (http://creativecommons.org/licenses/by-nc-nd/4.0/).

1. Introduction

1.1. Background

Fibre reinforced polymer (FRP) composite is a material composed of fibres as reinforcement and polymer as matrix. FRP composite materials were primarily developed for the aviation industry. In 1944, glass FRP (GFRP) composite materials were first applied in the fuselage skin of Vultee BT-15 trainer plane [1]. Since 1980s, the FRP composite materials were applied in civil engineering. They were embedded in and/or externally bonded to existing structural members such as concrete, masonry, timber, and steel to strengthen and/or rehabilitate these structures. For the mechanical properties of FRP composite materials, the fibre–matrix interface plays a

* Corresponding author.
** Corresponding author.
*** Corresponding author.
E-mail addresses: silu.huang@tu-braunschweig.de (S. Huang), q.fu@tu-braunschweig.de (Q. Fu), l.yan@tu-braunschweig.de, libo.yan@wki.fraunhofer.de (L. Yan).

[1] The two authors contributed equally to this work.

https://doi.org/10.1016/j.jmrt.2021.05.076

2238-7854/© 2021 The Author(s). Published by Elsevier B.V. This is an open access article under the CC BY-NC-ND license (http://creativecommons.org/licenses/by-nc-nd/4.0/).

List of abbreviations and symbols

FRP	Fibre reinforced polymer
GFRP	Glass fibre reinforced polymer
PP	Polypropylene
PVC	Polyvinyl chloride
RH	Relative humidity
MA	Maleated
MPS	3-(Trimethoxysilyl)propyl methacrylate
APS	(3-Aminopropyl)-triethoxysilane
MMC	Metal matrix composite
IFSS	Interfacial shear strength
ILSS	Intra-laminar shear strength
SPM	Scanning probe microscope
AFM	Atomic force microscope
SWNT	Single-walled carbon nanotube
MWNT	Multi-walled carbon nanotube
CNT	Carbon nanotube
DCB	Double cantilever beam
ENF	End-notched flexure
PLA	Poly(L-Lactic Acid)
SCF	Short carbon fibre
PEEK	Polyether ether ketone
P layer	Primary cell wall
ANN	Artificial neural networks
SVM	Support vector machines
FEM	Finite element method
DEM	Discrete element method
MD	Molecular dynamic
PCFF	Polymer consistent force field
CVFF	Consistent valence force field
AMBER	Assisted model building with energy refinement
CDM	Continuum damage model
CZM	Cohesive zone model
CFM	Coulomb friction model
RVE	Representative volume element
ECT	Edge crack torsion
SEM	Scanning electron microscope
TEM	Transmission electron microscopy
FTIR	Fourier-transform infrared spectroscopy
CT	Computed tomography
μCT	Micro-computed tomography
nCT	Nano-computed tomography
2D	Two-dimension
3D	Three-dimension
TGA	Thermogravimetric analysis
EDX	Energy dispersive X-ray spectroscopy
XPS	X-ray photoelectron spectroscopy
NMR	Solid-State Nuclear magnetic resonance
PMMA	Poly (methyl methacrylate)
PS	Polystyrene
PVA	Poly (vinyl alcohol)
GO	Graphene oxide
PRGO	Partially reduced graphene oxide
CG	Coarse-grained
P	Applied load
P_{max}	Maximum load
A	Cross-sectional area of the specimen in the in-plane shear test
E_f	Young's modulus of fibre
T_g	Glass transition temperature
G_I	Strain energy release rate in Mode I failure
G_{II}	Strain energy release rate in Mode II failure
C	Compliance of the specimen
L	Length of specimen in edge crack torsion test
B	Width of specimen in edge crack torsion test
L_{eff}	Thickness of the polymer adopted by nanoparticles
D	Average diameter of the particle cluster
V_{total}	Volume of particle cluster
$V_{polymer}$	Volume of the adopted polymer by nanoparticles
M_{sample}	Sample mass
H	Hardness of the material
E_r	Reduced elastic modulus
A_c	Contact area of the indenter
S	Unloading stiffness
$\mathbf{C_0}$ and $\mathbf{C}$	Stiffness matrix before and after the degradation, respectively
F_{1+}, F_{1-}, F_{2+} and F_{2-}	Damage activation function
G_N	Strain energy release rate
X_T and Y_T	Tensile strength in fibre direction and normal to the fibre direction
G_{Ic} and G_{IIc}	Critical energy release rate in mode I and mode II
S_L and S_T	Longitudinal and transverse shear strength, respectively
E_1, E_2, ν_{12} and G_{12}	In-plane elastic orthotropic properties (elastic modulus, major Poisson's ratio and shear modulus) of a unidirectional lamina
$\boldsymbol{H}$	Compliance tensor
R and l_e	Radius of the fibre and the embedded fibre length, respectively
E_{pot}, E_{bond}, E_{angle}, $E_{dihedral}$, $E_{vdWaals}$ and $E_{Coulomb}$	Potential energy of the total system, PCFF bond, PCFF angle, PCFF dihedral effect, van der Waals interaction and Coulombic interaction, respectively
d_f	Fibre diameter
l	Fibre embedded length
n	Fabric number in FRP laminated composite
s	Symmetry of fabric sequence in FRP laminated composite
d_f	Fibre diameter
l_c	Critical length of fibre
l_1	Overall length of the dog-bone shaped sample in fibre fragmentation test
w_1	Overall width of the dog-bone shaped sample in fibre fragmentation test
l_2	Gauge length of the dog-bone shaped sample in fibre fragmentation test
w_2	Gauge width of the dog-bone shaped sample in fibre fragmentation test
r	Roughness factor

b	Specimen width of specimen in short and double beam shear test
t	Specimen thickness of specimen in short and double beam shear test
a_0	Length of the pre-crack
a	Delamination length
m_1 and m_2	Compliance calibration coefficients
h	Half of the specimen thickness in edge crack torsion test
m_3 and m_4	Linear regression constants
n_{anc}	Number of anchoring points per chain in a composite
$w_{polymer}$	Mass fraction of polymer
h_{max}	Maximum indentation depth
h_f	Residual depth
h_c	Contact depth
h_{in}	Indent depth
d_i	Scalar damage parameter
$d_{int.}$	Damage parameter of the fibre/matrix interface
$E^{int.}$ and $E^{f.}$	Elastic modulus of the interface and fibre, respectively
$\nu^{int.}$ and ν^{f}	Poisson's ratio of the interface and fibre, respectively
d_f, d_m and d_s	Damage parameter of fibre breakage (longitudinal direction) and matrix cracking (transverse direction) and shear failures, respectively
d_f^t, d_f^c, d_m^t and d_m^c	Damage parameters of fibre in tension, fibre in compression, matrix tension and matrix in compression, respectively
d_N	Damage parameters ($N = 1\pm$, $2\pm$ and 6 represent the longitudinal, transverse and shear damage, respectively)
r_M	Internal variable ($M = 1+, 1-, 2+$ and $2-$) defining the threshold of the elastic domains was used to determine d_N
$f_M(r_M)$	Function having the same order as the damage activation function to indicate the initiation of softening
g_N	Energy dissipated per unit volume
l^*	Characteristic length of the finite element
l_e	Embedded length of CNT
τ_m	Shear stress on the matrix
τ_f	Shear stress on the fibre
σ_f	Tensile stress in a fibre
$d\sigma_f$	Tensile stress in a fibre element
dx	Length of a fibre element
$\gamma_{int.}$	Interface energy
$\gamma_{reinf.}$	Reinforcement surface energy
γ_{matrix}	Matrix surface energy
$\beta_{int.}$	Adhesion energy between reinforcement and matrix
θ	Contact angle at the interface
τ_{FFT}	Interfacial shear strength in fibre fragmentation test
σ_f	Fibre tensile strength
τ_{Pull}	Interfacial shear strength in fibre pull-out test
τ_{FPT}	Interfacial shear strength in fibre push-out test
σ_e	Average axial stress of the fibre
δ	Displacement of the fibre end in fibre push-out test
τ_{IPST}	Shear strength of in-plane shear test
τ_{SBST}	Interfacial shear strength of short beam shear test
δ_f	Load point deflection in the fracture toughness test
β	Constant for the indenter geometry
ε_i, $\varepsilon_{n,i}$ and $\varepsilon_{u,i}$	Normal strain, softening onset strain and ultimate strain in the softening process of element i
$\theta_{Gausspoint}$	Gauss point of elements
$\tilde{\sigma}_{11}$, $\tilde{\sigma}_{22}$ and $\tilde{\sigma}_{12}$	Effective stress tensors
$\tilde{\sigma}_{12}^m$and $\tilde{\sigma}_{22}^m$	Effective stress tensors with the fibre misalignment
η^L	Longitudinal friction coefficient
$\tilde{\tau}^T$and $\tilde{\tau}^L$	Effective longitudinal and transverse shear stress, respectively
α_{11}, α_{22} and β_{11}, β_{22}	Coefficients of thermal expansion and hygroscopic expansion in the longitudinal and transverse directions, respectively
ΔT and ΔM	Differences of temperature and moisture content, respectively
$\sigma_n$andδ_n	Cohesive traction vector (and displacement separation vector
$\sigma_c$and δ_c	Maximum cohesive traction and maximum separation, respectively
δ_0	Separation point
σ_1, σ_2, δ_1 and δ_2	Maximum cohesive tractions and separations in bi-linear cohesive laws
τ	Shear stress in friction model
σ_c	Normal pressure stress of interface in friction model
μ	Friction coefficient
σ_{d1}, σ_{d2}, and σ_{d3}	First, second and third principal stress of the droplet, respectively
σ_d	Yield strength of the droplet
τ_{fd}	Shear stress between the fibre and matrix droplet
ΔE	Difference in total energy of the CNT–epoxy
r_{CNT}	Radius of CNT
τ_i	Interfacial shear strength between CNT and epoxy

crucial role as the stress is transferred between fibre and matrix through their interface.

Therefore, this review mainly focuses on this critical issue: interface between fibre and polymer matrix in FRP composite. The mechanisms (i.e., interdiffusion, chemical bonding and mechanical interlocking) of FRP interface are introduced. The methods to improve the interfacial bonding based on the mechanisms are referred briefly. The characterization methods of FRP interface, as well as various simulation approaches of FRP interface are introduced and discussed.

Table 1 – Tensile properties of selected fibres with polymer matrices [7–13].

Material			Tensile strength (MPa)	Tensile modulus (GPa)	Elongation at break (%)	Density (g/cm^3)	Ref.
Synthetic fibre	Organic	Aramid-Kevlar	2300–3400	55–143	1.5–4	1.44–1.47	[7]
		Aramid-Twaron	3000	79–123	2–3.3	1.44	[7]
	Inorganic	E-glass	2000–3500	70	2.5	2.5	[8]
		Standard carbon	4000	230–240	1.4–1.8	1.4	[8]
Natural fibre	Plant-based	Sisal	507–855	9.4–28	2–2.5	1.3–1.5	[9]
		Hemp	550–1110	58–70	1.6	1.5	[9]
		Flax	345–1830	27–80	1.2–3.2	1.5	[9]
		Coir	131–220	4–6	15–30	1.2	[9]
	Animal-based	B. Mori silk	600–700	12.2	30–35	1.3–1.38	[10]
		Spider silk	1300–2000	30	19–30	1.3	[10]
		Chitosan	45.9–48.4	3.1–6.1	6.6	1.1	[11]
	Mineral-based	Basalt	1850–4800	70–110	2.5–3.5	2.5–2.9	[12]
		Brucite	900	13.8	–	2.4	[13]
Polymer matrix		Polypropylene	26–41	0.95–1.77	15–700	0.90–0.92	[8]
		Polystyrene	25–69	4–5	1–2.5	1.04–10.6	[8]
		Epoxy	35–100	3–6	1–6	1.1–1.4	[8]
		Polyester	40–90	2–4.5	2	1.2–1.5	[8]
		Vinyl ester	69–83	3.1–3.8	4–7	1.2–1.4	[8]

Challenges in the study of FRP interface are also summarized. For the chemical bonding, the interfacial bonding can be enhanced with coupling methods, using silane and maleated agents, which has been reviewed comprehensively in literature [2–5] and will not be discussed in this review.

1.2. *Introduction to the FRP composite materials*

For FRP materials, fibres usually exhibit higher modulus and strength than the polymer matrix, as shown in Table 1 Therefore, the mechanical performance (e.g., tensile and bending stiffness and strength) of the matrix can be improved when fibres are added. The functions of fibres include 1) carrying most of the tensile or compressive load applied on an FRP sample, and 2) bridging cracks in matrix and mitigating the growth of cracks through dissipating the energy near the crack tip. As shown in Fig. 1(a), when an FRP sample is subjected to an axial tensile load, the stress is transferred to the fibre through the surrounding matrix. In the figure, τ_m and τ_f are the shear stress acting on matrix and fibre, respectively. The σ_f and $d\sigma_f$ are the tensile stress in a fibre and a fibre element with length of dx, respectively. The process begins at the deformation of matrix caused by the applied load. Then, the matrix deformation induces shear stress at the fibre/matrix interface [6]. The tensile stress of fibre is activated to balance the shear stress. Through this process, the fibre carries most of the tensile load applied on the FRP composite. The mechanism of fibre bridging is illustrated in Fig. 1(b). Micro-cracks initially occur in polymer matrix due to its smaller fracture strain than that of fibres. The crack propagates when the strain energy near the crack tip is larger than the energy to form a new surface. If fibres are bridging a crack in the matrix, the stress carried by the matrix is transferred to the fibre via the interface. As the stress increases, the interface failure (e.g. fibre pull-out and interface debonding) or fibre fracture will occur depending on the interfacial shear strength of fibre–matrix and tensile strength of fibre. The interface failure and fibre fracture dissipate the strain energy near the crack tip, hence leads to the mitigation of crack propagation.

Conventional fibre materials in FRP include natural and synthetic fibres. As illustrated in Fig. 2, natural fibres can be further categorized into plant, animal and mineral-based

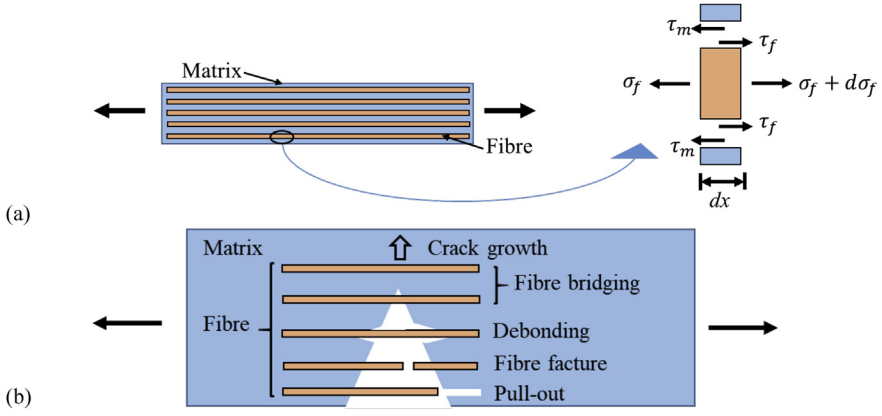

Fig. 1 – Schematic view of unidirectional FRP composites: the mechanisms of (a) load transferring at fibre/matrix interface and (b) fibre bridging, redrawn from Refs. [6,14] (Permission granted).

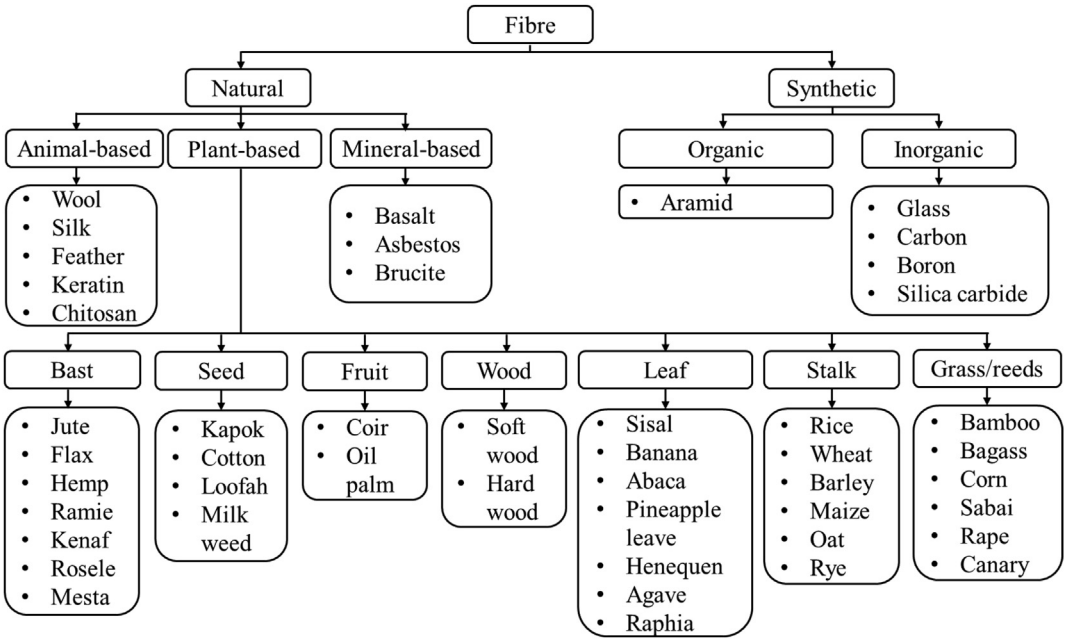

Fig. 2 – Classification of natural and synthetic fibres, redrawn from Ref. [15] (Permission granted).

fibres. Synthetic fibres are classified into organic and inorganic fibres. The forms of fibres in FRP can be divided into four main categories: monofilament short fibre, continuous unidirectional fibres, woven fabric, and non-woven mat. Table 1 presents the mechanical properties of some conventional fibres in comparison with some commonly used polymer matrices. Apart from properties of fibres, the orientation of fibres relative to loading direction also influences the mechanical properties (e.g., tensile modulus and strength) of FRP. Ideally, FRP is regarded as isotropic material in-plane if short fibres are randomly distributed in the matrix. The composite will have main tensile load-carrying directions which are same to the main fibre directions in the matrix.

The function of the polymer matrix in FRP composite materials includes holding the reinforcements together, transferring load, distributing loads evenly, carrying inter-laminar shear, and preventing fibres from direct contact with different environmental conditions.

Polymer matrices can be classified into thermoplastic and thermosetting materials. Upon heating, the cured thermosetting polymers do not melt. However, they can be pyrolyzed when they are heated to a high temperature. For example, at 300 °C, ortho-phthalic is pyrolyzed [16] to 82.6% of solid residues 6.1% of gas yields, and 9.7% of liquid (mainly aromatic compounds) yields by weight. In contrast, thermoplastic polymers melt under certain temperatures normally between 150 and 250 °C above the glass transition temperature (e.g., the melting point of polypropylene is between 160 and 175 °C [17]) and harden again when polymers are cooling down. The most widely applied thermoplastics are polyethylene, polypropylene (PP), polyvinyl chloride (PVC), and polystyrene [18]. Thermoplastic matrices are advantageous in terms of recyclability due to their ability to be remoulded [19], as well as high toughness and large resistance to microcracking [20]. However, the melting point of thermoplastic polymer limits the temperature range of the applications. Besides, the mechanical properties (e.g. tensile modulus and strength) of thermoplastic polymer are normally lower than those of thermoset [21]. This is because the linear molecular chain of thermoplastic polymer (shown in Fig. 3(a)) can be easily stretched when a load is applied. In contrast, thermosetting polymers such as epoxy, polyester and vinyl ester have a more stable molecular structure (crosslinks in Fig. 3(b)) compared to thermoplastic polymers. Therefore, they can work in higher load and temperature than thermoplastic.

1.3. *Significance of fibre/matrix interface*

Interface in FRP is the common boundary between fibre and the polymer matrix, through which the load can be transferred from matrix to fibres based on the strain compatibility. If the interface prematurely fails, the deformation (or strain) of the matrix is not compatible with that of the fibre, which results in that the load cannot be transferred from the weak component (matrix) to the strong component (fibre). In other words, the

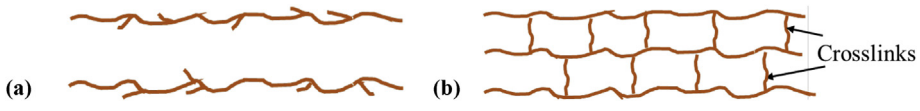

Fig. 3 – The structure of (a) thermoplastic polymer and (b) thermosetting polymer, redrawn from Ref. [22] (Permission granted).

reinforcing effect of fibres on polymer matrix cannot be achieved. Therefore, the strain compatibility at the interface is essential to the integrity of FRP materials. However, the strain compatibility is hard to be achieved under stressed and/or aggressive environmental conditions due to the different mechanical (e.g. elastic modulus) and physical properties (e.g. swelling ratio) of fibres and the matrix. Stress concentration occurs more likely at the interface than in fibres or matrix so that microcracks are easier to be generated at the fibre/matrix interface. As the microcracks propagate, the load-carrying capacity of the FRP composite material reduces. In order to make a good use of FRP material, it is essential to study the fibre/matrix interfacial properties. Furthermore, the fibre/matrix interface is critical for the long-term mechanical properties of FRP under aggressive environmental conditions. For example, when FRP composite is exposed to a high humidity environment (e.g., 95% RH), the deterioration of mechanical properties of the entire FRP is the result of the degradation of fibres, matrix, and fibre–matrix interface. The hydrolysis takes place in the matrix and/or fibre (i.e., specifically plant-based natural fibre) to cause the mechanical properties degradation of fibres and matrix. The transported moisture deteriorates the interfacial bonding through reducing the chemical bonds and mechanical interlocking at fibre/matrix interface. Besides, the differential swelling between fibre and the matrix induces microcracks at their interface [23,24]. During a long-term exposure in high humidity conditions, the microcracks formed by the swelling mismatch in the early stage of exposure provide new paths for moisture diffusion and hence accelerate the damage growth in fibres, matrix, and fibre–matrix interface. The hydrolysis of synthetic fibres is relatively insignificant in comparison with plant-based natural fibres. However, there still exists the hydrolysis of the matrix as well as the mismatch of fibre/matrix interface caused by the different swelling ratios, which can influence the short- and long-term mechanical properties of the synthetic FRP.

2. Interface in FRP

2.1. *Mechanism of the interface*

As shown in Fig. 4, at macro-scale, the interface is a common boundary between the reinforcement (fibres in FRP composite) and the polymer matrix. At micro-scale, this "boundary" is a transition region (named as interphase) with finite volume extending zone, where the chemical, physical and mechanical properties vary continuously or in a stepwise manner from the reinforcement to matrix materials [25]. According to the interphase definition, a fibre in FRP composite can be divided into two parts. One part does not contact the matrix and remains the properties of original fibres. The other part of the fibre is affected by the matrix and the properties differ from the original fibre. This difference in the properties has two origins: the first one is the treatment or adsorbed materials on the reinforcement or matrix before forming the composite. Surface treatments of fibres can add/remove functional groups to/from the original surface. Hence the fibre surface presents chemical and structural difference from the original fibre. When the fibres or matrix are exposed to the air before the assembling, the adsorption of chemical species in the air may occur at the surface to alter/eliminate certain surface reactivity, and then results in the decrease of the interfacial bonding [26]. The second cause is related to the diffusion or chemical reaction between fibres and matrix, which is discussed in the inter-diffusion, chemical bonding, and reaction bonding in the interface mechanisms.

The mechanisms of forming an interface in composite materials include physical attraction between electrically neutral bodies, molecular entanglement, inter-diffusion, electrostatic attraction, chemical bonding, reaction bonding, and mechanical bonding [26], as shown in Fig. 5. Besides, there are also some low energy forces such as hydrogen bonding and van der Waals forces. In the process of forming interfacial bonding, before the reinforcement and matrix contact each other, the physical attractions (including electrostatic attraction and physical attraction between electrically neutral bodies) may first take place. After the contact of reinforcement and matrix, other mechanisms like molecular entanglement and inter-diffusion start to operate. The final bonding between the reinforcements and matrix is formed by all the mechanisms working separately or most likely collaboratively [28]. The individual bonding mechanisms are introduced in Fig. 5 and discussed in detail below.

The physical attraction between electrically neutral bodies forms the interfacial bonding through the interactions of electrons at an atomic scale. This interaction is dependent on van der Waal forces, i.e. the attraction in neutral molecules or atoms. It may also depend on the acid-based interaction, i.e. the polar attraction of Lewis acids and bases, e.g. electron-

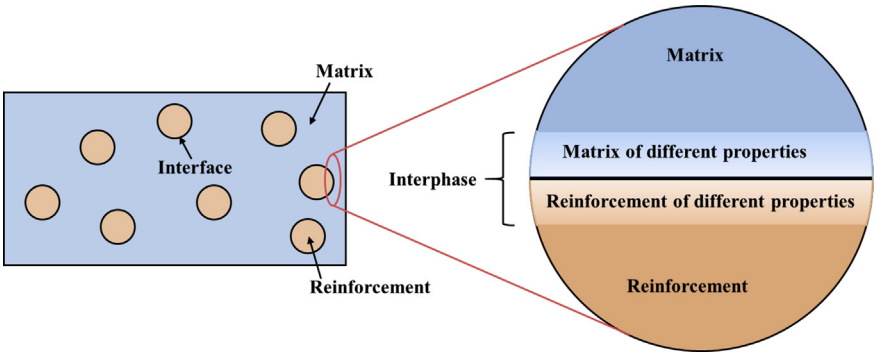

Fig. 4 – Schematic illustration of the interphase in the composite, redrawn from Ref. [27] (Permission granted).

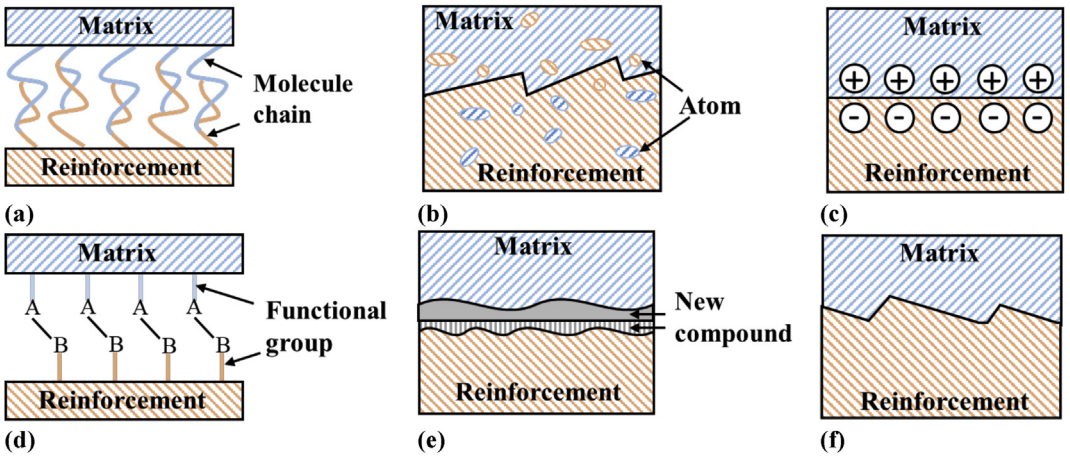

Fig. 5 – Interfacial bonding formed by (a) molecular entanglement; (b) inter-diffusion of elements; (c) electrostatic attraction; (d) chemical reaction between groups on reinforcement and matrix surfaces; (e) chemical reaction forming of a new compound, particularly in metal matrix composite (MMC); (f) mechanical interlocking, redrawn from Ref. [28] (Permission granted).

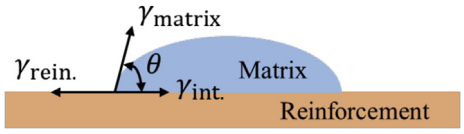

Fig. 6 – Contact angle and surface energy.

poor and electron-rich elements [29]. The interaction takes place only when the distance between atoms of the fibre and matrix is within several atomic diameters [28]. The wettability (the ability of liquids to spread on the solid surface) is usually used to characterize this physical attraction [28]. Based on Dupré equation [28], the thermodynamic work is used to describe the wettability of matrix (liquid) to reinforcement (solid). The relationship between the interface energy ($\gamma_{int.}$), reinforcement surface energy ($\gamma_{reinf.}$), matrix surface energy (γ_{matrix}), and adhesion energy between reinforcement and matrix ($\beta_{int.}$) is given by:

$$\gamma_{int.} = \gamma_{rein.} + \gamma_{matrix} - \beta_{int.} \quad (1)$$

According to Young's equation [28], for a liquid drop on a solid shown in Fig. 6, the surface and interface energies are also related to the contact angle at the interface θ, as shown in Eq. (2):

$$\gamma_{rein.} = \gamma_{int.} + \gamma_{matrix} \cos\ \theta \quad (2)$$

Substituting Eq. (2) into Eq. (1), the adhesion energy can be calculated by Eq. (3) given below. As the contact angle decreases from 180° to 0°, the adhesion energy increases, which indicates an increase of wettability between matrix and reinforcement:

$$\beta_{int.} = \gamma_{matrix}(1 + \cos\ \theta) \quad (3)$$

Wenzel [30] modified Young's equation by inducing the roughness factor (r) based on the assumption that grooves on the rough surface is completely filled by liquid. The roughness factor is defined as the ratio of the area of the actual rough surface to the smooth surface. The modified Young's equation is presented as:

$$\gamma_{rein.} \cdot r = \gamma_{int.} \cdot r + \gamma_{matrix} \cos\ \theta_r \quad (4)$$

where θ_r is the contact angle at a rough surface.

Increasing the wettability between fibre and polymer is a basic approach to enhance the interfacial bonding. There are many methods to increase the wettability. For example, corona and plasma treatments on fibre surface can increase the surface wettability through increasing carboxyl and hydroxyl groups on the surface. The increase of carboxyl and hydroxyl groups on fibres leads to the higher surface energy of fibres, $\gamma_{rein.}$ in Eq. (1) [31], hence resulting in higher interface energy.

The inter-diffusion in FRP interface indicates that the atoms and molecules of fibre material diffuse into polymer material at their interface, based on the thermodynamic equilibrium between fibres and matrix. Choi-Yim et al. [32] detected the diffusion of silicon from the silicon carbide particle to the metallic matrix by scanning Auger microscope. In the aspect of polymer matrix composite, Wolff et al. [33] observed the diffusion layer between the polymerized glass fibre and the matrix through laser scanning microscope. Moreover, the gradual change of the elastic modulus through the fibre–matrix interface (measured by nanoindentation) is regarded as an evidence of the interdiffusion between the matrix and relatively stiffer fibre. The diffused molecules can be further entangled with other molecules. The molecular entanglement can be influenced by the ambient temperature [28]. As the temperature increases, the molecules in polymer chains obtain enough energy to overcome local barriers (e.g., the interpenetration of molecule chains) which hinder molecular motions. When the temperature is close to the glass transition temperature (T_g, i.e. the temperature above which molecules have more relative mobility and polymers change from a glassy or crystalline state to a rubber state), molecular motion becomes so active that even the molecular

entanglement cannot effectively restrict the slippage of molecule chains [34]. Hence, as the molecular entanglement is unravelled gradually, the interfacial bonding is weakened.

Electrostatic attraction occurs when there is a difference in electrostatic charge between fibre and matrix surfaces due to an imbalance of electrons or ions, as shown in Fig. 5(c). The interface strength is dependent on the charge density [28]. The electrostatic attraction can work when materials are separated and the active distance is the order of centimetres, which is greater than the range of other adhesion mechanisms [35]. As aforementioned, the interaction based on van der Waal forces can only act within a distance of several atomic diameters. However, when materials are in intimate contact, the electrostatic effect is relatively weaker in comparison to van der Waals forces [36].

A chemical bonding at the interface is formed by the connection of compatible chemical groups between the reinforcement and the matrix. One common way to enhance chemical bonding is using coupling agents, which are bifunctional molecules when one end of the molecule can react with the compatible chemical group on fibres and the other end can react with the compatible chemical group of the matrix. Conventional agents include silane agents and maleated coupling agents. For silane agent, one end of silanes can react with hydroxyl groups (hydrophilic groups) of the plant-based natural fibre; the other end reacts with the hydrophobic groups in the matrix [9]. Maleated (MA) agents are commonly grafted to polypropylene (PP) [9]. In the fibre reinforced MA-PP composite, as shown in Fig. 7, there is a C–C bond formed by the MA agent and the polymer matrix. The other end of MAPP can react with the hydroxyl groups on fibre. When FRP composites with coupling agents are applied in practical environments such as hygrothermal and ultraviolet conditions, the function of coupling agents is affected by the environment as well. For example, Han et al. [37] investigated the interfacial adhesion between the polypropylene and hemp fibres treated by silane agents under ultraviolet ageing. In the comparison of silane agents of 3-(Trimethoxysilyl)propyl methacrylate (MPS) and (3-Aminopropyl)-triethoxysilane (APS), the fracture strains of the composites decreased by 35.2% and 8.0% after 8-week ageing, respectively. This is because the ester group in MPS absorbed ultraviolet radiation and get degraded leading to the relatively brittle failure of interfacial bonding. Therefore, an appropriate coupling agent needs to be selected according to the applied condition of FRP. Moreover, Pape and Plueddemann [38] summarized the modifications on silane coupling agents to improve the interfacial bonding. The modification methods included increasing hydrophobic character, crosslinking of the siloxane structure, thermal stability, and forming ionomer. These approaches can improve the resistance of the interface against the moisture and thermal degradation in hygrothermal environments. However, it should be pointed out that it is inherent that different chemical environments could affect different ends of the linking molecule under the coupling agent addition. Thus, further research regarding the influence of various environments (e.g., seawater and acid rain) on the function of coupling agents at the fibre–matrix interface is needed.

Reaction bonding is producing a new compound at the interface, which usually occurs at metal matrix composite (MMC) materials. This is simply discussed here. Due to the imbalance of thermodynamic systems, most MMC systems have a chemical potential gradient across the reinforcement–matrix interface [40]. Therefore, when fibres are in a liquid metal matrix under sufficient temperature, there will be intensive chemical reactions at the interface to yield reaction products. For example, at 500 °C, in boron fibre-reinforced aluminium composite material, aluminium diboride is formed at the interface [41].

The mechanical interlocking occurs between the matrix and rough surface of the fibre. The roughness of fibre surface could be the regular or irregular valleys, protuberance, and crevices of fibre surface [42]. When the surface is rougher, the bond area between matrix and fibre increases, and hence, the bond strength can be higher. Except for the roughness of fibres, the residual clamping stress caused by the difference in the thermal expansion or shrinkage between fibres and matrix is also beneficial for the fibre/matrix mechanical interlocking [28]. Grafting nanoparticles (e.g., nanoclay and nano carbon tube) to fibres can make the fibre surface rougher to enhance the mechanical interlocking. For plant-based natural fibres, alkali treatment is the commonly used approach to increase the mechanical interlocking of plant-based FRP composite materials. Plant-based natural fibres have fat and wax components which make the fibre surface smooth and have a negative effect on the interlocking. Alkali solution can remove the fat and wax to make the fibre surface rougher. Therefore, the mechanical interlocking can be improved. After the alkali treatment, grafting nanoparticles to the plant-based natural fibre can further increase the roughness and surface wettability of the fibre surface to enhance the interfacial bonding. The graphene oxide (GO) nanoparticle has gained popularity in the research regarding plant-based natural fibre composite, as it can not only provide the merits of nanoparticles but also show good chemical reactivity due to its intrinsic functional groups [43]. The active chemical reactivity can lead to the reaction between GO and fibre as well as between GO and matrix to form chemical bonding [44,45], which can improve the interfacial bonding significantly and further increase other mechanical properties e.g. tensile strength. Javanshour et al. [45] found the GO treated flax fibre reinforced epoxy composite showed 43% higher interfacial shear strength compared with the untreated flax/epoxy composite. Sarker et al. [43] reported that grafting GO onto jute fibres led to the improvement of 236% and 96% in the interfacial shear strength and tensile strength of jute/epoxy composite, respectively. Importantly, water molecular in the interface is a critical factor affecting the mechanical interlocking. Acting as a lubricant, water in the interface would lead to the aggravation of the slip between the fibre and matrix. On the other hand, the fibre and matrix have different shrinkage and swelling ratios. Increasing moisture content can reduce the residual clamping stress on the interface caused by the difference in the shrinkage between the fibre and matrix [46].

2.2. *Failure modes*

The failure modes of the interface can be categorized into three types according to the failure location: debonding

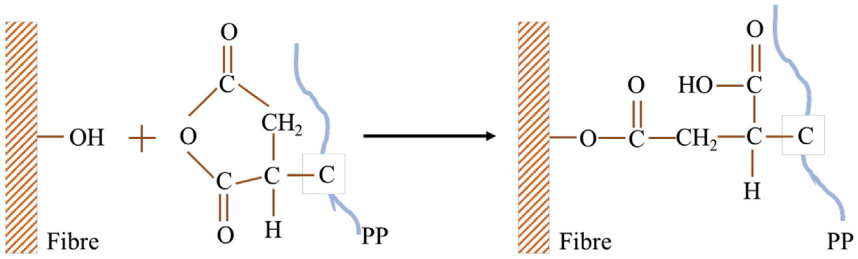

Fig. 7 – Reaction of MAPP with plant-based natural fibre, redrawn from Ref. [39] (Permission granted).

failure, failure in reinforcement, and failure in matrix, as shown in Fig. 8. These failure modes can occur individually or simultaneously depending on the bond strength, critical strength of the fibres (e.g., tensile strength in pull-out test and compressive strength in push-out test), and shear strength of the polymer matrix. For example, Oushabi et al. [47] reported that due to the incompatibility between the raw date palm fibre (hydrophilic) and polyurethane matrix (hydrophobic), the only failure mode observed was debonding failure (Fig. 9(a)) at the fibre–matrix interface under the single fibre pull-out test. When the raw date palm fibre was treated by 5 wt% NaOH, there was more matrix attached to the fibre surface as shown in Fig. 9(b). This phenomenon was attributed to that the alkali treatment leads to hydroxyl groups on the fibre surface to expose to the matrix [47]. The polymer chains of the matrix can hence form chemical bonds to the fibre surface and increase the bond strength. Liu et al. [46] also observed the debonding failure and matrix failure at the interface between the epoxy matrix and the palm fibre with different moisture contents. When there was a high moisture content (328%) in palm fibres, the debonding failure occurred. The water in the fibre/matrix interface reduced the fibre/matrix mechanical interlocking. In contrast, as the moisture content decreased, the bond strength of the palm fibre and the epoxy increased, and the failure happened at their interface and/or the matrix. The fibre failure at the interface can be observed in Fig. 9(c), which shows the tensile fracture surface of the short Napier grass fibre/polyester composite. The Napier grass fibre is fibrillated, and the fibrillation can lead to the lateral deformation of fibre resulting in the interface failure.

2.3. *Characterization of fibre/matrix interfacial properties*

Interfacial properties of FRP are characterized as interfacial shear strength (IFSS) between the fibre and polymer matrix. When it comes to laminated FRP composite materials, the intra-laminar shear strength (ILSS) and fracture toughness can be used to evaluate the relative interfacial properties as well. The characterization methods of interfacial properties are introduced in this section. Morphology observation and chemical analysis approaches are also discussed here to help in understanding the interfacial mechanism.

2.3.1. *Mechanical tests*

Mechanical tests for characterizing the interfacial properties in the composite can be classified into three types depending on the testing scale: 1) nano-, 2) micro-, and 3) macro-scale. Nano-scale measurements are usually conducted through pull-out of a nano-fibre or nanoparticle by the probe in a scanning probe microscope (SPM) or atomic force microscope (AFM). Micro-scale mechanical measurement includes fibre fragmentation test [49], single fibre pull-out test [46,50], and fibre push-out test [51]. Macro-scale mechanical measurement includes 45° in-plane shear test (ASTM D3518 [52]/ISO 14129 [53]), short beam shear test (ASTM D2344 [54]/ISO14130 [55]), and fracture toughness test (ASTM D5528 [56]/ISO 15024 [57] and ASTM D7905 [58]/ISO 15114 [59]). These test methods will be discussed individually. Some studies on the interfacial properties using mechanical tests are listed in Table 2. In these tests to obtain interfacial properties, the tests at nano-scale are mainly conducted on carbon nanotube. The embedded length of a nanotube sometimes is underestimated

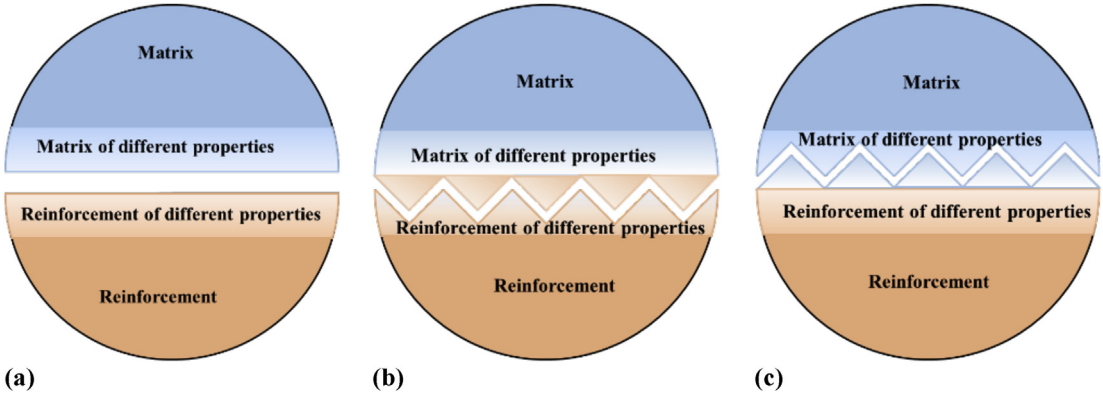

Fig. 8 – Failure modes of interphase: (a) debonding failure, (b) failure in reinforcement, (c) failure in matrix.

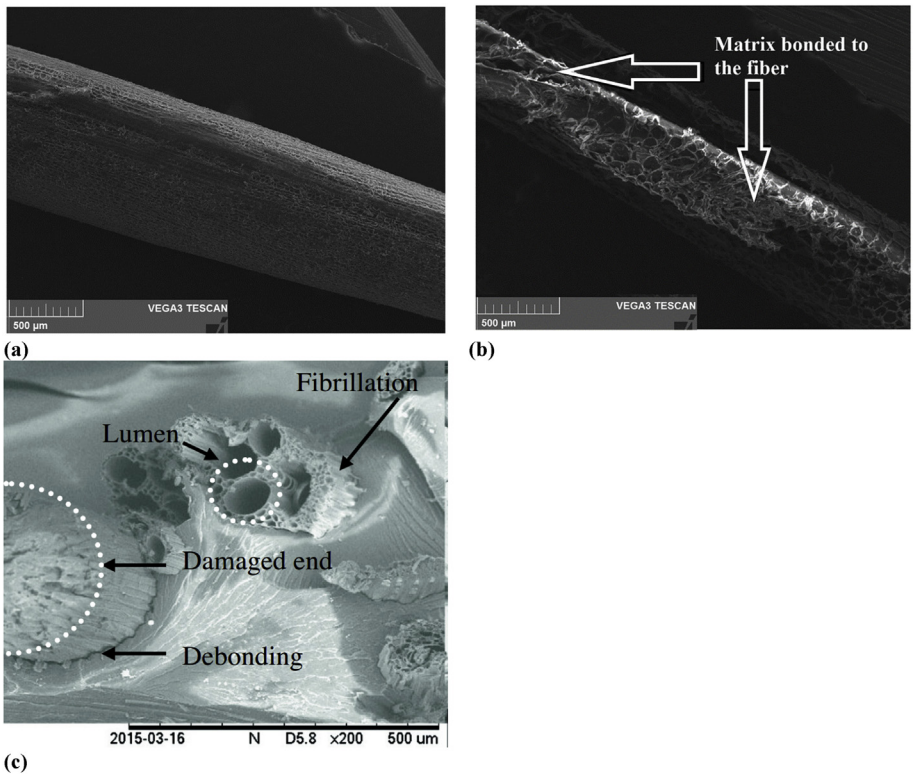

Fig. 9 – Failure modes of interphase: (a) debonding failure [47]; (b) debonding failure and failure in matrix [47]; (c) debonding failure and failure in fibre [48] (Permission granted).

due to the partially concealing of the nanotube. This underestimation leads to an overestimated shear strength. At the micro scale, the fibre fragment test requires that the matrix should be more ductile than the fibre. The fibre push-out test is suitable for fibres which can carry compressive load such as glass, carbon, and ceramic fibres. Fibre pull-out tests have no special requirements on material properties of fibres. It should be noted that the micro-bond tests cannot measure the interfacial shear strength of fibre/matrix interface in FRP, which is manufactured with pressure. At macro scale, in-plane shear test, short beam test and fracture toughness tests are suitable for laminated FRP composite material. Specially, the laminated FRP composites for the in-plane shear test need to be configured with a symmetric layer sequence. The details of these mechanical tests are discussed individually below.

2.3.1.1. *Nano-scale mechanical measurement*. At the nano-scale, the fibre pull-out test is usually performed with SPM or AFM. The nano-fibre or nanoparticle is pulled out from the polymer matrix by the tip. There are two test methods with various sample preparation. The first method can be used for both thermoplastic and thermoset polymers, whilst the second one only works when the matrix is thermoplastic. For the first method with SPM, the example of multi-walled carbon nanotubes (MWCNT)–epoxy interface is used for illustration. Nanotubes are dispersed in the epoxy resin and then mixed with the hardener to form a 200-mm-thick film. After the 200-mm-thick film is cured, the film is cut into thinner film (thickness: 70–100 nm) using a diamond knife and a Reichert-Jung ultra-cut microtome. In order to locate the interesting region where the hole of the epoxy is spanned by a nanotube (Fig. 10(a) and (b)), the semi-contact mode is used for the SPM imaging. Once the interested region is determined, the tip is slid across the hole in the contact mode. The sliding direction is perpendicular to the cantilever long axis and intersecting the nanotube axis [60]. The figures observed from transmission electron microscopy (TEM) before and after the MWCNT pull-out are shown in Fig. 10(a) and (b). The interfacial shear strength was calculated by dividing the pull-out force by the embedded area of the nanotube. Although the average interfacial strength of (MWCNT)–epoxy composite obtained in Cooper et al. [60] reached 150 MPa, the specimen-to-specimen strength variability is relatively high. There were six MWCNTs pulled out from epoxy with the maximum shear strength of 376 MPa and the minimum shear strength of 35 MPa. The author attributed the high variation to the measurement errors in the nanotube diameter and the embedded length. With respect to the second method with AFM for thermoplastic polymer matrix composite materials, such as polyethylene-butene with MWCNT [61], a single MWCNT is attached on the tip (using a nano-manipulator) and kept separated from the solid matrix in AFM. When the matrix is heated to be a liquid-like manner, the MWCNT is pushed into the molten polymer. Next, the thermoplastic matrix is cooled down to the room temperature and the tip maintains the

Table 2 – Investigations on interfacial properties through mechanical tests.

Ref.	Fibres	Matrix	Methods	Note
[60]	Carbon nanotube	Epoxy (Araldite LY564, Ciba-Geigy, hardener HY560)	Pull fibre out by scanning probe microscope (SPM)	• Both single-walled carbon nanotube (SWNT)-epoxy and multi-walled carbon nanotube (MWNT)-epoxy composites were tested • Main failure mode of MWNT-epoxy was pull-out failure and tube fracture was the dominated failure mode of SWNT-epoxy
[61]	Carbon nanotube		Pull fibre out by or atomic force microscope (AFM)	• Smaller diameter nanotubes, stronger interface, and higher fracture energy.
[62]	Flax, glass uni-directional fabric	Phenolic resin	Short beam shear test Double cantilever beam (DCB) tests	• Compared with glass fibre, the flax fibres which were twisted in bundles could provide more fibre bridging to enhance the interfacial properties (strength and fracture toughness)
[63]	Flax, glass bi-directional fabric	SR 1500 Epoxy	Double cantilever beam (DCB) tests	• Flax/epoxy system had better adhesion properties characterized by the lower critical, debonding lengths and higher IFSS
[64]	Flax, nano-TiO_2	Epofine 556 (Epoxy)	DCB test End-notched flexure (ENF) test	• Adding nano-TiO_2 could increase the fracture toughness of flax fibre reinforced epoxy. When the content of TiO_2 beyond 0.5 wt%, the agglomerate of nano-TiO_2 led to the failure at lower load values
[46]	Royal palm	E44-6101 epoxy	Single fibre pull-out test	• As the moisture content increased, the bond strength between fibre and epoxy decreased.
[65]	Flax	Poly(L-Lactic Acid) (PLA)	In-plane shear DCB test	• The influence of cooling rate: 93 °C/min, anneal at 50 °C, 15.5 °C/min and 1.5 °C/min • The in-plane shear strength and Mode I fracture toughness dropped with the slowest cooling rate
[66]	Flax, basalt	Scott-Bader Crystic VE676-03 (vinyl ester)	DCB test	• High moisture absorption by flax fibres led to a weak fibre–matrix interface
[49]	Glass	Epikote 828 (Epoxy)	Single fibre fragmentation test	• The IFSS of epoxy-glass fibre treated by silane was higher than that of epoxy–glass fibre treated by urethane
[50]	Sisal, curaua and jute fibres	Cementitious matrices	Single fibre pull-out test	• Sisal fibres showed the highest fracture energy during the pulling out, due to their higher surface roughness and more irregular cross-section shape than curaua and jute fibres in this study

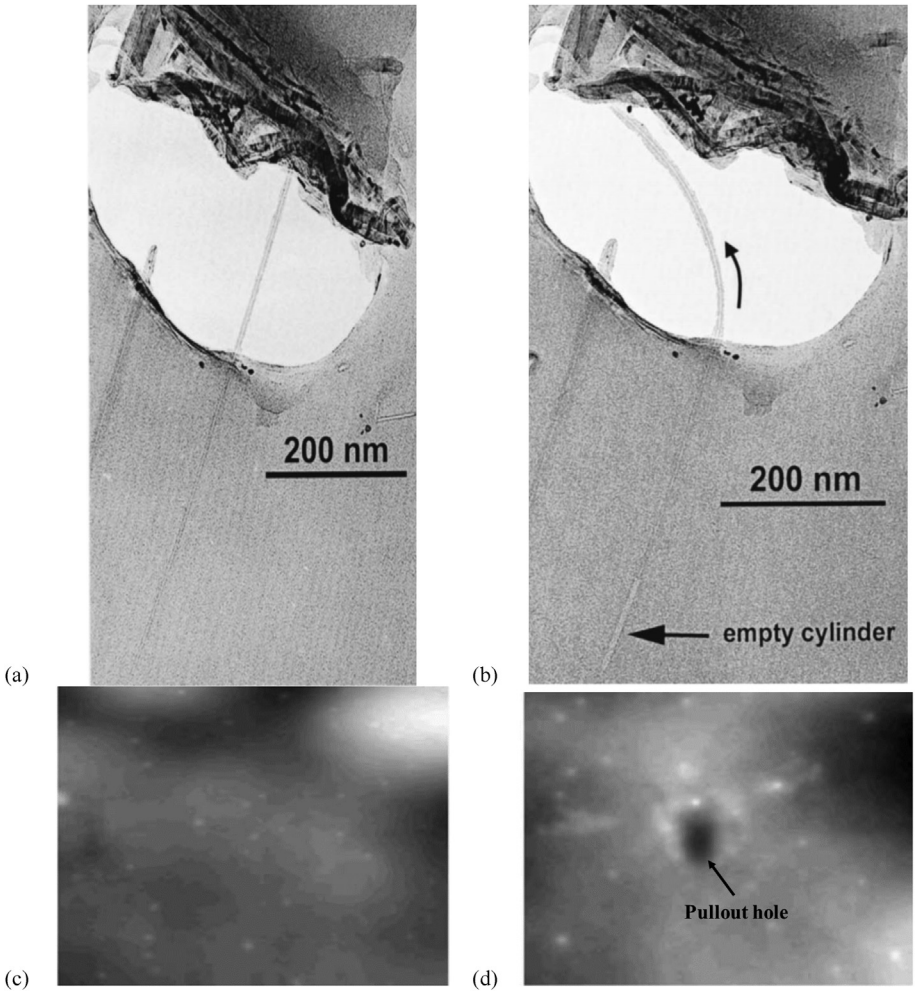

Fig. 10 – (a) TEM image of a MWNT crossing a hole in an epoxy resin matrix; (b) TEM image of a MWNT partially pull out by a SPM tip [60]. (c) AFM topography image of polyethylene-butene before pulling out of a MWNT; (d) AFM topography image of polyethylene-butene after pulling out of a MWNT (note: the horizontal scan size was 1 μm for (c) and (d)) [61] (Permission granted).

position. After the polymer matrix becomes solid, the nano-fibre/particle is pulled out by the tip. The images before and after the MWCNT pull-out are shown in Fig. 10(c) and (d).

2.3.1.2. *Fibre fragmentation test*. In fibre fragmentation test, the fibre is embedded in a dog-bone-shaped matrix, as illustrated in Fig. 11. Dimensions of the specimen in some literature are listed in Table 3. The matrix should have a larger failure strain (ideally at least three times) than the fibre in order to avoid matrix failure [67]. This test should be performed under an optical microscope to observe the in-situ fragmentation. Huang and Young [68] utilized Raman spectroscopy to capture the deformation of the carbon fibre, according to the fact that the band at 1580 and 2720 cm^{-1} in the Raman spectra will shift to the lower wavenumbers when the fibre is elongated. Tsirka et al. [69] also used the Raman spectra to study the interface deformation between epoxy matrix and carbon fibre grafted carbon nano-tubes in the fibre fragmentation test. As the tensile loading increases slowly (e.g. the crosshead speed of 0.005 mm/min in [70]), multiple fragmentations of the fibre take place [71,72] until the fibre lengths are too short to cause further breakage. With the assumption that the interfacial shear strength (IFSS) at the fibre–matrix interface is constant along the short fibre length, the IFSS of fibre fragmentation test (τ_{FFT}) can be evaluated based on force equilibrium as:

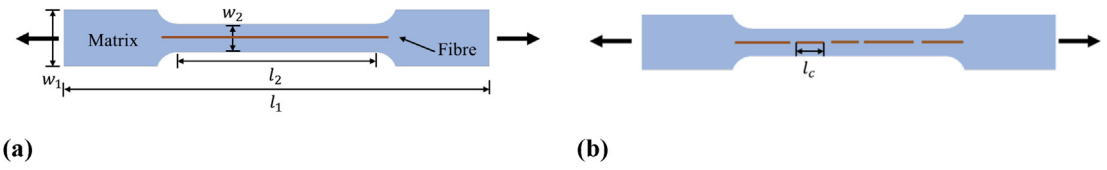

Fig. 11 – (a) Fibre fragmentation specimen and (b) fibre fragmentation under tension load.

Table 3 – Dimensions of the dog-bone-shaped sample in Fig. 11.

Ref.	l_1 (mm)	l_2 (mm)	w_1 (mm)	w_2 (mm)	Thickness (mm)
Budiman BA [73]	35	14	7	2	2
Seghini MC [70]	73	15	13	3	2
Khan Z [74]	35	16	6.4	1	–
Feih S [75]	35	16	6.45	2	2
M. J. Rich [76]	61.5	25.5	10.5	4	2

$$\tau_{FFT} = \sigma_f d_f/(2l_c) \quad (5)$$

where σ_f is fibre tensile strength; d_f is the fibre diameter, and l_c is the critical length of fibre, which is the average value of fibre fragment lengths at the end of the test [67].

2.3.1.3. *Fibre pull-out test and micro-bond test.* Fibre pull-out test is one of the most conventional tests for the investigation of bond behaviour of fibre and matrix. As shown in Fig. 12(a), the fibre is embedded in the matrix. One end of the fibre is applied load. During the test, the load and the fibre displacement are recorded. After the fibre is pulled out, the IFSS of fibre pull-out test (τ_{Pull}) can be calculated by [39].

$$\tau_{Pull} = P_{max}/\pi d_f l \quad (6)$$

where P_{max} is the maximum load; d_f is the fibre diameter, and l is the fibre embedded length.

Figure 12(b) shows the schematic of the pull-out test of multiple fibres. The matrix blocks are only connected by fibres. Using multiple fibres pull-out test, the influence of fibre volume fraction on the interfacial properties can be considered. The micro-bond test shown in Fig. 12(c) is a modified single fibre pull-out test. A small amount of matrix is applied on the fibre to form a droplet and cured to form an ellipsoid shape without external pressure. After the matrix is cured, the fibre is applied a tensile load and pulled out of the matrix. In this test, the smooth curvature at the fibre–matrix interface can reduce the stress concentration and hence reduce the variation in the interfacial shear strength [67]. However, the micro-bond test cannot measure the IFSS of fibre–matrix interface in FRP when it is manufactured with pressure, because the pressure cannot be applied during the curing process of the droplet.

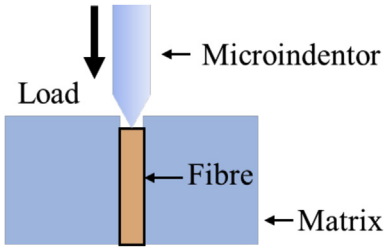

Fig. 13 – Schematic view of fibre push-out test.

2.3.1.4. *Fibre push-out test.* Fibre push-out test is applicable when the composite materials are linear elastic hard or brittle systems and there is no obvious elastic modulus mismatch between the fibre and matrix [77]. As shown in Fig. 13, a fibre is bonded in the matrix. The top surface of the fibre–matrix composite, which contacts the micro-indenter should be polished to obtain a smooth surface. During the compressive loading, the fibre is pressed into the matrix by a micro-indenter until the fibre slips from the matrix. The IFSS of composite in fibre push-out test (τ_{FPT}), can be calculated as in Eq. (7) [67]. Regarding the Poisson's ratio of the fibre, as the Poisson's ratio increases, the stress transfer from the fibre to the matrix will be more effective and then increase the shear strength [78].

$$\tau_{FPT} = \sigma_e d_f/(4l) \quad (7)$$

where σ_e is the average axial stress of the fibre, which is equal to the applied load divided by the cross-section area of the fibre; d_f is the fibre diameter and l is the debonded length derived from $l = E_f\delta/\sigma_e$. E_f is the Young's modulus of fibre, and δ is the displacement of the fibre end.

2.3.1.5. *In-plane shear test.* Through in-plane shear test, IFFS can be obtained by tensile test. The tested composite materials should be the continuous-fibre-reinforced laminated composite and the symmetric lay-up composed of +45° and −45° plies, according to ASTM D3518 [79]. The stacking sequence of the fibre in the composite should be [45/−45]*ns*, where $4 \le n \le 6$ for unidirectional tape, and $2 \le n \le 4$ for woven fabric [79]. The "*n*" stands for the fabric number and "*s*" means the symmetry of fabric sequences. The recommended controlled displacement is 2 mm/min. The

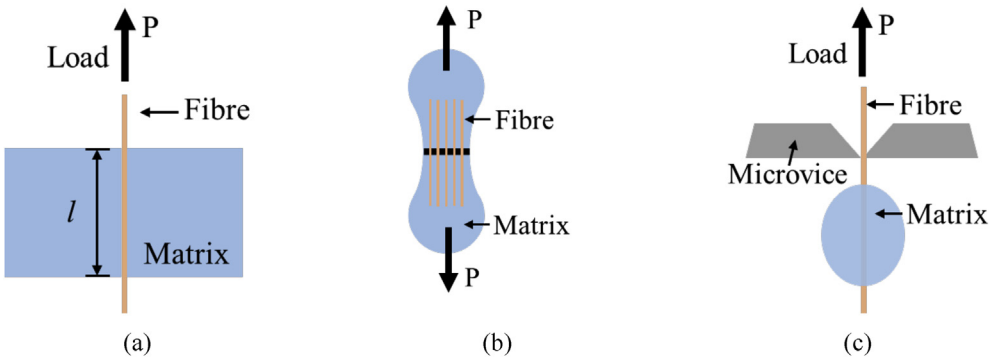

Fig. 12 – Schematic view of (a) single fibre pull-out test, (b) multiple fibres pull-out test and (c) micro-bond test.

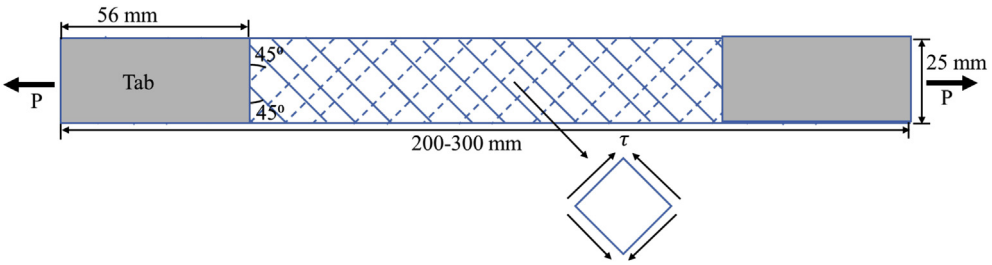

Fig. 14 – Specimen and load direction of the in-plane shear test.

dimension of the specimen is shown in Fig. 14 from ASTM D3039 [80]. Based on the force equilibrium, the shear strength of the in-plane shear test (τ_{IPST}) can be evaluated by:

$$\tau_{IPST} = P_{max}/(2A) \quad (8)$$

where P_{max} is the maximum load and A is the cross-sectional area of the specimen.

2.3.1.6. Short beam shear and double beam shear tests. For laminated fibre reinforced polymer composite, the short beam shear and double beam shear tests can be used to evaluate the maximum ILSS between fibre and the matrix. The short beam shear test is conducted under three-point bending, as depicted in Fig. 15. According to ASTM D2344 [54], the thickness of the specimen should between 2 and 6 mm. Based on the Euler–Bernoulli beam theory, the maximum ILSS of the short beam shear test (τ_{SBST}) occurs at the mid-thickness of the composite and has the relationship with maximum applied load P_{max}, specimen width b and thickness t as:

$$\tau_{SBST} = 3P_{max}/(4bt) \quad (9)$$

The double beam shear test is conducted under a five-point bending, as shown in Fig. 16. According to ISO 19927 [81], five cylindrical rollers with a diameter of 6 mm are used in the test. The load is applied through two rollers at the test speed of 1 mm/min until the specimen fails. Same to the short beam shear test, the maximum ILSS of double beam shear test (τ_{BBST}) is derived from the Euler–Bernoulli beam theory, as shown in Eq. (10).

$$\tau_{BBST} = 33P_{max}/(64bt) \quad (10)$$

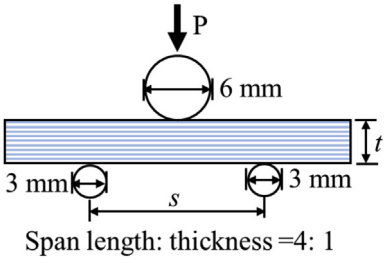

Fig. 15 – Schematic of short beam shear test.

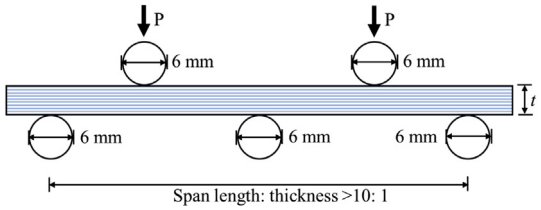

Fig. 16 – Schematic of double beam shear test.

where P_{max}, b and t are maximum load, specimen width, and thickness, respectively.

Merzkirch and Foecke [82] studied the interlaminar shear in the unidirectional carbon fibre reinforced epoxy laminate through the short beam and double shear tests. The higher shear strength was reached when the double beam test was performed. The τ_{BBST} was approximately 30% higher than the values obtained from the short beam shear test. This could be attributed to that the influence of stress concentration under the loading nose and the bending stress are reduced in double beam shear test [83].

Compared with the short beam shear test, the double beam shear test has the advantage to calculate the interlaminar shear modulus. The calculation of interlaminar shear modulus is based on the elastic modulus in longitudinal and transverse directions, Poisson's ratio, and the in-plane shear modulus of the FRP laminate.

2.3.1.7. Fracture toughness test. In the research on laminated FRP composite, the inter-laminar fracture toughness is commonly used to study the interfacial properties of laminated FRP materials. There are three modes of the crack propagation (mode I: opening mode, mode II: sliding (or in-plane shear) mode, and mode III: tearing (or out-of-plane shear) mode, as shown in Fig. 17. The fracture toughness can be characterized by the strain energy release rate, which is defined as the energy loss per unit increment in the area of the specimen as the crack grows. The calculation for the strain energy release rate in mode I, mode II and mode III are presented in this section.

Mode I and mode II fracture toughness are commonly studied in the research through the double cantilever beam (DCB) test and end-notched flexure (ENF) test, respectively. Figure 18 shows the schematic view of DCB and ENF tests. The dimensions of specimens for DCB and ENF tests are given as

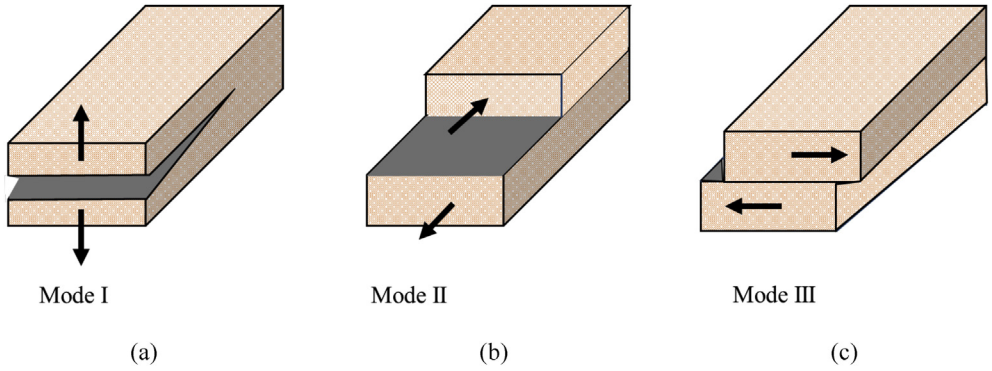

Fig. 17 – Three basic failure modes: (a) opening mode; (b) in-plane shear mode and (c) out-of-plane mode.

per ASTM D5528 [56] and ASTM D7905 [58], respectively. In ASTM D5528, the recommended width is 20–50 mm and thickness is 3–5 mm. In ASTM D7905, the width of 19–26 mm and thickness of 3.4–4.7 mm are suggested.

In DCB test, the cantilevers are pulled at a crosshead speed of 1–5 mm/min. When the crack length develops to 3–5 mm, the loading is stopped and released. The position of the crack tip needs to be marked. After that, the loading and unloading processes are repeated. In each loading process, the crack is allowed to propagate 3–5 mm in length. Once the crack length reaches 45 mm, the test should be terminated. During the test process, the load (P), the load point deflection (δ_f) and delamination length (a) are recorded. According to the Euler–Bernoulli beam theory (for a cantilever and linear elastic considerations), the strain energy release rate (G_I) in Mode I failure can be evaluated by Eq. (11) as follows:

$$G_I = 3\delta_f P/(2ba) \tag{11}$$

where b is the width of the specimen.

In practice, G_I calculated from Eq. (11) is an overestimated value, because the beam may rotate at the delamination front. In order to correct influence caused by the rotation, a longer delamination, $a + |\Delta|$, is used. The value of $|\Delta|$ is determined by experimentally generating a linear least-squares plot of $C^{1/3}$ as a function with delamination length (a) [56], as illustrated in Fig. 19, where C is the compliance, i.e. $C = \delta/P$. Therefore, the G_I can also be calculated using Eq. (12) as follows:

$$G_I = 3\delta P / [2b(a + |\Delta|)] \tag{12}$$

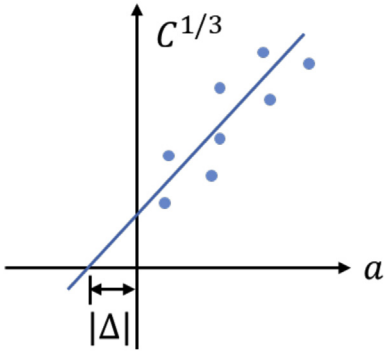

Fig. 19 – The determination of $|\Delta|$ in the calculation of G_I.

The ENF test is carried out under a three-point bending under displacement control (0.02–0.08 mm/min), until the propagation of delamination could be observed by visual assessment or the applied force drops significantly. During the test process, the load (P) and delamination length (a) are recorded. Besides the fracture tests, the compliance calibration tests are necessary to obtain the relationship between the compliance (C) and delamination length (a), which is used in the calculation of the Mode II strain energy release rate (G_{II}). The specimen of compliance calibration test is similar to the specimen shown in Fig. 18(b) with the only difference of a_0. The two lengths of a_0 (20 and 40 mm) are individually used in compliance calibration tests, the results of which are used to determine the compliance

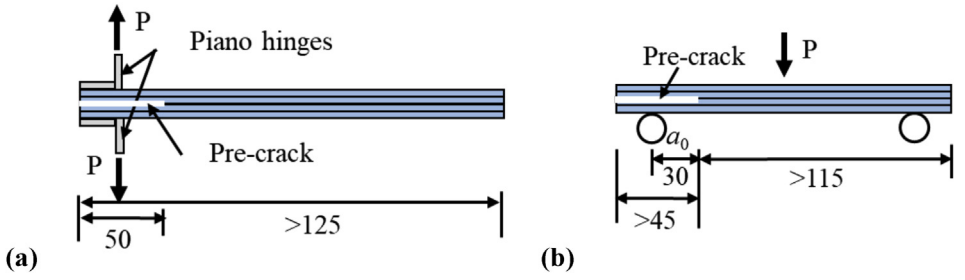

Fig. 18 – (a) Double cantilever beam (DCB) test and (b) end-notched flexure (ENF) test, unit: mm.

calibration coefficients, m_1 and m_2, using a least-squares linear regression between C and a^3:

$$C = m_2 + m_1 \cdot a^3 \tag{13}$$

The specimen in Fig. 18 (b) with $a_0 = 30$ mm is used in the fracture test. Combining the fracture test results and compliance calibration coefficients, (G_{II}) can be calculated by Eq. (14)

$$G_{II} = 3 \cdot m_1 p^2 \cdot a^2 / (2b) \tag{14}$$

where b is the width of the specimen.

However, there is a lack of a standard method to evaluate the mode III fracture toughness of FRP composites. Lee [84] proposed an edge crack torsion (ECT) test method to study the mode III fracture toughness. Ahmadi-Moghadam and Taheri [85] and Mehrabadi and Khoshravan [86] followed this method to investigate the mode III fracture toughness of GFRP. Morais et al. [87] applied the ECT method in anticlastic bending to study the mode III fracture toughness of CFRP laminated plates, as shown in Fig. 20. In Fig. 20(a), the L, B, a, h and P are the length, width, crack length, half of the plate thickness, and the applied load, respectively. The detailed view of the ECT test on CFRP from Morais et al. [87] is shown in Fig. 20(b). The red and blue arrows indicate the directions of the torsion below and above the pre-crack face, respectively.

The compliance calibration method is applied to the evaluation of Mode III strain energy release rate (G_{III}). Similar to the process for calculating G_{II}, the relationship between calibrated torsional compliance (C) and delamination length (a) is constructed by linear regression, as presented in Eq. (15).

$$1 / C = m_4 - m_3 a \tag{15}$$

where m_4 and m_3 are constants.

Hence, the fracture toughness in Mode III can be calculated according to Eq. (16).

$$G_{III} = \frac{P^2}{2B}\frac{dC}{da} = \frac{m_3 P^2}{2B(m_4 - m_3 a)^2} \tag{16}$$

where P is the applied load and B is the specimen width.

2.3.2. *Multi-scale measurement and size effects on interfacial properties*

As introduced in 2.3.2, there are various mechanical tests for FRP interfacial properties from nanoscale, microscale, and macroscale. The absolute values of the test results could be different. Drzal and Madhukar [88] tested the interfacial properties (i.e. interfacial shear strength and interlaminar shear strength) of CFRP (AU-4/828 carbon fibres in an Epon 828 epoxy) through single-fibre fragmentation test, micro-bond test, micro-indentation technique, in-plane shear test, and short-beam shear tests. The values of the results are 37.2, 23.4, 55.5, 37.1, and 47.5 MPa, respectively (Fig. 21). In microscale tests (first three tests), the micro-bond test had the lowest interfacial shear strength. The explanation from the authors

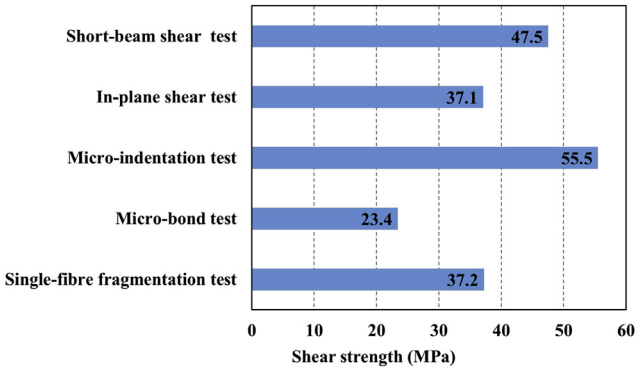

Fig. 21 – The shear strength obtained by various mechanical tests.

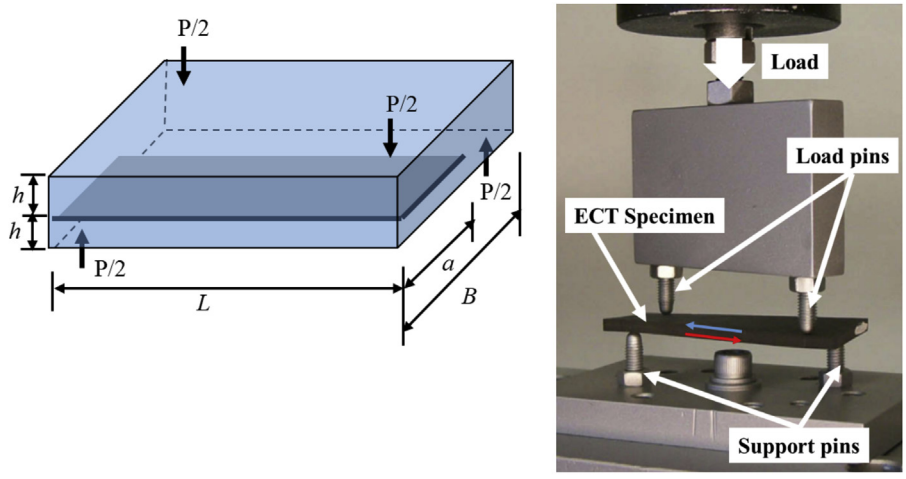

Fig. 20 – The schematic of (a) ECT specimen and (b) test setup [87] (Permission granted).

[88] is that there was a loss of curing agent in the small drops which had large surface-to-volume ratios. In macroscale tests, the difference can be attributed to the loading state of the composite or simplified assumptions during the strength calculation (e.g., in the single fibre pull-out test, the interfacial shear strength (IFSS) is related to the tensile strength and the embedded area of the fibre whilst the shear strength in short beam test is calculated based on Euler–Bernoulli beam theory and the maximum shear strength is assumed to occur at the mid-thickness. For example, in 45° tensile test (in-plane shear test), when the interfacial adhesion between fibre and the matrix is poor, there is a scissoring effect, i.e. when the woven fibre composites are subjected to off-axis loading, the warp and weft yarns that are biased with certain angle tend to reorient towards the principal loading axis [89]. This rotation cannot be measured by the strain gauges at the outer plies of the specimen due to the inter-ply failure and then results in a lower in-plane shear strength [88]. In the view of the short beam test, the ILSS is derived from the beam theory. The failure of the short beam will occur when the midplane shear stress exceeds the interfacial shear stress or the matrix shear stress [88]. There are various failure modes for short beam test specimens, such as delamination failure, local crushing of the specimen by the loading pin, bending failure, and permanent plastic deformation. The failure modes are believed to have a significant influence on the ILSS values. From Cui et al. [90], unidirectional carbon fibre–epoxy showed ILSS of 109.7 MPa in the short beam shear test when the failure mode was permanent plastic deformation. However, when the specimen failed in delamination, the average ILSS was 90.1 MPa. Therefore, a delamination failure mode should be obtained to measure ILSS correctly.

Additionally, the size effect on the measured results is worthy to point out. For the short beam shear test, Cui et al. [90] investigated the unidirectional carbon fibre–epoxy with a specimen thickness of 1.6–12.8 mm (the span-to-thickness ratio was 5:1). As the thickness increased, the ILSS decreased with a total reduction of 26%. In the aspect of interlaminar fracture toughness test, the initial crack length has been paid attention to whilst the study on specimen size effect is few.

2.3.3. *Morphology observation and chemical analysis*

The tests discussed above are the methods that can directly measure the interfacial properties (e.g., interfacial shear strength and fracture toughness) of fibre reinforced polymer composites. There are some other characterization techniques, such as scanning electron microscope (SEM), transmission electron microscopy (TEM) and Fourier-transform infrared spectroscopy (FTIR) can provide the morphological/structural (from SEM/TEM) and chemical bond analysis (from FTIR) for fibre/polymer matrix interface. These characterization methods are beneficial for understanding the interface mechanisms from the perspectives of physical and Physico-chemical changes. For example, the Physico-chemical parameters of fibre material usually considered are fibre dimension and fibre surface treatment. As for the polymer matrix, the glass transition temperature, crosslink density, and chemical modification are critical points. The typical physical parameter, e.g., fibre dimension, is measured since the change of fibre diameter can cause micro-cracks at the matrix/fibre interface which can reduce their interfacial properties. The diameter measurement can be completed by microscopic techniques, such as optical microscopes, SEM, and TEM with the resolution up to 100 nm, 1 nm, and 0.1 nm [91], respectively. In the measurement, it is necessary to measure a large number of fibres to obtain mean fibre diameter and fibre diameter distribution, which can reflect the change of fibre diameter statistically. With the development of X-ray Computed tomography (CT) scanning, the micro-CT and nano-CT can provide the dimension information in the three-dimension configurations at a multi-scale. Besides, the effects of treatment on fibre surface and polymer matrix on interfacial properties are reflected by the chemical bonding at the interface through detecting the change of functional groups with FTIR and Raman spectroscopy. For example, when the plant-based natural fibre is treated by silane solution, the polysiloxane oligomers indicated that the pre-hydrolyzed silane has reacted with the hydroxyl groups on the fibre surface to form the chemical bonding [92]. Table 4 summarizes various characterization methods used in the research on interfacial properties of fibre reinforced polymer composite materials. These methods can be classified into two categories, i.e., direct and indirect observations.

2.3.3.1. Scanning electron microscope (SEM). Scanning electron microscope (SEM) is used to observe the sample surface at the microscale by scanning the surface with a focused electron beam. The electron beam reflects off a surface with a given topography, responding to a unique signal. Due to the different materials in composite materials, the responding signals are different as well. Therefore, SEM is a commonly used technique to investigate the interphase and interfacial properties of composite materials, especially to observe the bonding state of the reinforcement-matrix systems and the bridge effect. A typical figure about the bonding state between the reinforcement and matrix is shown in Fig. 22. There were clear gaps between flax fibres and epoxy in Fig. 22(a), which indicated poor interfacial bonding. After adding 0.5% TiO_2, there was no apparent gap between fibre and epoxy (see Fig. 22(b)). Figure 23 shows the failure surface of carbon fibre composite reinforced with nylon nano-fibre after the DCB test. It was observed that the nylon fibres were embedded in the epoxy matrix and strongly attached to the carbon fibre [98], which was expected to enhance the bridge effect in the carbon fibre reinforced composite material.

In addition to observing the interface based on the failure surface, SEM can also be used for the in-situ assessment of the fibre–matrix interface. Ghaffari et al. [51] used in-situ SEM to observe the fibre push-out test conducted on the carbon fibre reinforced epoxy composite. The process of fibre push-out test is introduced in the previous section 2.3.1.4. During the test, when there is a load eccentricity of the indenter (Fig. 24(a)) or the failure happens to the fibre and matrix (Fig. 24), the results cannot reflect the interfacial properties between the fibre and matrix, which need to be discarded for shear strength calculation. In the exact interface failure (Fig. 25), the fibre ends which are pushed out can be clearly observed. Through monitoring the load condition by real-time in-situ SEM, the data from samples with interface failure is selected to calculate the interfacial shear strength.

Table 4 – Characterization methods of interphase in composite materials.

Interface observation	Method	Feature	Application in interface analysis
Direct observation on interface	Scanning electron microscope (SEM)	Reflecting the morphology of the sample surface	Coupled with EDX to determine the compositions of different elements at the interface [93,94]
	Transmission electron microscopy (TEM)	Reflecting the internal and external structure of the sample	
	X-ray computed tomography (CT) scanning	Presenting the internal and external structure of the sample in three-dimension (3D)	Imaging the interface in 3D Tracing the interface in situ
	Atomic force microscope (AFM)	Imaging the surface properties (e.g., morphology, roughness, and texture) of the sample	Quantifying the change of the surface properties by a specific tip
	Nanoindentation	Measuring the hardness and reduced elastic modulus of the sample surface	Quantifying the hardness and reduced elastic modulus of fibre/matrix interface
Indirect observation on interface	Thermogravimetric analysis (TGA)	Computing the weight loss in the materials with the increasing temperature	Obtaining the mass of some reaction product in the interphase Coupled with TEM to calculate the thickness of the interphase of nanocomposite [95]
	Fourier-transform infrared spectroscopy (FTIR)	Reflecting the functional groups on the sample surface by the absorbed energy from infrared light	Presenting the change (occurring and disappearing) of chemical groups associated with the interfacial bonding
	Raman spectroscopy	Reflecting the functional groups on the sample surface through the scattering energy of the sample irradiated by visible light (or near-infrared)	FTIR and Raman spectroscopy are complementary mutually. Generally, a sample with a weak FTIR result has a strong Raman scattering spectroscopy
	Energy dispersive X-ray spectroscopy (EDX)	Identifying qualitatively the compositions of different elements in a specific sample at one part hundred range based on the interaction between the X-ray excitation and the sample [96]	Coupled with TEM to determine the compositions of different elements at the interface
	X-ray photoelectron spectroscopy (XPS)	Identifying the composition, chemical, and electronic states of elements in the sample The composition can be determined at one part thousand range [96]	Determine the compositions of different elements at the interface
	Solid-State Nuclear magnetic resonance (NMR)	Characterizing the structure and dynamics of the polymer based on NMR's sensitivity to the chemical shifts, relaxation times, and dipolar couplings [97].	Observing the structure of the polymer at the interface through the magnetization exchange from the reinforcement surface [97]

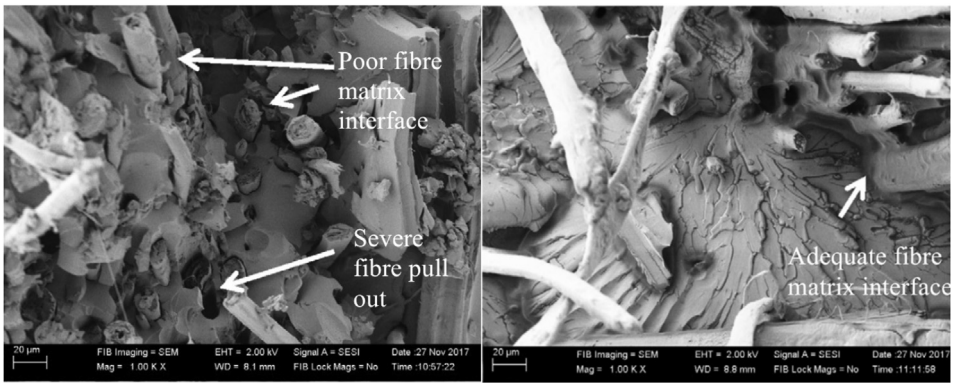

Fig. 22 – SEM images of flax fibre reinforced epoxy composites with TiO_2 addition by (a) 0% (b) 0.5% [99] (Permission granted).

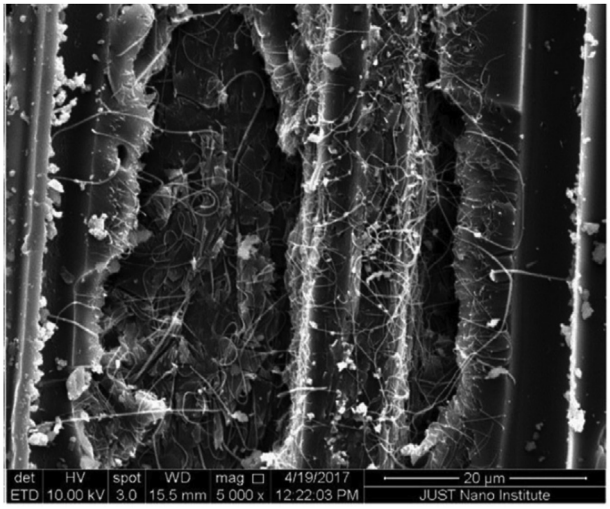

Fig. 23 – The inter-laminar surface of carbon fibre composite reinforced with nylon nanofiber [98] (Permission granted).

2.3.3.2. *Transmission electron microscopy (TEM)*. Transmission electron microscopy (TEM) is a microscopy technique where a beam of energetic electrons transmits through a sample and the image is formed by the interaction of electrons and the atoms of the sample [96]. Compared with SEM which can only be used to observe the sample's morphology, TEM can provide the image of the sample's inner structure. For example, in the interphase of carbon nanotube (CNT)–epoxy, the partial pull-out of CNT and the empty cylinder in epoxy can be observed [60,100], as shown in Fig. 10 before.

2.3.3.3. *Energy-dispersive X-ray spectroscopy*. Energy-dispersive X-ray spectroscopy (EDX, EDS, EDXS, or XEDS) is used to identify the chemical elements on the sample and their relative contents. The principle is that when a sample adopts the energy from the incident electron, an X-ray will be activated. For a certain element, there is a corresponding specific X-ray. Therefore, EDX can be coupled with SEM (signals from secondary electron) and TEM (signals from electron scattering) to analyse the elemental composition of the image from SEM or TEM. An interface analysis coupling TEM with EDX is illustrated in Fig. 26 and Table 5. The calculation of elemental composition was based on the data of six red dashed zones. The specimen was prepared through coarse and medium milling by beam current from Gallium (Ga) ion source. In the three phases (carbon fibre, interface, and epoxy) of the composite, the implantation capability of Ga^+ ion is different. The bulk carbon fibre has a better Ga^+ resistance because of its crystal structure [94].

2.3.3.4. *X-ray computed tomography (CT) scanning*. X-ray Computed tomography (CT) scanning is the technique to image the scanned object in three-dimension (3D) by injecting X-ray from different angles. The attenuation of X-ray photons is the base of the technique. When the X-ray photons pass through an object, the attenuation depends on the physical

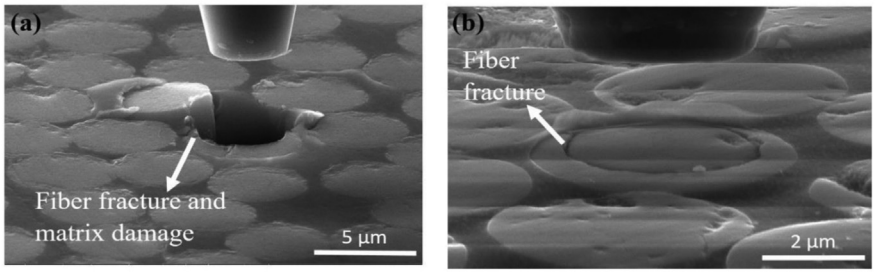

Fig. 24 – Fibre and matrix damage in fibre push-out test: (a) fibre and matrix failure (b) fibre fracture [51].

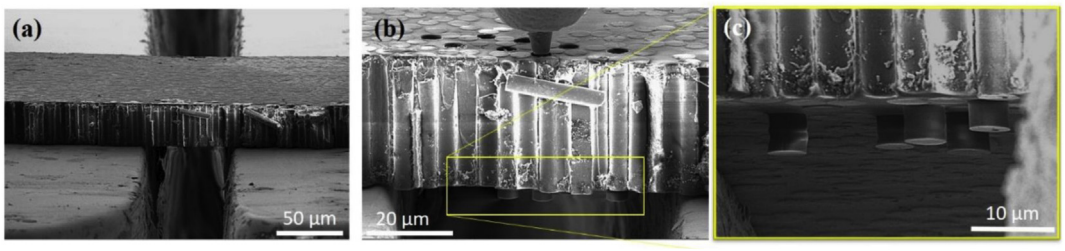

Fig. 25 – Interface failure in fibre push-out test: (a) before the test; (b) and (c) after the test [51].

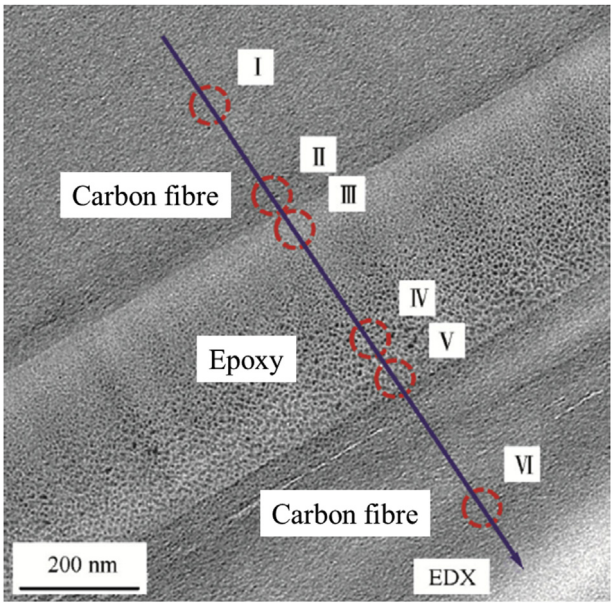

Fig. 26 – TEM image and EDX results of carbon fibre–epoxy–carbon fibre interface [94] (Permission granted).

density of the object. Therefore the object that contains different phases can show different levels of X-ray attenuation [101]. The X-ray detector can obtain one two-dimension (2D) projection image from one scanning. After scanning the object during 360° rotation, all the 2D images will be computed to cross-sectional slices and further processed into the 3D modes of the object. The 3D representation can provide more details about the interface compared with the 2D representation from SEM or TEM. The image from SEM or TEM can only reflect the morphology of a cross-section of a sample. In the image from 3D CT scanning, however, the whole structure of the sample can be observed. The micro-computed tomography (μCT) and nano-computed tomography (nCT) can detect internal structures with a high resolution, ranging from 30 nm to 20 μm (synchrotron X-ray CT) or ranging from 50 nm to 100 μm (laboratory X-ray CT) [102]. Seghini et al. [70] used μCT to reconstruct the fractured area of the flax yarn after the fragmentation tests on flax/epoxy and flax/vinylester single yarn composites, as shown in Fig. 27. For both epoxy and vinylester samples, the failure mainly appeared at the peripheral zone of the flax yarn. Besides the 3D reconstruction of the tested sample, CT scanning can provide the in-situ analysis as well, which is beneficial for the observation of the micro-crack initiation during the debonding of the fibre/matrix interface. Figure 28 shows the CT images of carbon fibre/epoxy composite at nanoscale under fibre push-in test performed by Watanabe et al. [103]. Through the 3D CT scanning, not only the 3D structure (left figures), but also the various cross-sections (e.g., Z_1 and Z_2 in X–Y plane, Y_1, Y_2, and Y_3 in X–Z plane) can be observed. Additionally, a time-lapse X-ray CT scanning can shed light on the progress of composite degradation [104]. It is advantageous to track and analyse the changing of the interface. As shown in Fig. 28, as the insertion displacement increased, cracks propagated through the plastic zones of the epoxy resin [103]. Additionally, the radial expansion of the fibre during the test also affected the crack propagation, which need to be further investigated through 3D CT scanning.

2.3.3.5. *Thermogravimetric analysis (TGA)*. Thermogravimetric analysis (TGA) is carried out to investigate the thermal

Table 5 – Element content from EDX results of carbon fibre–epoxy–carbon fibre interface (only red circles region on the blue line in Fig. 26).

Region	Element content (%)					
	Gallium (Ga)	Carbon (C)	Nitrogen (N)	Oxygen (O)	Silicon (Si)	Sulphur (S)
I	0.15	97.72	1.22	0.80	0.09	–
II	0.21	95.96	1.05	2.40	0.06	0.29
III	0.24	92.98	2.50	3.86	0.08	0.30
IV	0.48	89.49	3.98	5.18	0.13	0.71
V	0.41	94.30	1.27	3.37	0.09	0.53
VI	0.13	97.66	1.44	0.64	1.10	–

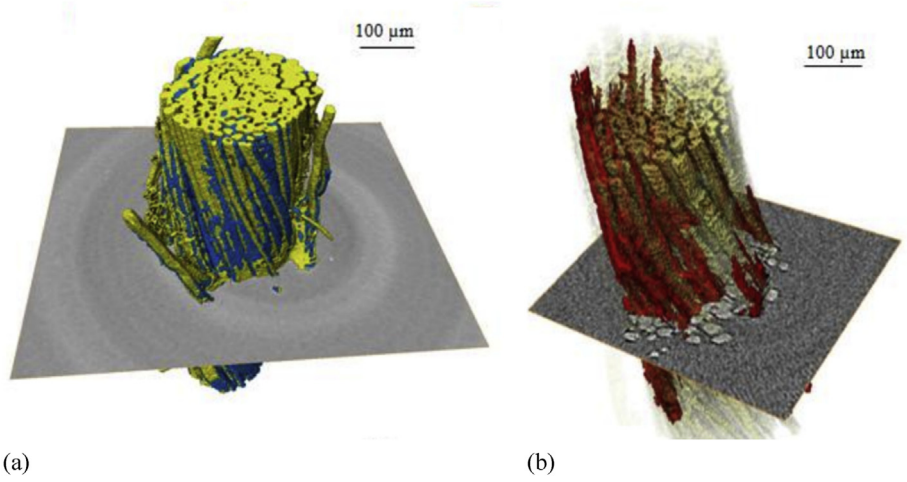

Fig. 27 – The 3D reconstruction of (a) flax yarn from the flax/epoxy composite (blue: failure zone), (b) flax yarn from the flax/vinylester composite (red: failure zone) [70] (Permission granted).

performance of nanocomposites by measuring the weight of the sample with the increasing temperature in a controlled atmosphere. TGA can help to understand compositions at the interface when there is a reaction product at the interphase and the product has a distinguished decomposed temperature. Moreover, combining the measurements of dimensions with TEM and the weight loss with TGA, the thickness of the polymer (L_{eff}) adopted by nanoparticle and the number of anchoring points per chain in a composite (n_{anc}) can be calculated. For instance, Ciprari et al. [95] tested Al_2O_3- poly (methyl methacrylate) (PMMA), Al_2O_3-polystyrene (PS), Fe_3O_4-PMMA, and Fe_3O_4-PS with TGA and TEM. The PMMA-Al_2O_3 was manufactured using Al_2O_3 nanoparticles in a solution of PMMA dissolved in chlorobenzene. The PS-Al_2O_3 was produced with Al_2O_3 nanoparticle and PS was dissolved in toluene. The PMMA-Fe_3O_4 was manufactured by Fe_3O_4 nanoparticles and PMMA in chlorobenzene. And the PS-Fe_3O_4 was produced by Fe_3O_4 nanoparticles and PS in toluene. Samples for TEM were small droplets of the solutions. Samples for TGA were the solid mass obtained through centrifuging the polymer–nanoparticle mixtures. The thickness of the polymer (L_{eff}) was derived by Eqs. (15) and (16) given below. The Al_2O_3 and Fe_3O_4 particles clusters are assumed to be spherical, and the polymer is adsorbed evenly on the clusters. Therefore, the thickness of the polymer is equal to the radius of the cluster with polymer minus the radius of the cluster, as presented in Eq. (15). The average diameter of the cluster (D) is determined by the measurement from TEM. The V_{total} can be calculated by Eq. (16). V_{total} is the volume of a cluster which is obtained from the measured diameter. $V_{polymer}$ is the volume of the adopted polymer. It is calculated based on the sample mass (M_{sample}) and the mass fraction of polymer ($w_{polymer}$) which are determined from TGA. The number of anchoring points per chain in a composite (n_{anc}) was derived by Eq. (17). The results indicated that the n_{anc} of PMMA-Al_2O_3 and PS-Al_2O_3 were larger than that of Fe_3O_4-PMMA and Fe_3O_4-PS. This means in these two matrices (PMMA and PS), the Al_2O_3-matrix had stronger interfacial bonding than that in Fe_3O_4-matrix.

$$L_{eff} = \left(\frac{4\pi}{3}V_{total}\right)^{1/3} - \frac{D}{2} \tag{17}$$

$$V_{total} = V_{cluster} + V_{polymer} = V_{cluster} + \frac{M_{sample}w_{polymer}}{\rho N_{cluster}} \tag{18}$$

where ρ is the density of polymer and $N_{cluster}$ is the number of clusters in the sample.

$$n_{anc} = \frac{\overline{M_W}}{M_{mon}(2n_{eff} - 1)} \tag{19}$$

where $\overline{M_W}$ is the average molecular weight of the polymer; M_{mon} is the molecular weight of polymer monomers and n_{eff} is the average number of repeating units of the polymer.

2.3.3.6. Fourier-transform infrared spectroscopy (FTIR) and Raman spectroscopy. Fourier-transform infrared spectroscopy (FTIR) and Raman spectroscopy are used to reflect the functional groups on the sample by infrared and visible light (or near-infrared), respectively. Entities with strong Raman responses tend to have weak infrared spectroscopy responses and vice versa. The vibration of chemical bonds absorbed light with a specific wavelength. Since a certain chemical group has the corresponding absorption ranges on the spectroscopy, the function group associated with interfacial bonding can be analysed by FTIR and Raman scattering. For example, Goumri et al. [105] studied the interphase of poly (vinyl alcohol) (PVA) with low graphene oxide (GO) and partially reduced graphene oxide (PRGO) loadings (i.e., 0.5 wt%, 1 wt%, and 2 wt%) by FTIR and Raman spectroscopy. The D-band (at 1332 cm^{-1} in the spectroscopy) is related to structural defects of graphene nanolayers. The disappearance of the 2D band (i.e., as a second-order two phonon process) is attributed to the presence of the carboxyl groups on the surface of the GO. This chemical group provided a better bonding between the hydroxyl groups of the PVA matrix and the oxygenated functionalities of the GO [105]. Table 6 summarized the commonly investigated absorption peaks regarding the interfacial bonding between the fibre and matrix.

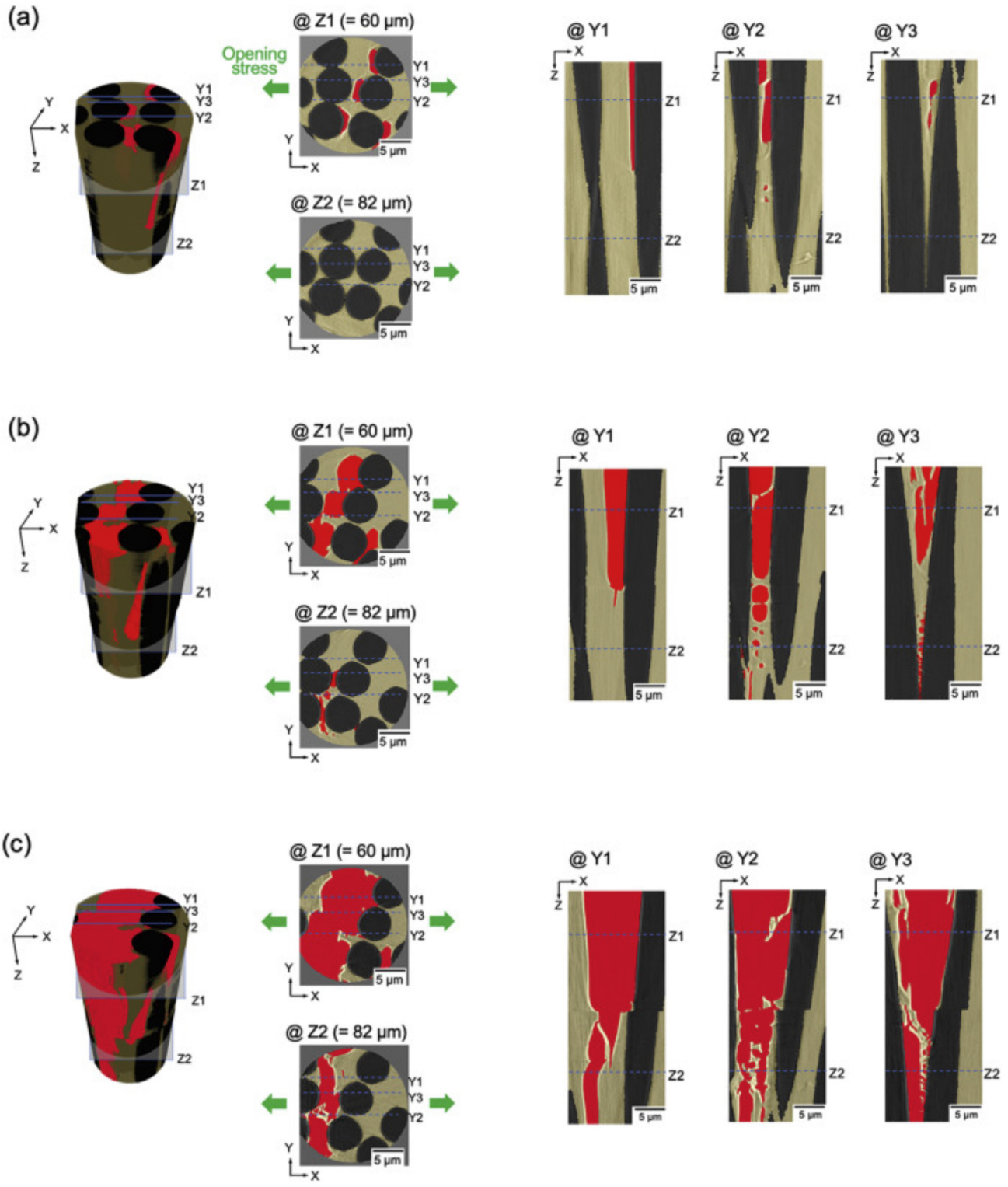

Fig. 28 – CT images for the carbon fibre/epoxy composite at different amounts of indentation displacement: (a) 15 μm, (b) 20 μm and (c) 25 μm. The grey, dark yellow, and red regions represent the carbon fibres, plastic resin, and cracks (air), respectively. The green arrows mean the open stress directions [103] (Permission granted).

2.3.3.7. Atomic force microscope (AFM). Atomic force microscope (AFM) can be also used as a characterization method for the surface properties (morphology, roughness, texture [96], adhesion, viscoelasticity, and energy dissipation [113]) based on the interaction between the tip at the free end of a cantilever in AFM and surface atoms of a sample. The tip is

Table 6 – Functional groups investigated in spectroscopy for fibre/matrix interface.

Functional group	Absorption band (cm^{-1})	Fibres	Influence on the interface
C–F (carbon–fluorine group)	950–1280 [106]	Oxyfluorinated carbon fibre [106]	• Increasing the specific polarity of the fibre surface • Formatting of Ox–Fx bonding between the fibre and matrix [106]
–OH	3400–3200	Plant-based natural fibres	• Reducing the water absorption of the fibre to migrate the mismatch in swelling ratios of the fibre and matrix which can cause micro-cracks at the fibre/matrix interface • Reacting with coupling agents to form chemical bonding
C═O	1736–1741 [107] 1735–1737 [108]	Sisal, jute, and kapok fibres treated by NaOH solution [107] Coir fibre treated by NaOH solution [108]	• Reduction/disappearing means the partial reaction/removing of the hemicellulose. (reducing the hemicellulose can make the fibre surface rough to increase the interfacial bonding)
C═O CH═CH	1730 [109] 1715 [110] 1581 [110]	NaOH treated Borassus fruit fibre + maleated Polypropylene [109] Flax fibre treated by maleic anhydride (MA) [110]	• Forming chemical bonding between the fibre and matrix (two ends of the MA agent connect the –OH of fibre and matrix respectively) [109,110]
Si–O–Si	762 and 1030 [111]	Glass fibre treated by silane solution [111]	• Forming chemical bonding between the fibre and matrix (two ends of the silane coupling agent connect the –OH of fibre and matrix respectively)
C–O–Si	1162–1159 [112] 956–1149 [108]	Flax fibre treated by silane solution [112] Coir fibre treated by silane solution [108]	
Si–O–Al	522–521 [112]	Flax fibre grafted with nanoclay by silane [112]	• Grafting nanoclay on the fibre surface to increase the surface roughness [112]

attached at the free end of a cantilever in AFM. There are three working modes for AFM scanning: contact mode, semi-contact (or tapping) mode, and non-contact mode. In the contact mode, the repulsive force between the atoms is recorded to analyse the surface properties. On the contrary, in the non-contact mode, the attractive force between atoms is measured to reflect the surface properties. The interaction force results in the deflection of the cantilever, which is measured through an optical beam method. In the semi-contact (or tapping) mode, the tip is oscillated near the resonance frequency of the cantilever and touches the sample surface periodically. When the tip passes over a concave region of the surface, the cantilever has a higher amplitude. Contrarily, the amplitude is lower when the tip passes over a convex region. Therefore, the change in oscillation amplitude is used to measure the topographic variations on the sample surface [114]. Monclus et al. [115] investigated the interphase of glass flake-reinforced polypropylene composite by AFM. The variations of the contact stiffness between tip and sample surface were observed by measuring the deflection of the cantilever in contact mode. There was an abrupt interphase between the glass flake and the polymer (Fig. 29), as the glass region is stiffer than the polymer region. Cech et al. [116] utilized AFM to study the surface topography and phase imaging of the interface between glass fibre and polyester in semi-contact mode. The surface topography of the interface can be seen in Fig. 29(a), and the height and phase profiles along the white line are shown in Fig. 29(b). An abrupt phase shift can be observed between the interface and fibre. The author attributed the shift to the great difference in Young's modulus between the interface and the fibre. Wang and Hahn [117] used AFM height images to characterize the interphase of CFRP and investigated the influence of hygrothermal treatments on the interphase in tapping mode, which is a modified non-contact mode. Under the tapping mode, the tip scans the sample surface with the cantilever oscillating at (or near) its resonance frequency. The topography of the sample surface leads to the variation of the distance between the sample surface and tip. When the tip gets closer to the sample surface, the adhesion force (e.g., van der Waals force and electrostatic force) between the tip and the sample surface will reduce the amplitude. The signal of amplitude reduction is recorded to form the topography image of the sample. The reduction of the height difference between fibre and matrix was attributed to the swelling of matrix by moisture absorption. In contrast, the height difference ascended when the specimens were treated by high temperature (120 °C). This was attributed to the matrix shrinkage caused by the post-curing under elevated temperature.

2.3.3.8. Nanoindentation. Nanoindentation is the method to characterize the surface mechanical properties (e.g., reduced modulus and hardness) of the tested material. The process of nanoindentation measurement is shown in Fig. 30(a), where the calibrated indenter tip approaches the material surface. When the tip contacts and indents into the sample surface, the force increases. After the maximum load is achieved, the sample will be unloaded. The maximum indentation depth

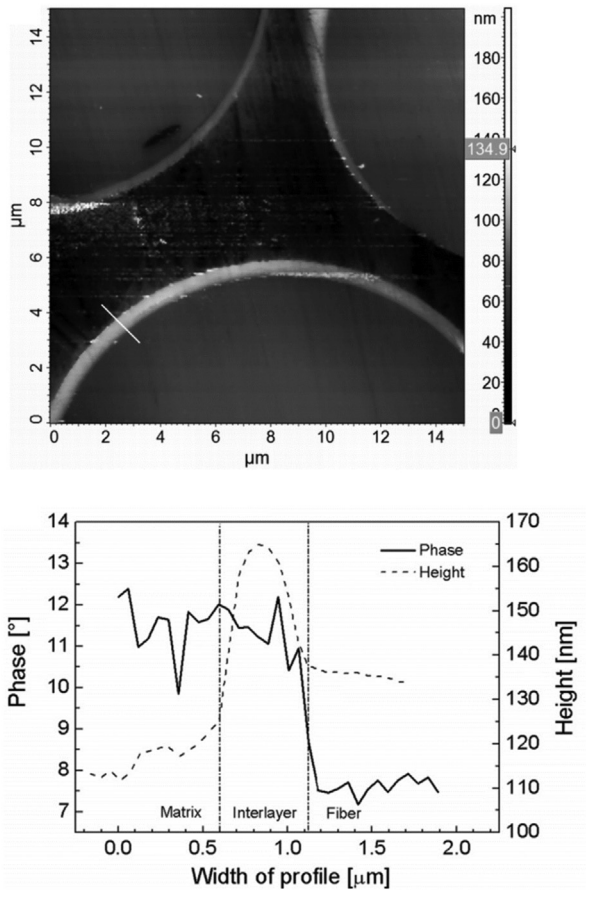

Fig. 29 – AFM image of the interface of glass fibre reinforced polyester composite: (a) Surface topography; (b) Height (dashed line) and phase (solid line) profiles across the interface [116] (Permission granted).

(h_{max}) is the total displacement of the indenter, which is equal to the sum of elastic and plastic deformation of the sample. The residual depth (h_f) after unloading is the plastic deformation of the sample. The contact depth (h_c) indicates the height of the contact surface between the indenter and the deformed surface, which is used for calculating the contact area of the indenter for further quantification of hardness (H) and reduced elastic modulus (E_r), as shown in Eqs. (20) and (21).

$$H = \frac{P_{max}}{A_c} \tag{20}$$

$$E_r = \frac{\sqrt{\pi}}{2\beta} \times \frac{S}{\sqrt{A_c}} \tag{21}$$

where P_{max} is the maximum applied load and A_c is the contact area of the indenter. The β is a constant for the indenter geometry. The unloading stiffness (S) shown in Fig. 30(b) is measured at the initial point of the unloading, which is the derivative of applied load (P) with respect to the indent depth (h_{in}):

$$S = \frac{dP}{dh_{in}} \tag{22}$$

When the nanoindentation test is performed on the fibre reinforced polymer composite, the difference in the hardness and reduced modulus between the fibre and polymer matrix can be used to determine the interfacial parameters such as the thickness and elastic modulus. Figure 31 shows the load–displacement curves for short carbon fibre (SCF) reinforced polyether ether ketone (PEEK) composite [118]. The SCF showed elastic behaviour, while the PEEK matrix showed a hysteresis loop during each loading–unloading cycle due to the viscoelasticity and elastic strain relaxation of the matrix. The load–displacement curves of the interface were between the curves of fibre and matrix. The closer the measured curves to the hysteresis loops are, the softer is the interphase.

The nanoindentation on the interface between the matrix and man-made fibre (e.g. carbon [118,119] and glass [120,121]) have been widely investigated. Carbon and glass fibres are homogeneous materials, and it is assumed that no other interfaces exist within monofilament individual glass or carbon fibre. In contrast, plant-based natural fibre has a hierarchical structure so that it is challenging to use the

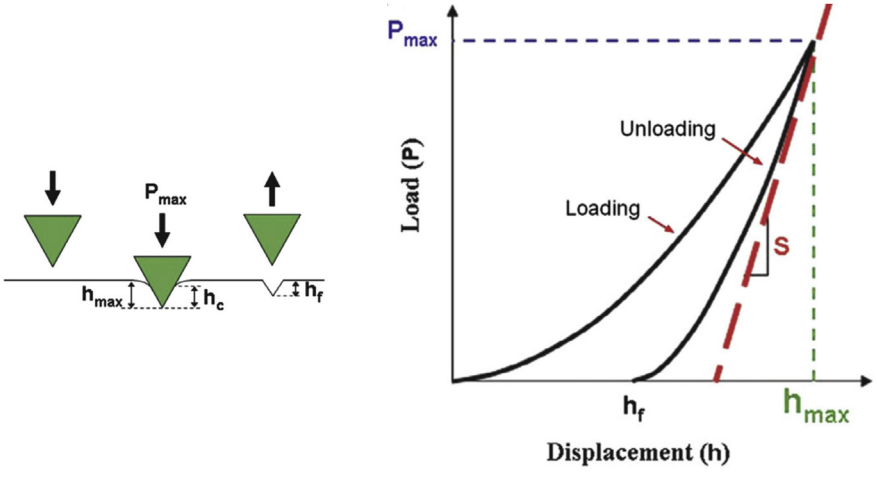

Fig. 30 – (a) The process of a nanoindentation test; (b) a typical load–displacement curve of a nanoindentation test [118] (Permission granted).

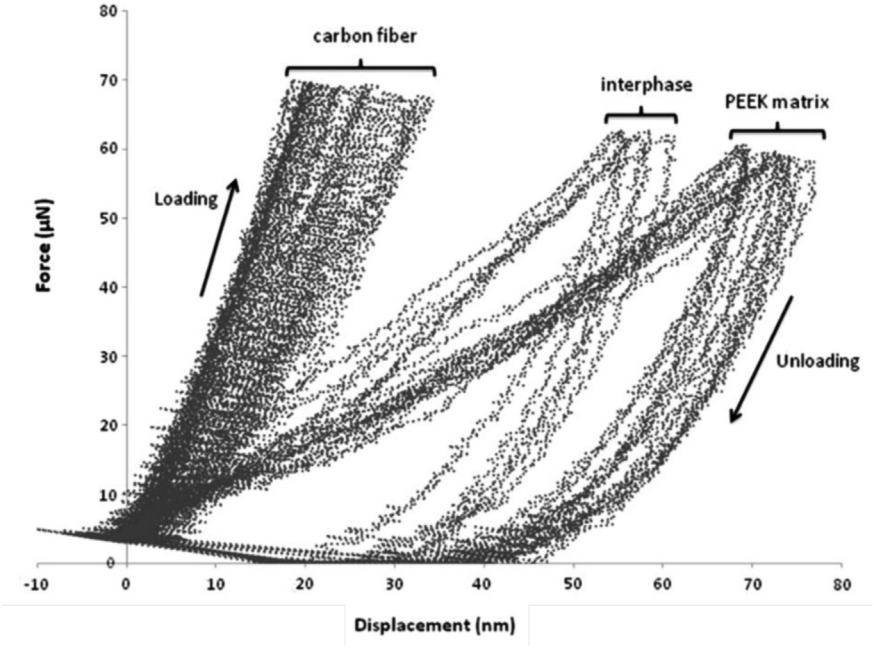

Fig. 31 – Typical load–displacement curves of SCF-PEEK composite [118] (Permission granted).

nanoindentation method to identify interfacial parameters (i.e., hardness and reduced elastic modulus of the interface) of plant-based natural fibre reinforced polymer. The reason is that one cannot simply judge whether the changes of hardness and reduced elastic modulus result from the matrix/fibre interface or the hierarchical structure of the plant-based natural fibre. For example, a single plant-based fibre contains the primary cell wall (P layer), secondary cell wall (S1, S2, and S3 layers), and the enclosed hollow lumen. Therefore, the change of the modulus and hardness is likely to occur at both the matrix/fibre interface, the interface between cell walls (i.e., middle lamella) and interface between the cell wall and lumen. Li et al. [122] investigated the interfaces at the epoxy/sisal fibre composite by AFM equipped with a nanoindentation system. A variety of points need to be measured for the matrix and the fibre in a cross section to distinguish different interfaces (matrix/fibre interface and interface in cell walls) in the composite. The detailed positions of nanoindentation are illustrated in Fig. 32(a). Figure 32(b) and (c), showed that there are similar values of hardness and reduced elastic modulus between the matrix and the lumen areas, which were significantly lower than the values of the corresponding cell walls measured. In the cell walls, the hardness and reduced elastic modulus were not constant. The S2 layer had the highest values of the hardness and reduced elastic modulus among all the cell wall layers (i.e., P, S1, S2 and S3 layers, as shown in Fig. 32.

2.3.3.9. *Characterization aided by machine learning and automated algorithms*. The characterization of interfaces in FRP aims at understanding the interface mechanisms which can advise FRP composite design with good interfacial bonding performance. However, there is still a lack of the theoretical relationship between the interface properties and the mechanical properties of FRP, which is nearly impossible to be achieved due to the complexity, inhomogeneity, and large uncertainty of the interfacial properties. Therefore, researchers turn to alternative methods which can deal with unseen and complex patterns and correlate the interfacial properties and the mechanical properties of FRP composite materials. Machine learning and automated algorithms (through processing a large number of 2D images into 3D data sets) are potential approaches to predict the mechanical properties of FRP composite materials and even capture the sub-micro defects in the FRP with high accuracy.

Konstantopoulos et al. [123] used Machine Learning classification models to process the nanoindentation mapping data to identify the influence of interface modification on the hardness and reduced tensile modulus of CFRP. The modification methods on the carbon fibre were functionalization with oxygen groups, functionalization with monomer grafting, and using carbon nanotubes. Three trained models used in machine learning included artificial neural networks (ANN), classification trees, and support vector machines (SVM). The procedure is given in Fig. 33. The original training data were from the nanoindentation results with the indentation displacement of 200 nm. Before the machine learning, the raw data was pre-processed to avoid the model overfitting and the model bias due to different scales of magnitude between different variables (e.g., contact depth, hardness, and reduced elastic modulus from the nanoindentation tests). Specifically, the raw data was processed to discard the variables with strong correction (exceeding ±0.90) through calculating the correlation value between every two variables. It should be noted that, during the pre-processing, the raw data were normalized with the z-score normalization method, in which the distances between the raw data and the mean were computed in standard deviations. The pre-processed data

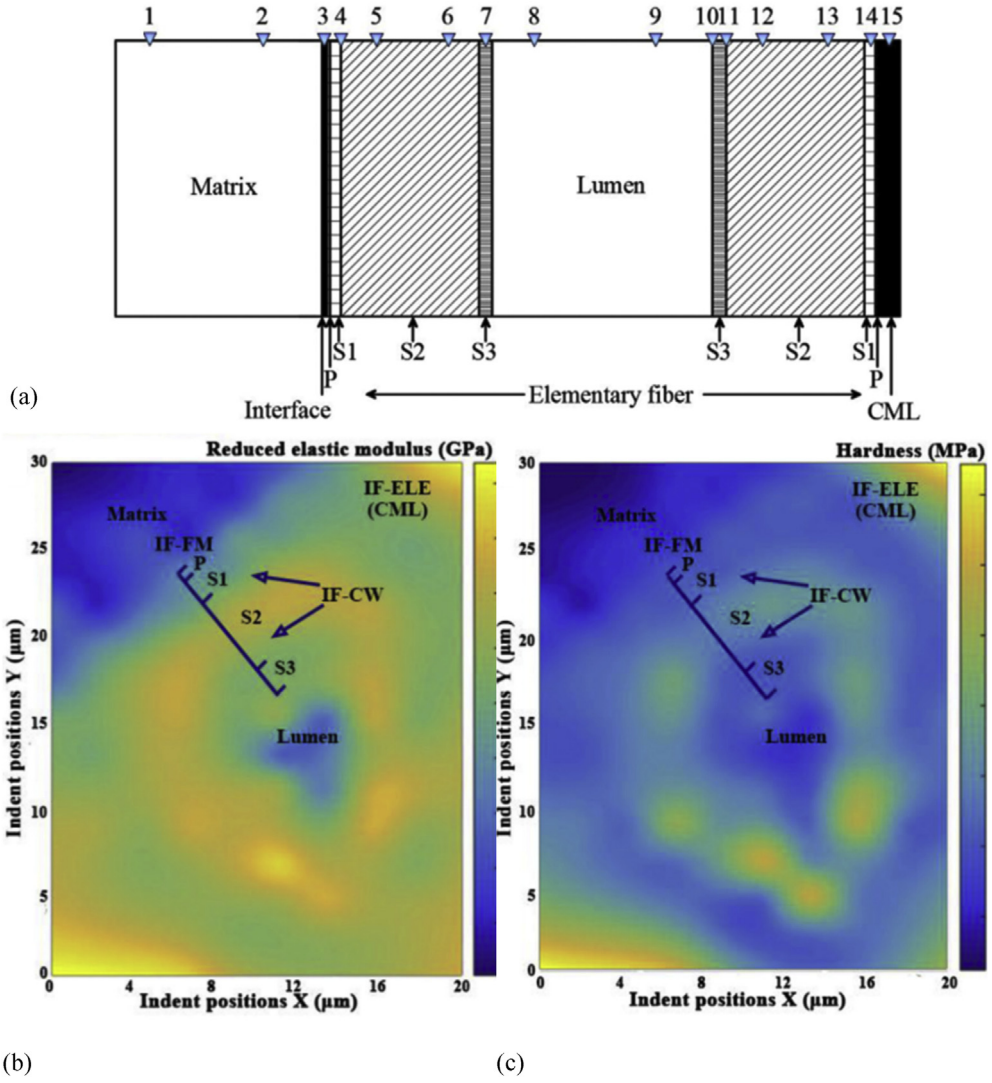

Fig. 32 – (a) Indentation position; (b) reduced elastic modulus and (c) hardness of the sisal fire reinforced epoxy composite. (CML: compound middle lamellae which gluing fibre together) [122] (Permission granted).

were classified into clusters (i.e., epoxy, reinforcement, interface, and carbon fibre clusters) by the k-means algorithm in which each datum was partitioned to the cluster with the nearest mean. Next, the clustered data was trained by ANN, classification trees, and SVM methods. After the training, the prediction models between the interface modification and indentation mapping were established. Additionally, to test the transfer learning potential, the dataset from the nano-indentation results with the indentation displacement of 400 nm (Fig. 33) was used for validation. As a result, the SVM kernel classification showed a relatively good accuracy (prediction accuracy was 72.7%) to describe the effect of carbon fibre modification.

Fritz et al. [124] used automated algorithms to process the 3D dataset of CFRP laminates captured by micro-CT. The methods to identify the inter-laminar thickness and voids are presented in Fig. 34. In the inter-laminar thickness tool, the parting surface needs to be determined first. The process is given as follow: 1) binarizing the CT image and computing the grey value, 2) defining the grey value of each pixel in the image as the energy function, 3) connecting the seed points on the minimum-energy continuous path in the inter-laminar region to form a parting line, 4) performing steps 1)–3) on each 2D images to form the parting surface in 3D. After the parting surface was determined, increasing the grey value of the highlighted fibre edges and calculating the distance between the nearest carbon microfibers and the point on the parting surface. In the aspect of void quantification, it was determined by identifying the darkest voxels associated with voids and grouping the voxels into 3D clusters. Setting the parting surface as the basis surface, the voxels located in the region 7 μm above and below the parting surface were classified into inter-laminar voids. The thickness of 7 μm is based on an assumed inter-laminar thickness of 14 μm which was twice the diameter of the carbon fibre used in this study). Other voxels were identified as intra-laminar voids. Based on the processed CT images, some new features were observed such as tow-aligned resin pockets (significant increase of inter-laminar

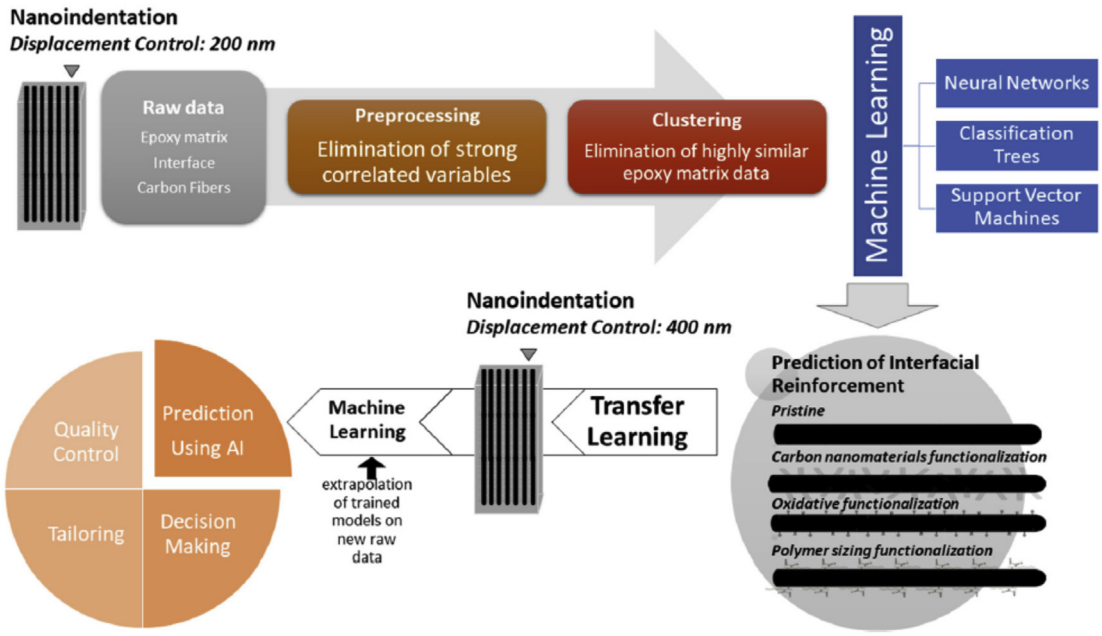

Fig. 33 – Workflow of identifying the interface mechanism in CFRPs using machine learning. [123] (Permission granted).

thickness in CT images), individual misplaced fibres (Fig. 35), and sub-microvoids. They have been not linked to composite damage initiating, propagation, damage resistance, and failure yet. In further research, these features (i.e., tow-aligned resin pockets, individual misplaced fibres, and sub-microvoids) can be scanned by in-situ μCT before and after loading to observe their propagation during the loading. It should be noted that the 3D dataset usually consists of a large number of 2D images, requiring a highly efficient data processing tool.

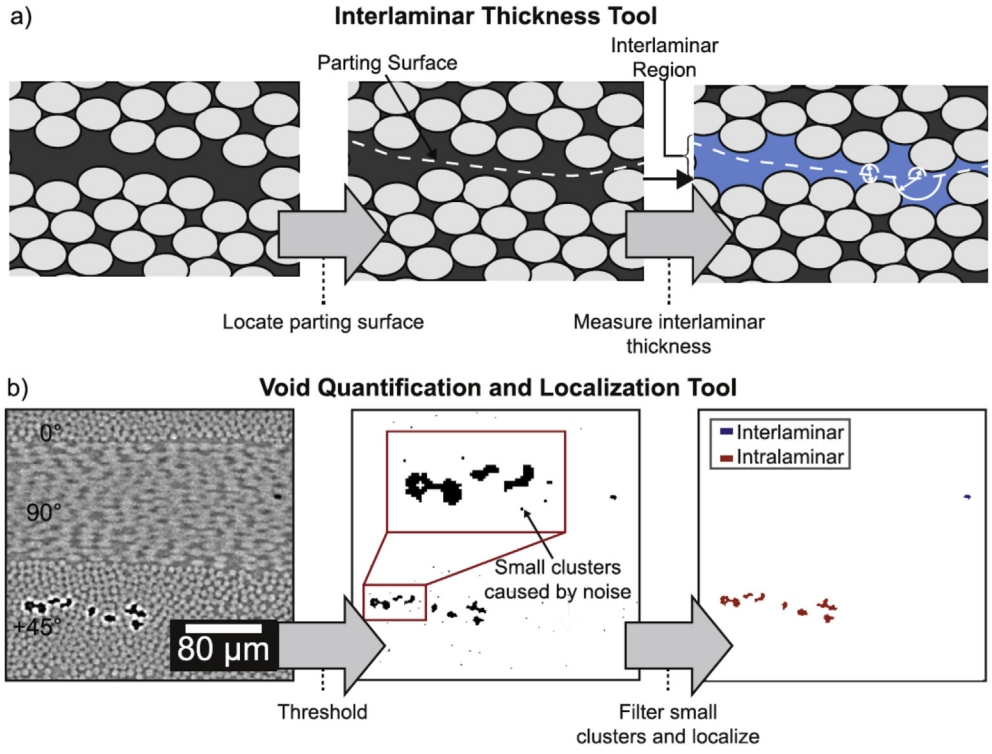

Fig. 34 – Flowchart describing the function of the automated analysis tools used in this work utilizing μCT datasets. (a) interlaminar analysis tool and (b) voids qualification and localization [124] (Permission granted).

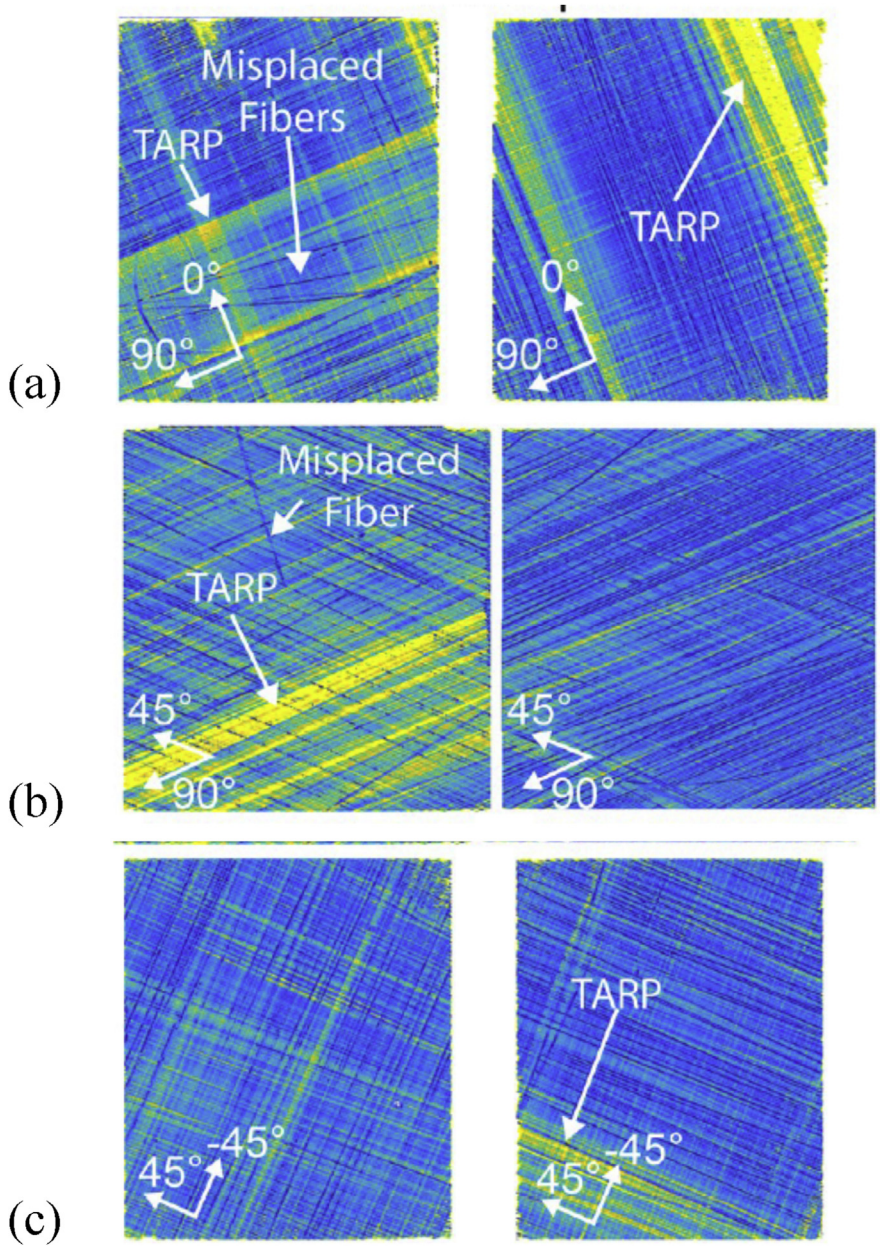

Fig. 35 – Interlaminar thickness maps of representative interlaminar regions of [0/90/±45]s CFRP laminates: (a) 0/90 interface, (b) 90/+45 interface and (c) +45/−45 interface [124] (Permission granted).

2.4. *Simulation of interface*

Although mechanical tests can evaluate interfacial shear strength and morphology observation can help to explain interface mechanisms, as discussed in Subsection 2.3.2 and 2.3.3, they cannot observe the changing process of the interfacial properties (including shear stress and morphology changes) during the whole debonding process. In the simulation, however, the debonding of the interface can be described mathematically and presented visually by each simulating step in both local and global coordinates. Therefore, the observation on the debonding process of the interface can be obtained through interface simulation. This section introduced interface simulations in the finite element method (FEM), discrete element method (DEM), and molecular dynamic (MD) method. A summary of the models, force fields, and corresponding mechanical tests on the FRP composite, and interface simulations by FEM, DEM, and MD is presented in Table 7. In the following section, the details are discussed.

2.4.1. *Finite element method (FEM) model*

The FEM is the most commonly used approach to simulate behaviour of composite material (e.g. mechanical properties, crack initiation, and propagation) under various loading conditions (e.g. quasi-static, vibration, and dynamic loadings) at different scale lengths (e.g. microscale, mesoscale, and

Table 7 – The simulation method of the interface.

Simulation method	Models	Corresponding test
FEM	1. Continuum damage model 2. Cohesive zone model 3. Coulomb friction model	1. Interface tests (fibre pull-out, fibre push-in and in-plane shear test) 2. Interlaminar test (Mode I/II/III Fracture tests, short beam shear test) 3. Tensile, compressive, impact, and bending tests
DEM	1. Linear contact model	1. Tensile and compressive tests
MD	1. Polymer consistent force field (PCFF) 2. Consistent valence force field (CVFF) 3. Assisted model building with energy refinement (AMBER) force field	1. Fibre pull-out test

macroscale) [125]. Moreover, the simulation can combine mechanical and thermal loads to formulate complex loading conditions (e.g. thermo-mechanical cyclic loading [126]). In FEM, the material response (e.g., stress and strain) and relationships among material parameters are described by constitutive models. Continuum damage model (CDM), cohesive zone model (CZM), and Coulomb friction model are typical constitutive models.

2.4.1.1. Continuum damage model (CDM). The CDM is a phenomenological model based on continuum damage mechanics. When the CDM is applied to simulate the fibre/matrix interface and inter-laminar interface, the relationship between the damage propagation and stiffness degradation needs to be established in a solid element [127]. The damage evolution is achieved by using the scalar damage parameter (d_i, where i denotes the element i) to describe the stiffness degradation, as shown in Eq. (23). The range of the damage parameter is from 0 to 1, in which $d_i = 0$ represents the initial state and $d_i = 1$ means complete debonding state. The $\mathbf{C_0}$ and $\mathbf{C}$ are the stiffness matrix before and after the degradation, respectively.

$$\mathbf{C} = (1 - d_i) \cdot \mathbf{C}_0 \tag{23}$$

In the isotropic material with bi-linear stress–strain relation, the d_i can be derived from Eq. (24) [128].

$$d_i = \frac{\varepsilon_{u,i}(\varepsilon_i - \varepsilon_{n,i})}{\varepsilon_i(\varepsilon_{u,i} - \varepsilon_{n,i})} \tag{24}$$

where ε_i, $\varepsilon_{n,i}$ and $\varepsilon_{u,i}$ are the normal strain, softening onset strain, and ultimate strain in the softening process of element i, respectively.

Apart from determining the damage parameters by stress–strain relation, Babaei and Farrokhabadi [129] used the angle between each Gauss point of elements ($\theta_{Gausspoint}$) to determine the damage parameter of the fibre/matrix interface ($d_{int.}$). As shown in Fig. 36, the fibre and matrix elements were connected by interface elements where four Gauss points were in each element. The d_{int} was expressed by Eq. (25).

$$d_{int.} = \begin{cases} 0, & |\theta_{Gausspoint}| > |\alpha| \\ \approx 1, & |\theta_{Gausspoint}| \leq |\alpha| \end{cases} \tag{25}$$

The α was derived from Eq. (26)

$$\alpha = -E^{int.} \cdot \nu^f + E^{f\cdot} \cdot \nu^{int.} + E^{f\cdot} - E^{int.} \tag{26}$$

where the terms $E^{int.}$, $E^{f\cdot}$ and $\nu^{int.}$, ν^f were the elastic modulus and Poisson's ratio of the interface and fibre, respectively.

For orthotropic materials such as FRP laminates, various damage parameters are necessary to reduce the material stiffness in different directions. For example, Wang et al. [130] introduced d_f, d_m and d_s to denote the fibre breakage (longitudinal direction) and matrix cracking (transverse direction) and shear failures, respectively. As the shear failure is dependent on the longitudinal and transverse cracks, in linear softening material, the d_s of linear softening material is given by Eq. (27) [130], as follows:

$$d_s = 1 - \left(1 - d_f^t\right)\left(1 - d_f^c\right)\left(1 - d_m^t\right)\left(1 - d_m^c\right) \tag{27}$$

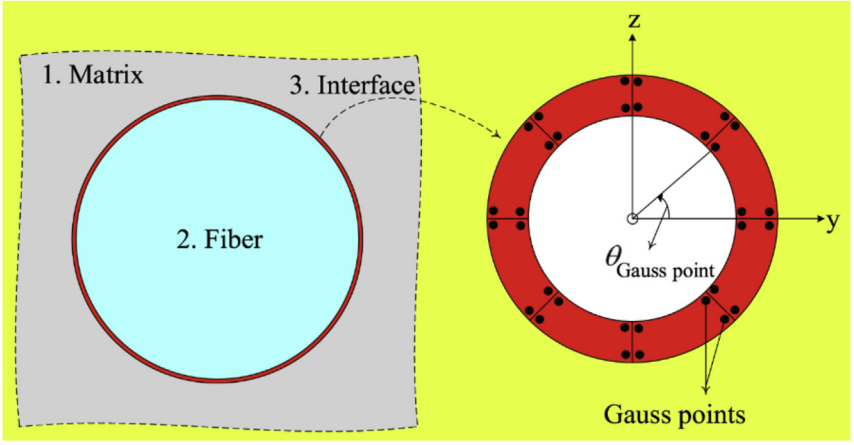

Fig. 36 – The angle between each Gauss point of interface elements [129] (Permission granted).

where d_f^t, d_f^c, d_m^t and d_m^c represent the damage parameters of fibre in tension, fibre in compression, matrix tension, and matrix in compression, respectively.

Maimí et al. [131] introduced three types of damage variables (d_N, N = 1±, 2± and 6 represent the longitudinal, transverse and shear damage, respectively) as well. And N = 1+, 1 − , 2+ and 2− means longitudinal tension, longitudinal compression, transverse tension and transverse compression, respectively. Especially, the internal variable r_M (M = 1+, 1 − , 2+ and 2 −) defining the threshold of the elastic domains was used to determine d_N. The term r_M was associated with the loading function, which was dependent on the strain tensor and material properties (elastic modulus and strength). In the research of Maimí et al. [132], the exponential damage evolution law was used in the FRP laminates. The general form of damage parameters is expressed in Eq. (28)

$$d_N = 1 - \frac{1}{f_M(r_M)} \exp\{A_N[1 - f_M(r_M)]\} \tag{28}$$

where $f_M(r_M)$ is a function having the same order as the damage activation function to indicate the softening initiation. The damage activation function (F_{1+}, F_{1-}, F_{2+} and F_{2-}) came from the LaRC04 criteria [131], as presented in Table 8. The A_N is the adjusting parameter calculated from the fracture toughness of the material, which is expressed as Eq. (29).

$$g_N(A_N) - \frac{G_N}{l^*} = 0 \tag{29}$$

where G_N is the energy release rate, g_N is the energy dissipated per unit volume, and l^* is the characteristic length of the finite element.

To consider the influence of temperature and moisture on the FRP, they (Maimí et al. [131,132]) used the equation of the energy density containing damage variables, as follows:

$$G = \frac{\sigma_{11}^2}{2(1-d_1)\cdot E_1} + \frac{\sigma_{22}^2}{2(1-d_2)\cdot E_2} - \frac{\nu_{12}}{E_1}\cdot\sigma_{11}\cdot\sigma_{22} + \frac{\sigma_{12}^2}{2(1-d_6)\cdot G_{12}} + (\alpha_{11}\cdot\sigma_{11} + \alpha_{22}\cdot\sigma_{22})\cdot\Delta T + (\beta_{11}\cdot\sigma_{11} + \beta_{22}\cdot\sigma_{22})\cdot\Delta M \tag{30}$$

where E_1, E_2, ν_{12} and G_{12} are the in-plane elastic orthotropic properties (elastic modulus, major Poisson's ratio, and shear modulus) of a unidirectional lamina. The α_{11}, α_{22} and β_{11}, β_{22} are the coefficients of thermal expansion and hygroscopic expansion in the longitudinal and transverse directions, respectively. The ΔT and ΔM are the differences in temperature and moisture content, respectively.

The strain tensor is the derivate of the energy density, which is expressed in Eq. (31):

$$\varepsilon = \frac{\partial G}{\partial \sigma} = \boldsymbol{H} : \sigma + (\alpha_{11} + \alpha_{22})\cdot\Delta T + (\beta_{11} + \beta_{22})\cdot\Delta M \tag{31}$$

where $\boldsymbol{H}$ is the compliance tensor as follows:

$$\boldsymbol{H} = \frac{\partial^2 G}{\partial^2 \sigma} = \begin{bmatrix} \frac{1}{(1-d_1)\cdot E_1} & -\frac{\nu_{12}}{E_1} & 0 \\ -\frac{\nu_{12}}{E_1} & \frac{1}{(1-d_2)\cdot E_2} & 0 \\ 0 & 0 & \frac{1}{(1-d_6)\cdot G_{12}} \end{bmatrix} \tag{32}$$

González et al. [133] applied the model from Maimí et al. [131,132] to simulate the drop-weight impact test on the unidirectional FRP laminate, and further applied compression on the impacted FRP laminate. The simulation can describe the failure of interlaminar and ply during the test. Furthermore, Maimí et al. [134] developed the previous CMD model to a fully 3D damage model to describe the inter-laminar and intra-laminar failure mechanisms without pre-setting the crack plane. Considering the dimensional expansion, the energy density is modified as follows:

Table 8 – The damage activation functions and corresponding loading functions in LaRC04 criteria.

Damage activation function	Loading functions (φ_{1+}, φ_{1-}, φ_{2+} and φ_{1-})
$F_{1+} = \varphi_{1+} - r_{1+} \le 0$	$\varphi_{1+} = \frac{\tilde{\sigma}_{11} - \nu_{12}\cdot\tilde{\sigma}_{22}}{X_T}$
$F_{1-} = \varphi_{1-} - r_{1-} \le 0$	$\varphi_{1-} = \frac{\left\lvert\tilde{\sigma}_{12}^m + \nu_{12}\cdot\tilde{\sigma}_{22}^m\right\rvert}{S_L}$
$F_{2+} = \varphi_{2+} - r_{2+} \le 0$	$\varphi_{2+} = \begin{cases} \sqrt{\left(1 - \frac{G_{Ic}}{G_{IIc}}\right)\frac{\tilde{\sigma}_{22}}{Y_T} + \frac{G_{Ic}}{G_{IIc}}\left(\frac{\tilde{\sigma}_{22}}{Y_T}\right)^2 + \left(\frac{\tilde{\sigma}_{12}}{S_L}\right)^2}, \tilde{\sigma}_{22} \ge 0 \\ \frac{1}{S_L}\left\lvert\tilde{\sigma}_{12}\right\rvert + \eta^L\tilde{\sigma}_{22}, \tilde{\sigma}_{22} < 0 \end{cases}$
$F_{2-} = \varphi_{2-} - r_{2-} \le 0$	$\varphi_{2-} = \sqrt{\left(\frac{\tilde{\tau}^T}{S_T}\right)^2 + \left(\frac{\tilde{\tau}^L}{S_L}\right)^2}$

where $\tilde{\sigma}_{11}$, $\tilde{\sigma}_{22}$ and $\tilde{\sigma}_{12}$are effective stress tensors; $\tilde{\sigma}_{12}^m$ and $\tilde{\sigma}_{22}^m$ represent effective stress tensors with the fibre misalignment. X_T and Y_T are tensile strength in fibre direction and normal to the fibre direction, respectively.η^L is the longitudinal friction coefficient. G_{Ic} and G_{IIc} are energy release rate in mode I and mode II. S_L andS_T are longitudinal and transverse shear strength, respectively. $\tilde{\tau}^T$ and $\tilde{\tau}^L$ are effective longitudinal and transverse shear stress, respectively.

$$G_{3D}=\frac{\sigma_{11}^2}{2(1-d_1)\cdot E_1}+\frac{1}{2E_2}\left(\frac{\sigma_{22}^2}{1-d_2}+\frac{\sigma_{33}^2}{1-d_3}\right)-\frac{\nu_{12}}{E_1}\cdot\sigma_{11}\cdot(\sigma_{22}+\sigma_{33})$$
$$-\frac{\nu_{23}}{E_2}\cdot\sigma_{22}\cdot\sigma_{33}+\frac{\sigma_{12}^2+\sigma_{13}^2}{2(1-d_6)\cdot G_{12}}+[\alpha_{11}\cdot\sigma_{11}+\alpha_{22}\cdot(\sigma_{22}+\sigma_{33})]\cdot\Delta T$$
$$+[\beta_{11}\cdot\sigma_{11}+\beta_{22}\cdot(\sigma_{22}+\sigma_{33})]\cdot\Delta M \tag{33}$$

where the direction of d_1, d_2 and d_3 are defined by a set of orthonormal vectors $[e_1, e_2, e_3]$; the ν_{23} is the minor Poisson's ratio.

Then the compliance tensor H is updated as Eq. (34):

$$H=\frac{\partial^2 G_{3D}}{\partial\sigma\otimes\partial\sigma} \tag{34}$$

With the 3D model (Maimí et al. [134]), the delamination procedure of notched FRP laminate subjected to longitudinal tension was predicted fairly well: the notched ply in the FRP triggered the delamination between the central ply and the adjoining plies, followed by the propagation of delamination in mode II along the longitudinal direction.

Based on the model of Maimí et al. [134], Salavatian and Smith [135] studied in-plane shear modulus reduction concerning the effect of internal traction and crack closure on the in-plane shear modulus. Melro et al. [136] used the 3D models from Maimí et al. [134] to simulate the response of woven fabric reinforced polymer in various load conditions (tension and shear). A 5-harness satin weave was chosen as the representative unit cell in the "infinite" length of the fabric reinforced polymer, as shown in Fig. 37. In the uniaxial tension, the load is applied along the warp (horizontal) yarns, and the damage accumulated in the weft yarns propagates to the matrix which causes the final failure of the weave. Under a pure shear load, the damage tends to be located along the edges of the yarns where there is bonded to the matrix.

2.4.1.2. Cohesive zone model (CZM). In the FE method, the cohesive zone is established in the element with zero thickness, compared with the CDM in the solid element having a defined thickness. The CZM element can be calculated in the cohesive elements in Abaqus [137–140] and contact elements in ANSYS [141]. In CZM, the interface stress is calculated based on the cohesive traction-separation law, which is characterized as a relationship between a cohesive traction vector (σ_n) and displacement separation vector (δ_n) [142]. There are several commonly used forms of the traction-separation law in Fig. 38. The first two forms (linear softening and constant forms) describe the traction-separation law after the cohesive traction has attained an initial peak value σ_c, and the cohesive traction decreases linearly or vanishes when the displacement reaches the maximum separation of δ_c. Figure 38(a) shows the linear softening law which is appropriate for quasi-brittle materials such as ceramics and concrete [143]. The constant form traction-separation law is used to describe the plasticity of the crack tip in ductile metals [143]. The other four traction-separation laws consider both the softening region and the initial region in which the traction increases to the initial peak value (σ_c) in a specific matter as the displacement increases to the separation point (δ_0). In bi-linear and trapezoidal forms, the initial and softening regions are linear. Specially, the trapezoidal form contains a plateau (δ_0–δ_1) which is used to describe the crack growth resistance in

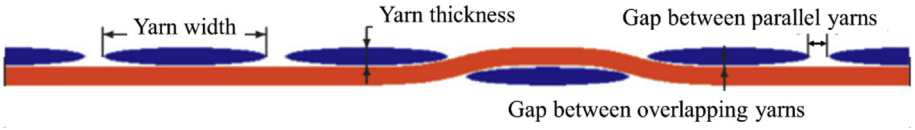

Fig. 37 – The structure of the 5-harness satin weave [136] (Permission granted).

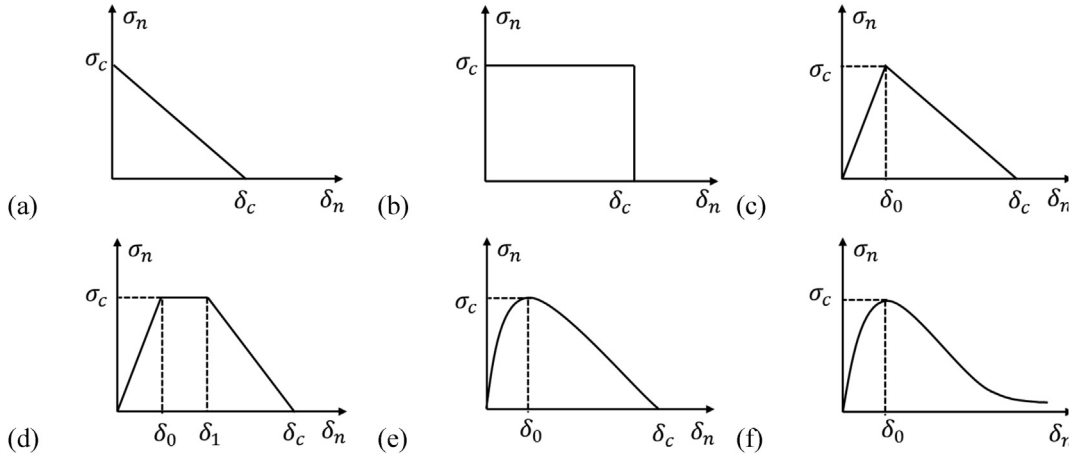

Fig. 38 – Different shapes of the cohesive traction-separation law: (a) linear softening form; (b) constant form (Dugdale Model); (c) bi-linear form; (d) trapezoidal form; (e) polynomial form; (f) exponential form; redrawn from [142] (Permission granted).

elasto-plastic materials [144]. In Fig. 38(e) and (f), the traction-separation laws are presented as polynomial and exponential relationships, respectively [90].

All the last four forms are usually utilised in the interface simulation of FRP materials [144–149]. The bi-linear traction-separation law is the simplest approach due to its monotonicity and continuity. Jia et al. [145] simulated the debonding progress of a carbon fibre–epoxy interface in the single fibre pull-out test by using bi-linear traction-separation law in Abaqus cohesive elements. In the simulation, the matrix embedded with a fibre was simplified as a semi-infinite matrix with a cylindrical fibre, as shown in Fig. 39(a). The R and l_e represent the radius of the fibre and the embedded fibre length, respectively. The pull-out force was applied uniformly on the top surface of the fibre in the axial direction. The assumptions include 1) the pull-out process is static, 2) the fibre will not break before the debonding happens, 3) the debonding initiates at the fibre–matrix interface and propagates longitudinally along with the carbon fibre, and 4) the normal stress along the fibre is smaller than the ultimate strength of the fibre material, which means the fibre will not fracture before it is pulled out. The model described in Fig. 39(a) is symmetric, therefore it can be simplified further to a two-dimensional axisymmetric model as constructed is shown in Fig. 39(b). The radial and axial constraints were applied on the bottom of the model whilst the side along the axisymmetric axis was constrained only in the radial direction. The cohesive zone between the fibre and matrix was defined as the four-node, axisymmetric cohesive elements (COHAX4). The bilinear traction-separation law (Fig. 38(c)) was implemented in these cohesive elements. The key parameters (i.e., σ_c, δ_0 and δ_c) were determined by experimental curve fitting from the single fibre pull-out test. Based on the cohesive elements, Jia et al. [145] found out that the fibre pull-out energy per unit interfacial area (namely specific pull-out energy) is independent of the fibre radius but increases with the increases of the embedded length which can enhance the interfacial friction.

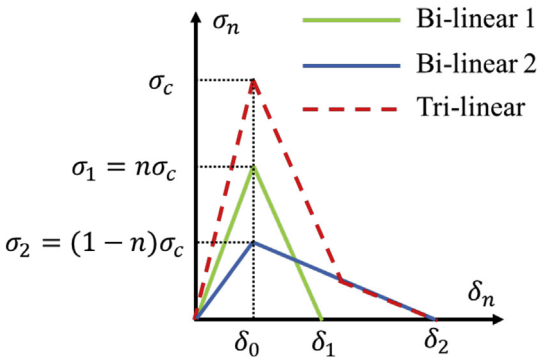

Fig. 40 – Tri-linear cohesive law based on two bi-linear laws, redrawn from Ref. [144] (Permission granted).

Recently, a tri-linear cohesive law which is a superposition of two bilinear cohesive laws has been proposed to represent different fracture mechanisms (such as quasi-brittle fracture of the matrix and fibre bridging) in the simulation of laminated composites [144]. As shown in Fig. 40, the two solid lines represent two bi-linear cohesive laws which have the same initial separation displacement (δ_0) but different initial peak stress (σ_1 and σ_2) as well as maximum separation displacements (δ_1 and δ_2). Heidari-Rarani and Ghasemi [144] studied the delamination of unidirectional glass fabric/epoxy laminate by end-notched flexure (ENF) test and FE simulation implemented a tri-linear cohesive law. In the simulation, the Bi-linear 1 with a shorter maximum separation displacement (δ_1) was used to characterize the quasi-brittle fracture in the matrix while the Bi-linear 2 with a longer maximum separation displacement (δ_2) was applied to characterize the fibre bridging. The FE model in the ABAQUS code is divided into two parts. One part was the specimen formed by 2D plane strain elements (CPE4). Another part was the delamination section which was built by 2D linear quadrilateral cohesive elements (COH2D4) and located in the pre-crack of ENF specimen along

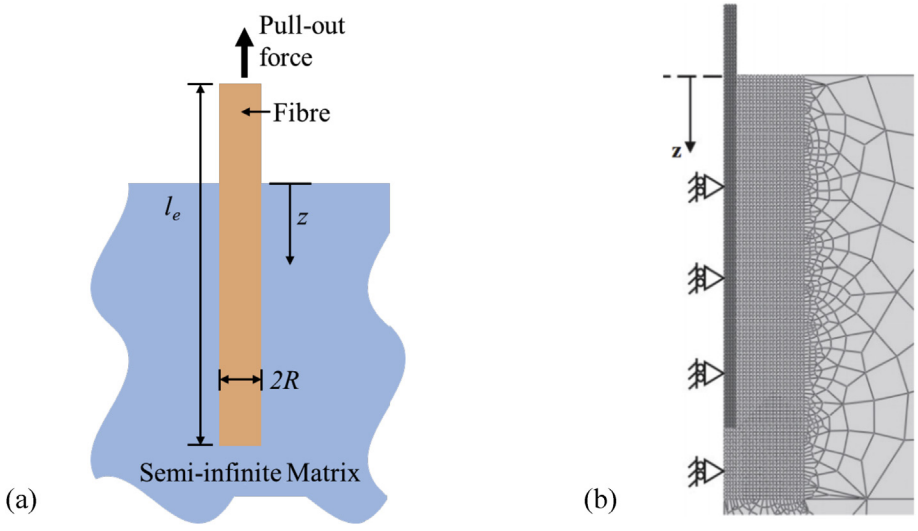

Fig. 39 – (a) The fibre pull-out model; (b) the axisymmetric finite element model for a single carbon fibre pull-out [145] (Permission granted).

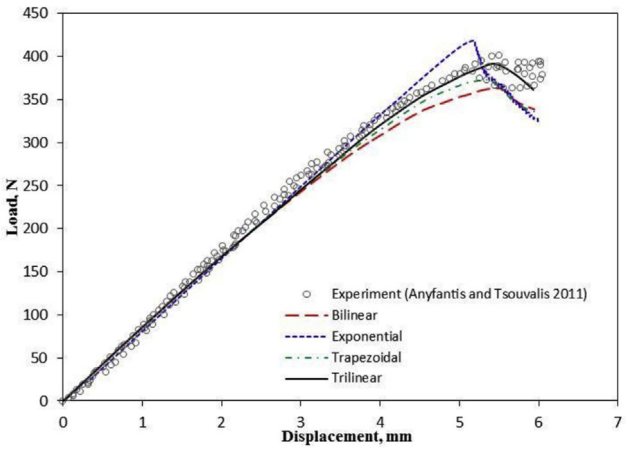

Fig. 41 – Simulation results of various shapes of cohesive law respect to experiments [144] (Permission granted).

the potential delamination direction. The authors also performed FE simulation based on bi-linear, trapezoidal, and exponential cohesive laws. The comparison between the experimental and simulation results is shown in Fig. 41. The superposed tri-linear law had better agreement with the experimental results due to its superposition of two bi-linear cohesive laws which can justify the two damage mechanisms (quasi-brittle fracture in the matrix and fibre bridging) at the crack tip.

Zhuang et al. [150] investigated the failure of FRP laminate under half-hole pin bearing by the combination of CDM and CZM. The CDM models with bi-linear softening law and smeared crack law [151] were used to simulate intra-laminar damage propagation in the longitudinal and transversal directions, respectively. The CZM accounted for the inter-laminar failure. In the research, the damage propagation at the bearing plane of the FRP laminate was observed by an optical microscope (magnification factor: 5) and recorded by a digital camera. Compared with the micrographs recorded during the test, the simulation can capture well the influence of the ply thickness and sequence on the bearing strength. For further study, Zhuang et al. [152] simulated the double-shear and single-shear composite bolted joints with different configurations and geometries. Different from the previous study, in this updated model, the inherent cohesive-frictional behaviour was considered in the intra-laminar transverse and delamination failure procedure. The damage-friction coupling method of Alfano and Sacco [153] was adopted to describe the influence of friction effects on the inter-laminar failure. Through this model, the critical failure which was responsible for the structural failure can be identified. For example, in bolted FRP joints, the FRP delamination outside the washer edge was caused by accumulated shear cracks in bearing failure mode.

Tserpes and Koumpias [128] compared the Mode I fracture simulation based on CDM and CZM in the 3D model. The linear-softening law and the exponential traction law were applied in CDM and CZM models, respectively. The maximum load and initial stiffness predicted by both CDM and CZM models had a good agreement (the error range was less than 5%) with the values obtained from the double cantilever beam tests. However, the predictions of the CDM were more dependent on the mesh density than the CZM. The same phenomenon was founded by Sugiman and Ahmad [154] by simulating the single-lap shear test on an adhesively bonded joint by CDM and CZM. In CDM, as the mesh size increased 0.05 mm, the change of the maximum load was around 5%. In CZM, however, as the mesh size increased 0.8 mm, the change of the maximum load was only 0.3%. Moura and Chousal [127] performed a 2D simulation on the Mode II fracture toughness tests through both CDM and CZM. The end-notched flexure (ENF) test was used to determine the Mode II fracture toughness of the bonded joint. Based on the load–displacement curves obtained from the simulation, the energy release rates were calculated and compared with the experimental results. The equivalent crack was introduced to reflect the influence of the fracture process region which was near the crack tip on the fracture toughness. In the fracture process region, the material undergoes softening damage, but the crack had not been generated. In the simulation, the total strain energy of all points in the fracture process region was regarded as the energy to form an equivalent crack. The summary of the generated crack and the equivalent crack was the true crack length in both CZM and CDM simulation. The CZM displayed better agreements in the calculated fracture toughness with the experimental value than the CDM model due to that the normal stresses at the crack tip in CDM dissipated the energy for the equivalent crack.

2.4.1.3. Coulomb friction model. Coulomb friction model describes the shear stress before the sliding of two contact surfaces. The shear stress (τ) is expressed as Eq. (35):

$$\tau = \mu \cdot \sigma_c \tag{35}$$

where μ and σ_c are the friction coefficient and normal pressure stress of interface, respectively.

Coulomb friction model is usually used to simulate the interface debonding process in the fibre pull-out test [155], micro-bond test [156,157], and fibre push-out test [158]. Zhi et al. [156] studied the influence of fibre diameter on the interfacial shear strength between polyester fibre and epoxy in the micro-bond test. The interface between the fibre and epoxy droplet was simulated using the Coulomb friction model with a constant friction coefficient of 0.5. As shown in Fig. 42, the SOLID 185 element was used to simulate the fibre and the droplet. Contact elements CONTA174 and TARGE170 were assigned the contact surface on the fibre and the target surface on the droplet, respectively.

The droplet was assumed to be isotropic, and its state was described using maximum distortion strain energy criterion (i.e., once the deformation of a point in a material reaches the maximum value of uniaxial stress state, the yield failure occurs in the material), as presented in Eq. (36).

$$\left\{\frac{1}{2}\left[(\sigma_{d1}-\sigma_{d2})^2+(\sigma_{d2}-\sigma_{d3})^2+(\sigma_{d3}-\sigma_{d1})^2\right]\right\}^{1/2} \leq {\sigma_d}^2 \tag{36}$$

where σ_{d1}, σ_{d2} and σ_{d3} are the first, second and third principal stress of the droplet, respectively, and σ_d is the yield strength of the droplet.

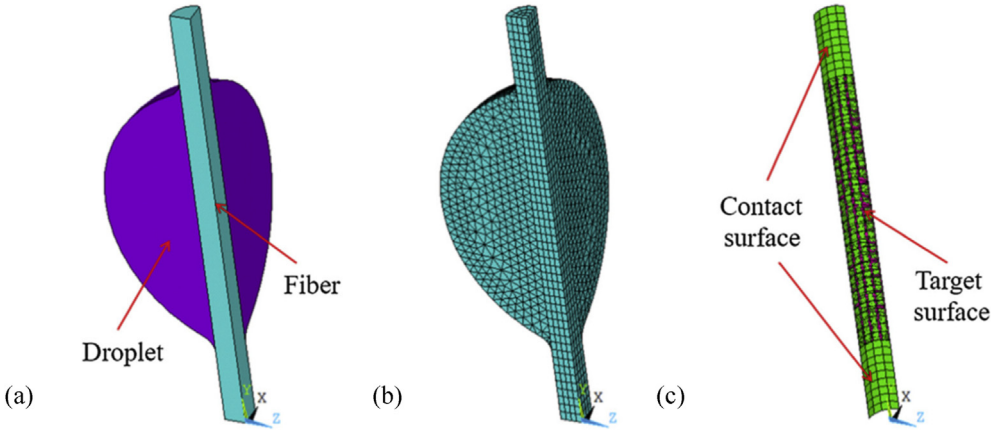

Fig. 42 – Finite element model of (a) droplet and fibre, (b) mesh scheme and (c) contact elements [156](Permission granted).

The debonding process was assumed as a pure shear state. Therefore, $\sigma_{d1} = \tau_{fd}$, $\sigma_{d2} = 0$ and $\sigma_{d3} = -\tau_{fd}$, where τ_{fd} is the shear stress between the fibre and matrix droplet. Hence, Eq. (36) can be simplified as Eq. (37) When τ_{fd} reaches the maximum value, the contact surfaces started to slide.

$$\tau_{fd} \leq \sigma_d \Big/ \sqrt{3} \tag{37}$$

According to the simulation results, the shear stress between fibre and droplet decreased as the fibre diameter increased, which was in agreement with the experimental results. This phenomenon was attributed to that the smaller fibre diameter led to higher contact friction stress points and increase the interfacial shear strength.

In the simulation of pull-out and push-out tests, fibre is mostly assumed as straight. In nanocomposite, nanotubes are typically curved and entangled. Chen et al. [159,160] simulated the debonding of the curved and entangled nano-fibres from the polymer matrix based on Coulomb friction model. The radial compressive stress at fibre/matrix interface was considered during the pull-out of the curved fibre. The simulation could clearly describe the interfacial stress distribution along the curved fibre revealed that fibres with more curvature and longer embedded length need higher force and energy for debonding initiation. Additionally, the Coulomb friction law has been coupled with CZM to simulate the debonding and the sliding process between the fibre and matrix. Nian et al. [157] proposed the interface model by incorporating a Coulomb friction law into the bilinear traction-separation law (as shown in Fig. 43(a)) to simulate the debonding between the glass fibre and epoxy in the microbond test. Compared with the traditional bilinear traction-separation law, only one additional parameter τ_f (i.e., the frictional stress in the pure frictional stage) was introduced. The coupled interface model gave a good prediction of the load–displacement curve in comparison with the results of microbond test, as shown in Fig. 43(b).

In the FE simulation discussed above, the fibres and fabric are regarded as a continuum and cannot be separated during the debonding process. However, plant-based fibres such as flax and hemp fibres contain fibre bundles that consist of single fibres and have natural defects (e.g., kink band). These two features may lead to the bundle and fibre damage and fail to form a pure shear state during the fibre–matrix debonding. Therefore, the separation of fibres in a bundle and fibre defects need to be considered in the debonding of fibre–matrix. Sliseris et al. [161] used brittle material laws obtained from the single fibre tensile test to describe the flax fibre defects and the relationship between fibres in a bundle through the finite element method. The representative volume element (RVE) with the size of 2 mm was applied to guarantee that all fibres (maximum length was 1.9 mm) were included in the RVE. After applying tension load in the vertical direction, the failure mode from the simulation captured accurately the fibre breakage initiated at the fibre defects and the splitting of fibre bundle as shown in Fig. 44 (black and red points).

2.4.2. *Discrete element method (DEM) model*

In a DEM model, the bulk material such as glass fibre, carbon fibre, and epoxy are assembled by discrete particles. The information of each particle and contact between joint particles can be recorded individually and updated dynamically [162]. Therefore, DEM is convenient to simulate the local debonding problem. Ismail et al. [162] simulated the unidirectional FRP by representative area element. Specifically, the matrix and fibres were simulated by disc particles. The connection between particles in pure matrix and fibres was parallel bonds, as shown in Fig. 45. In the parallel bond model, a set of elastic springs are distributed evenly on the contact plane and centred at the contact point; these springs are used to resist the moment caused by particle rotation [163]. The fibre–matrix interface was described by a displacement-softening model. When the transverse tensile stress was applied to the DEM model, simulation results showed that the interfaces had higher stress than the matrix or fibre, especially in the areas with high fibre densities. According to the simulation, tension cracks usually began with interfacial debonding. The final catastrophic fracture of composite material was caused by the combination of the interfacial and matrix micro-cracks. In the 2D DEM model, fibres have the same direction; whilst there is more flexibility of fibre direction in 3D DEM model. However,

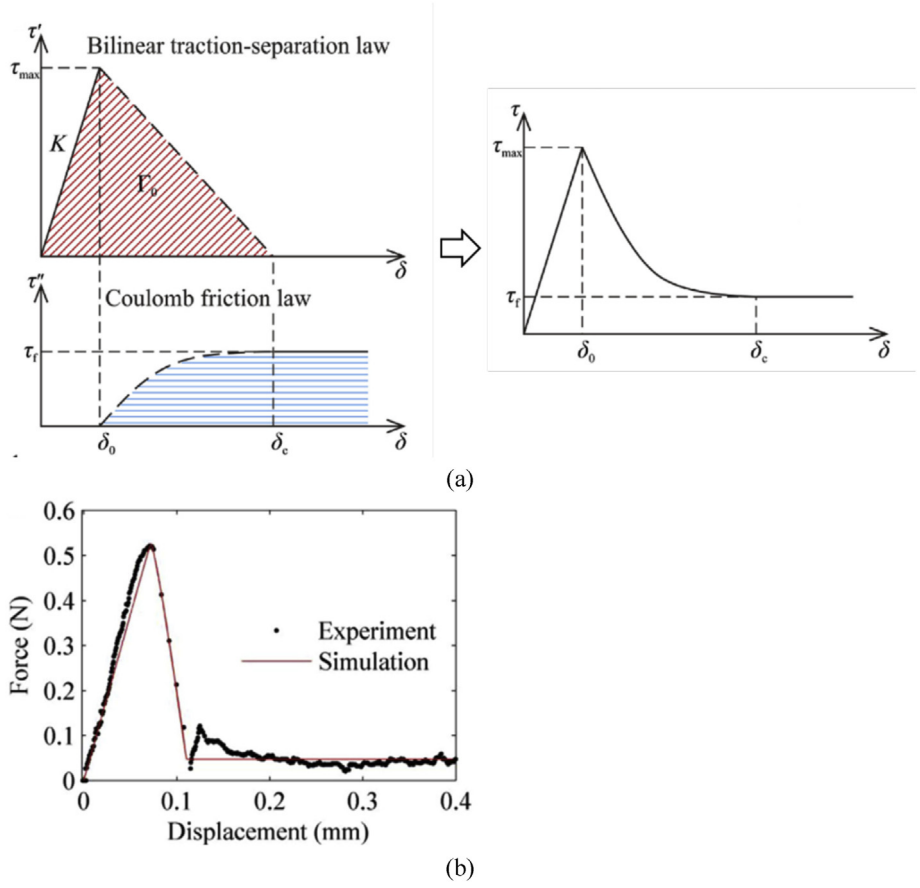

Fig. 43 – (a) The traction-separation law combining a Coulomb friction law and bilinear traction-separation law; (b) the comparison between the load–displacement curves from the simulation and experiment results [157] (Permission granted).

the simulation of fibre–polymer interface in 3D DEM is still lacking.

2.4.3. *Molecular dynamics (MD) simulation*

Molecular dynamics (MD) simulation can be utilized to understand the interaction between the reinforcement and matrix at the atomistic level. In MD simulations, the atoms and molecules are regarded as a collection of interacting classical particles [164]. The trajectories of atoms and molecules are determined based on Newton's equations of motion [165]. According to the trajectory, various structural and dynamic properties of the system can be calculated [164]. MD

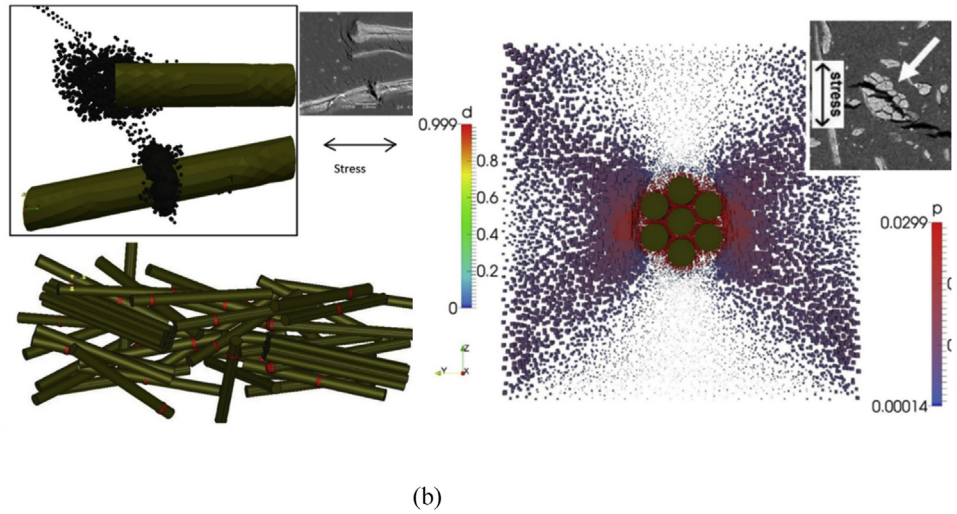

Fig. 44 – The simulation results with corresponding SEM figures from experimental results: (a) the damage of single fibre and (b) the splitting of fibre bundle [161] (Permission granted).

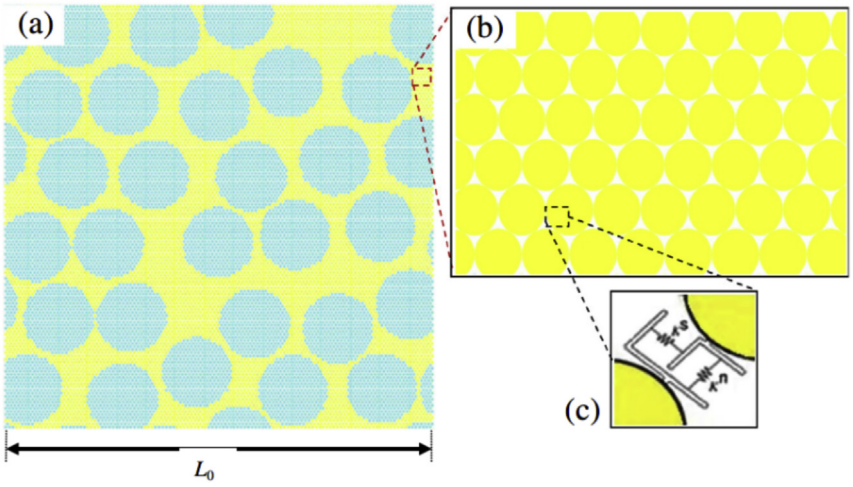

Fig. 45 – Fibre distribution and discrete element discretisation: (a) representative area element; (b) hexagonal packing arrangement; (c) contact between particles [162] (Permission granted).

simulation is performed using empirically parameterized force fields which describe the relationship between the molecule energy and molecule structure. For instance, in the MD simulation of polymer-based composite, commonly used force fields include polymer consistent force field (PCFF) [166,167], consistent valence force field (CVFF) [168], and the assisted model building with energy refinement (AMBER) force field [169,170].

In the research by Xiong and Meguid [166] the MD simulations of CNT reinforced epoxy composites were performed based on PCFF. This research investigated the influence of epoxy density, length, and diameter of a CNT, and the CNT–epoxy interphase thickness on the interfacial properties (e.g., pull-out force and interfacial shear strength and interaction energy). The single polymer molecular chain and CNT are exhibited in Fig. 46(a) and (b). The analytic form of the energy expression used in the PCFF is presented in Eq. (38):

$$E_{pot} = E_{bond} + E_{angle} + E_{dihedral} + E_{vdWaals} + E_{Coulomb} \quad (38)$$

where E_{pot}, E_{bond}, E_{angle}, $E_{dihedral}$, $E_{vdWaals}$, and $E_{Coulomb}$ are the potential energy of the total system, PCFF bond, PCFF angle, PCFF dihedral effect, van der Waals interaction, and Coulombic interaction, respectively.

During the simulation, the load end of the CNT was pulled at a uniform velocity of 1×10^{-5}Å per femtosecond. The free end of the CNT was pulled out completely from the epoxy matrix. The interfacial shear strength (IFSS) was determined based on the change of total energy, as presented in Eq. (39)

$$\Delta E = \pi r_{CNT} \tau_i l_e^2 \quad (39)$$

where ΔE is the difference in total energy of the CNT–epoxy, r_{CNT} is the radius of CNT, l_e is the embedded length of CNT, and τ_i is the IFSS. According to the simulation results, the increase of length and diameter of a CNT, and the thickness of CNT–epoxy matrix interface resulted in a decrease of interfacial shear strength.

Xiao and Xian [168] studied the mechanism of how moisture affects the interfacial bonding in carbon fibre–epoxy resin using MD simulation based on CVFF and the micro-bond experiment. In order to simulate the moisture condition, 23,586 water molecules (density: 1 kg/m^3) were assigned to the carbon fibre–epoxy interfacial system. The moisture condition simulation results indicated that the surface free energy

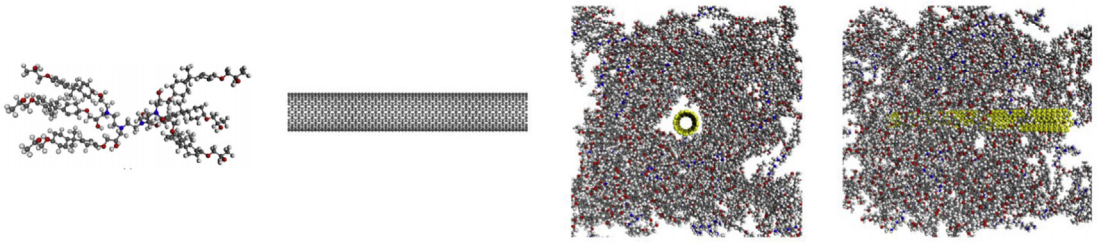

Fig. 46 – (a) Molecular model of a single diglycidyl ether of bisphenol-A–triethylene-triamine (DGEBA–TETA) epoxy chain; (b) molecular model of a single-walled CNT; (c) front and (d) lateral views of the computational model of the CNT–epoxy composite [166] (Permission granted).

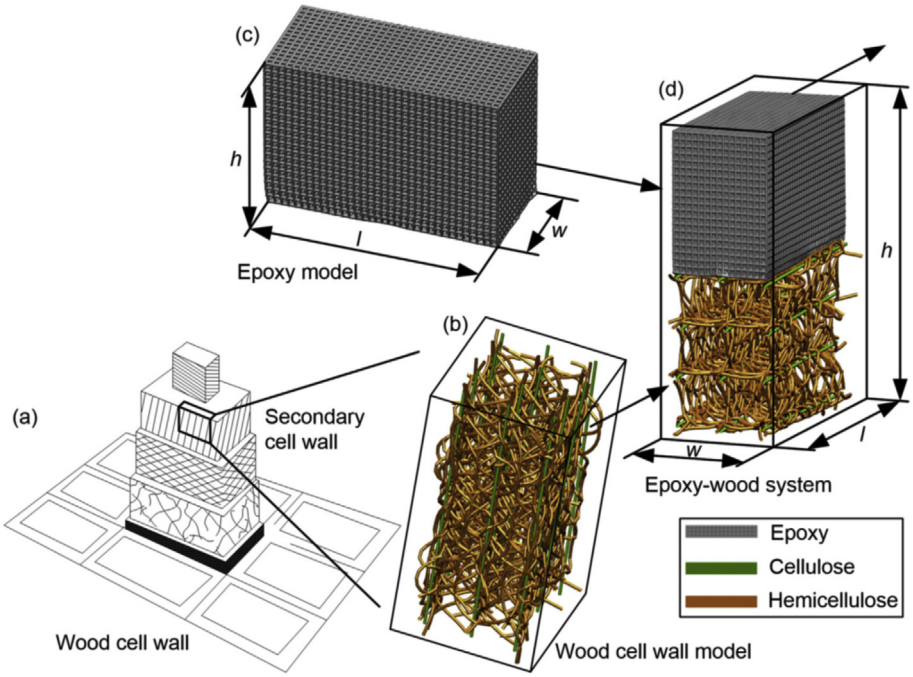

Fig. 47 – The schematic diagram of (a) wood cell wall consisted of multiple layers; (b) wood cell wall model consisted of cellulose and hemicelluloses; (c) epoxy cross-linked structure with dimensions of 340 Å × 150 Å × 200 Å; and (d) mesoscale model of epoxy–wood material system with dimensions of 340 Å × 150 Å × 440 Å [167] (Permission granted).

was reduced by about 58%. This reduction was comparable with the drop of the interfacial shear strength tested by the micro-bond experiment. Moreover, the MD results revealed that the Coulomb forces between water and epoxy molecules were critical to the interfacial debonding process [168]. Tam et al. [171] investigated the effect of salt environment on the interface adhesion of carbon fibre–epoxy by MD simulation based on CVFF. The 5 wt% of sodium (Na^+) and chloride (Cl^-) ions were added into water molecules to simulate the salt environment. The simulation was subject to structural equilibration in the canonical ensemble at a constant temperature of 300 K for 2 ns with a time step of 1 fs. According to the simulation results, the salt solution leads to the largest loss of interfacial adhesion energy compared with dry and wet cases (with/without water molecules). This phenomenon is attributed to that salt solution leads to a lower value of density profile of epoxy atoms which indicated less attractive interaction.

Additionally, MD is also used for the interphase of glass fibre–epoxy composite [172] and other composite materials (e.g. ceramic, metal, and cementitious matrix composites). It is worthy to point out that, in most of the MD simulation of fibre/polymer-based matrix interface, the materials of fibres focus on the carbon or glass (mainly content is SiO_2) [172], which have relatively simple molecular structure in the comparison of plant-based or animal-based natural fibres having a hierarchical structure consisting of several macromolecular compounds such as cellulose, hemicellulose, lignin in plant-based fibres and cuticle, chitin in animal-based fibres. Due to the simple molecular structure of carbon or glass fibres, their MD simulation can be built at the several nanometre scale. However, in the case of plant-based fibre, the dimension of cell wall constituents is generally tens of nanometre, which exceeds the computational capacity of atomistic MD simulations. In order to understand the interface between the plant-based fibre and matrix in MD simulation, one method is simplifying the cell wall to the scale of atomistic MD simulation. For example, Tam et al. [167] used cellulose to represent the wood cell wall and performed cellulose–epoxy atomistic MD simulation to confirm that water molecules reduce the adhesion energy of the wood–epoxy interface. Another approach is coarse-grained (CG) MD model which is proposed to simulate the molecular motion at the mesoscale. Briefly, the fundamental principle of CG models is to group cooperative atoms together into CG sites and then CG sites interact with each other based on effective potentials [173]. The coarse-grained MD has been applied to simulate the cellulose fibre [174] and chitin [175]. Tam et al. [167] utilized CG model to simulate the interface of epoxy–-wood cell wall and studied the influence of temperature (−5, 20, and 50 °C) on the interfacial fracture energy. The model of the wood cell wall with the structure of cellulose embedded in the hemicellulose, as illustrated in Fig. 47. In the simulation, the epoxy was sheared off the cell wall substrate by applying an external force in the direction parallel to the cellulose. The interfacial fracture energy is calculated by dividing the potential of mean force by interfacial area. According to the simulation results, conformational changes of the epoxy–cell wall interface (obvious deformation of epoxy layer and delamination of cell wall layer) were observed and

unveiled that the temperature can significantly deteriorate the interface of wood–epoxy.

In the simulation methods discussed above, both the finite element method (FEM) and discrete element method (DEM) can be used to establish the interface model for FRP composite from macro, meso, and micro scales. The MD simulation is of great use to present the real interaction in the interface at the atomic and molecular scale. However, the limited simulation scales in time (3×10^{-10} s) and length (smaller than 100 nm), and high requirement of computing efficiency are obstacles to broaden its application.

3. Future developments

In the investigation of fibre/matrix interface, the method to improve the interfacial bonding based on the interface mechanisms is still a key point. Using nanoparticles can enhance the interfacial bonding by various interface mechanisms such as enhancing mechanical interlocking, increasing surface wettability of fibre, and chemical bonding. Nowadays, a "growth" method has gained attention from researchers because it can make nanoparticles grafting more efficient compared with soaking fibres in the solution containing nanoparticles. For example, Yang et al. [176] immersed the sisal fibre coated by Zinc oxide (ZnO) into the aqueous solution of Zinc nitrate ($Zn(NO_3)_2$) to lead the lateral growth of ZnO nanowires on the fibre surface. Yao et al. [177] used the chemical vapour deposition method to achieve the growth of nanocarbon tubes on the carbon fibre surface. This "growth" method currently is utilized in the FRP composite material containing one type of fibre. It needs further investigation to apply the method to the intra-layer hybrid FRP composites which have different fibres in one FRP. Additionally, to achieve the practical application of FRP-nanoparticles in composite materials, the influence of nanoparticles on the interfacial bonding under various conditions (e.g., weathering, ultraviolet and hygrothermal environments) for long-term exposure needs to be investigated both experimentally and theoretically. Further studies can focus on characterizing the chemical or physical changes of the interface with nanoparticles during the exposure and formulating the life predictions consi dering the degradation of fibre–matrix interface with nanoparticles.

In the simulation of the interface, the models considering the influence of nanoparticles need further investigated. For example, the bridge effect of nanoparticles which can increase toughness could be incorporated in the simulation of interface crack propagation. Besides, the influence of nanoparticles on the roughness of fibre surface could be quantified as the friction coefficient and applied in the interface simulation based on friction models. Furthermore, the effect of shape, size and distribution of nanoparticles on the interface need to be considered in the simulation. The molecular dynamics (MD) simulation of the fibre–matrix interface with nanoparticles under various conditions such as weathering and ultraviolet is an interesting aspect for further explorations. Coupling MD simulation, finite element method, and discrete element method could fulfil the multi-scale investigation on the interface and the entire FRP-nanoparticles composite materials.

4. Conclusions

This paper presents a comprehensive review of the interfacial properties of FRP. The interface mechanism and the interfacial properties of FRP are discussed. The methodology for characterisation, and the numerical simulation on the interface and interfacial properties are also introduced. The mechanism of interphase in composite materials includes physical attraction between electrically neutral bodies, molecular entanglement, interdiffusion, chemical bonding, reaction bonding, and mechanical bonding. The final bonding is most likely formed by the combination of some of these mechanisms. The corresponding methodology for interfacial properties (e.g., interfacial shear strength, interlaminar shear strength, and fracture toughness) is introduced in mechanical tests and auxiliary analysis method. The simulations based on FEM, DEM, and molecular dynamics are presented. In the FEM, the continuum damage model, cohesive zone model, friction model, and coupled model are discussed. The future perspectives on the investigation of grafting nanoparticles on the hybrid FRP, the chemical or physical mechanisms of the interface with nanoparticles, and the simulation of interface modified by nanoparticles are discussed.

Declaration of Competing Interest

The authors declare no conflict of interest.

Acknowledgement

The research was financially supported by Fachagentur Nachwachsende Rohstoffe e.V. (FNR, Agency for Renewable Resources) founded by Bundesministerium für Ernährung und Landwirtschaft (BMEL, The Federal Ministry of Food and Agriculture of Germany), under the Grant Award: 22011617, and by Bundesministerium für Bildung und Forschung (BMBF, Federal Ministry of Education and Research of Germany) (Grant No.: 031B0914A). The first author Silu Huang also would like to thank the China Scholarship Council to support her Ph.D. study (No. 201806690002). The gratitude would be extended to anonymous reviewers for their constructive comments during the review process. The authors acknowledge support by the German Research Foundation and the Open Access Publication Funds of the Technische Universität Braunschweig.

REFERENCES

[1] Ye L, Lu Y, Su Z, Meng G. Functionalized composite structures for new generation airframes: a review. Compos Sci Technol 2005;65(9):1436–46. https://doi.org/10.1016/j.compscitech.2004.12.015.

[2] Lu JZ, Wu Q, McNabb HS. Chemical coupling in wood fiber and polymer composites: a review of coupling agents and treatments. Wood Fiber Sci 2000;32(1):88–104.
[3] Shokoohi S, Arefazar A, Khosrokhavar R. Silane coupling agents in polymer-based reinforced composites: a review. J Reinforc Plast Compos 2008;27(5):473–85. https://doi.org/10.1177/0731684407081391.
[4] Xie Y, Hill CAS, Xiao Z, Militz H, Mai C. Silane coupling agents used for natural fiber/polymer composites: a review. Compos Part A Appl Sci Manuf 2010;41(7):806–19. https://doi.org/10.1016/j.compositesa.2010.03.005.
[5] Anbupalani MS, Venkatachalam CD, Rathanasamy R. Influence of coupling agent on altering the reinforcing efficiency of natural fibre-incorporated polymers – a review. J Reinf Plast Compos 2020;39(13–14):520–44. https://doi.org/10.1177/0731684420918937.
[6] Young RJ. Composite micromechanics: from carbon fibres to graphene. In: Beaumont PWR, Soutis C, Hodzic A, editors. Structural integrity and durability of advanced composites. Elsevier; 2015. p. 3–23.
[7] Jassal M, Ghosh S. Aramid fibres-An overview. Indian J Fiber Text Res 2002;27:290–306.
[8] Holbery J, Houston D. Natural-fiber-reinforced polymer composites in automotive applications. JOM 2006;58(11):80–6. https://doi.org/10.1007/s11837-006-0234-2.
[9] Pickering KL, Efendy MA, Le TM. A review of recent developments in natural fibre composites and their mechanical performance. Compos Part A Appl Sci Manuf 2016;83:98–112. https://doi.org/10.1016/j.compositesa.2015.08.038.
[10] Loh K, Tan W. Natural silkworm-epoxy resin composite for high performance application. In: Zakhariev, editor. Metal, ceramic and polymeric composites for various uses. 1st ed. Valley Cottage NY: Scitus Academics LLC; 2016.
[11] Notin L, Viton C, David L, Alcouffe P, Rochas C, Domard A. Morphology and mechanical properties of chitosan fibers obtained by gel-spinning: influence of the dry-jet-stretching step and ageing. Acta Biomater 2006;2(4):387–402. https://doi.org/10.1016/j.actbio.2006.03.003.
[12] Taerwe L, Matthys S. Use of FRP in concrete structures: trends and challenges. In: FIB symposium on concrete engineering for excellence and efficiency, vol. 2. Czech Concrete Society; 2011. p. 1071–84.
[13] Li M, Mu Q, Yan P, Liu L, Guo X. Brucite fibers on performance improvement and mechanism of high-temperature slag cementing slurries. J Adhes Sci Technol 2020;34(1):1–12. https://doi.org/10.1080/01694243.2019.1659568.
[14] Zollo RF. Fiber-reinforced concrete: an overview after 30 years of development. Cement Concr Compos 1997;19(2):107–22. https://doi.org/10.1016/S0958-9465(96)00046-7.
[15] Yan L, Kasal B, Huang L. A review of recent research on the use of cellulosic fibres, their fibre fabric reinforced cementitious, geo-polymer and polymer composites in civil engineering. Compos B Eng 2016;92:94–132. https://doi.org/10.1016/j.compositesb.2016.02.002.
[16] Torres A, De Marco I, Caballero BM, Laresgoiti MF, Legarreta JA, Cabrero MA, et al. Recycling by pyrolysis of thermoset composites: characteristics of the liquid and gaseous fuels obtained. Fuel 2000;79(8):897–902. https://doi.org/10.1016/S0016-2361(99)00220-3.
[17] Selke SE, Hernandez RJ. Packaging: polymers for containers. In: Buschow KHJ, editor. Encyclopedia of materials: science and technology. Amsterdam: Elsevier; 2001. p. 6646–52.
[18] Saldívar-Guerra E, Vivaldo-Lima E. Handbook of polymer synthesis, characterization, and processing. Hoboken, NJ, USA: John Wiley & Sons, Inc; 2013.
[19] Yılmaz ND, Arifuzzaman Khan GM. Flexural behavior of textile-reinforced polymer composites. In: Mechanical and physical testing of biocomposites, fibre-reinforced composites and hybrid composites. Elsevier; 2019. p. 13–42.
[20] Russo P, Acierno D, Simeoli G, Iannace S, Sorrentino L. Flexural and impact response of woven glass fiber fabric/polypropylene composites. Compos B Eng 2013;54:415–21. https://doi.org/10.1016/j.compositesb.2013.06.016.
[21] Crosky A, Soatthiyanon N, Ruys D, Meatherall S, Potter S. Thermoset matrix natural fibre-reinforced composites. In: Natural fibre composites. Elsevier; 2014. p. 233–70.
[22] Campbell FC. Thermoset resins: the glue that holds the strings together. In: Manufacturing processes for advanced composites. Elsevier; 2004. p. 63–101.
[23] Bradley WL, Grant TS. The effect of the moisture absorption on the interfacial strength of polymeric matrix composites. J Mater Sci 1995;30(21):5537–42. https://doi.org/10.1007/BF00351570.
[24] Heshmati M. Durability and long-term performance of adhesively bonded FRP/steel joints. Gothenburg, Sweden: Chalmers University of Technology; 2017.
[25] Kim J-K, Mai Y-W. Introduction. In: Engineered interfaces in fiber reinforced composites. Elsevier; 1998. p. 1–4.
[26] Drzal LT, Rich MJ, Lloyd PF. Adhesion of graphite fibers to epoxy matrices: I. The role of fiber surface treatment. J Adhes 1983;16(1):1–30. https://doi.org/10.1080/00218468308074901.
[27] Sethi S, Ray BC. Environmental effects on fibre reinforced polymeric composites: evolving reasons and remarks on interfacial strength and stability. Adv Colloid Interface Sci 2015;217:43–67. https://doi.org/10.1016/j.cis.2014.12.005.
[28] Kim J-K, Mai Y-W. Characterization of interfaces. In: Engineered interfaces in fiber reinforced composites. Elsevier; 1998. p. 5–41.
[29] Ebnesajjad Sina. Surface treatment of materials for adhesive bonding: theories of adhesion. Amsterdam: Elsevier; William Andrew an imprint of Elsevier; 2014.
[30] Wenzel RN. Surface roughness and contact angle. J Phys Chem 1949;53(9):1466–7. https://doi.org/10.1021/j150474a015.
[31] Gassan J, Gutowski V. Effects of corona discharge and UV treatment on the properties of jute-fibre epoxy composites. Compos Sci Technol 2000;60(15):2857–63. https://doi.org/10.1016/S0266-3538(00)00168-8.
[32] Choi-Yim H, Busch R, Johnson WL. The effect of silicon on the glass forming ability of the Cu47Ti34Zr11Ni8 bulk metallic glass forming alloy during processing of composites. J Appl Phys 1998;83(12):7993–7. https://doi.org/10.1063/1.367981.
[33] Wolff D, Geiger S, Ding P, Staehle HJ, Frese C. Analysis of the interdiffusion of resin monomers into pre-polymerized fiber-reinforced composites. Dent Mater 2012;28(5):541–7. https://doi.org/10.1016/j.dental.2011.12.001.
[34] Sethi S, Rathore DK, Ray BC. Effects of temperature and loading speed on interface-dominated strength in fibre/polymer composites: an evaluation for in-situ environment. Mater Des (1980-2015) 2015;65:617–26. https://doi.org/10.1016/j.matdes.2014.09.053.
[35] Hays DA. Role of electrostatics in adhesion. In: Lee L-H, editor. Fundamentals of adhesion. Cham: Springer International Publishing; 1991. p. 249–78.
[36] Petrie EM. Adhesive bonding of textiles: principles, types of adhesive and methods of use. In: Jones I, Stylios G, editors. Joining textiles: principles and applications. Oxford: Woodhead Publishing Limited in association with the Textile Institute; 2013. p. 225–74.
[37] Han HC, Gong XL, Zhou M, Li C, Yang HB. A study about silane modification and interfacial ultraviolet aging of hemp

fiber reinforced polypropylene composites. Polym Compos 2021;40:446. https://doi.org/10.1002/pc.26000.
[38] Pape PG, Plueddemann EP. Methods for improving the performance of silane coupling agents. J Adhes Sci Technol 1991;5(10):831–42. https://doi.org/10.1163/156856191X00242.
[39] Zhou Y, Fan M, Chen L. Interface and bonding mechanisms of plant fibre composites: an overview. Compos B Eng 2016;101:31–45. https://doi.org/10.1016/j.compositesb.2016.06.055.
[40] Chawla N, Chawla KK. Interface. In: Chawla N, Chawla KK, editors. Metal matrix composites. New York, NY: Springer New York; 2013. p. 99–119.
[41] Chawla N, Chawla KK. Monotonic behavior. In: Chawla N, Chawla KK, editors. Manufacturing processes for advanced composites//metal matrix composites. New York, NY: Elsevier; Springer New York; 2004//2013. p. 163–225.
[42] Liu D, Song J, Anderson DP, Chang PR, Hua Y. Bamboo fiber and its reinforced composites: structure and properties. Cellulose 2012;19(5):1449–80. https://doi.org/10.1007/s10570-012-9741-1.
[43] Sarker F, Karim N, Afroj S, Koncherry V, Novoselov KS, Potluri P. High-performance graphene-based natural fiber composites. ACS Appl Mater Interfaces 2018;10(40):34502–12. https://doi.org/10.1021/acsami.8b13018.
[44] Chen J, Huang Z, Lv W, Wang C. Graphene oxide decorated sisal fiber/MAPP modified PP composites: toward high-performance biocomposites. Polym Compos 2018;39:E113–21. https://doi.org/10.1002/pc.24433.
[45] Javanshour F, Ramakrishnan K, Layek RK, Laurikainen P, Prapavesis A, Kanerva M, et al. Effect of graphene oxide surface treatment on the interfacial adhesion and the tensile performance of flax epoxy composites. Compos Appl Sci Manuf 2021;142(9):106270. https://doi.org/10.1016/j.compositesa.2020.106270.
[46] Liu W, Huang J, Wang N, Lei S. The influence of moisture content on the interfacial properties of natural palm fiber–matrix composite. Wood Sci Technol 2015;49(2):371–87. https://doi.org/10.1007/s00226-015-0702-3.
[47] Oushabi A, Sair S, Oudrhiri Hassani F, Abboud Y, Tanane O, El Bouari A. The effect of alkali treatment on mechanical, morphological and thermal properties of date palm fibers (DPFs): study of the interface of DPF–Polyurethane composite. S Afr J Chem Eng 2017;23:116–23. https://doi.org/10.1016/j.sajce.2017.04.005.
[48] Haameem JAM, Abdul Majid MS, Afendi M, Marzuki HFA, Fahmi I, Gibson AG. Mechanical properties of Napier grass fibre/polyester composites. Compos Struct 2016;136:1–10. https://doi.org/10.1016/j.compstruct.2015.09.051.
[49] Zhao FM, Takeda N. Effect of interfacial adhesion and statistical fiber strength on tensile strength of unidirectional glass fiber/epoxy composites. Part I: experiment results. Compos Part A Appl Sci Manuf 2000;31(11):1203–14. https://doi.org/10.1016/S1359-835X(00)00085-3.
[50] Ferreira SR, Pepe M, Martinelli E, de Andrade Silva F, Toledo Filho RD. Influence of natural fibers characteristics on the interface mechanics with cement based matrices. Compos B Eng 2018;140:183–96. https://doi.org/10.1016/j.compositesb.2017.12.016.
[51] Ghaffari S, Seon G, Makeev A. In-situ SEM based method for assessing fiber-matrix interface shear strength in CFRPs. Mater Des 2021;197(11):109242. https://doi.org/10.1016/j.matdes.2020.109242.
[52] Test method for in-plane shear response of polymer matrix composite materials by tensile test of a 45 laminate. 2018. https://doi.org/10.1520/D3518_D3518M-18.
[53] ISO 14129:1997 Fibre reinforced plastic composites – Determination of the in-plane shear stress/shear strain response, including the in-plane shear modulus and strength, by the ±45° tension test method. 1997. https://doi.org/10.31030/7433963.
[54] ASTM D 2344. Test method for short-beam strength of polymer matrix composite materials and their laminates. West Conshohocken, PA: ASTM International. https://doi.org/10.1520/D2344_D2344M-16.
[55] ISO 14130:1998: fibre-reinforced plastic composites – determinations of apparent laminar shear strength by short-beam method. 1998. https://doi.org/10.31030/7433990.
[56] ASTM D 5528. Test method for mode I interlaminar fracture toughness of unidirectional fiber-reinforced polymer matrix composites. West Conshohocken, PA: ASTM International. https://doi.org/10.1520/D5528-13.
[57] ISO 15024:2001-12: fibre-reinforced plastic composites – determination of mode I interlaminar fracture toughness, GIC, for unidirectionally reinforced materials.
[58] ASTM D 7905. Test method for determination of the mode II interlaminar fracture toughness of unidirectional fiber-reinforced polymer matrix composites. West Conshohocken, PA: ASTM International. https://doi.org/10.1520/D7905_D7905M-19E01.
[59] ISO 15114:2014. Fibre-reinforced plastic composites – determination of the mode II fracture resistance for unidirectionally reinforced materials using the calibrated end-loaded split (C-ELS) test and an effective crack length approach.
[60] Cooper CA, Cohen SR, Barber AH, Wagner HD. Detachment of nanotubes from a polymer matrix. Appl Phys Lett 2002;81(20):3873–5. https://doi.org/10.1063/1.1521585.
[61] Barber AH, Cohen SR, Kenig S, Wagner HD. Interfacial fracture energy measurements for multi-walled carbon nanotubes pulled from a polymer matrix. Compos Sci Technol 2004;64(15):2283–9. https://doi.org/10.1016/j.compscitech.2004.01.023.
[62] Zhang Y, Li Y, Ma H, Yu T. Tensile and interfacial properties of unidirectional flax/glass fiber reinforced hybrid composites. Compos Sci Technol 2013;88:172–7. https://doi.org/10.1016/j.compscitech.2013.08.037.
[63] Saidane EH, Scida D, Pac M-J, Ayad R. Mode-I interlaminar fracture toughness of flax, glass and hybrid flax-glass fibre woven composites: failure mechanism evaluation using acoustic emission analysis. Polym Test 2019;75:246–53. https://doi.org/10.1016/j.polymertesting.2019.02.022.
[64] Prasad V, Sekar K, Varghese S, Joseph MA. Enhancing Mode I and Mode II interlaminar fracture toughness of flax fibre reinforced epoxy composites with nano TiO_2. Compos Part A Appl Sci Manuf 2019;124:105505. https://doi.org/10.1016/j.compositesa.2019.105505.
[65] Le Duigou A, Davies P, Baley C. Macroscopic analysis of interfacial properties of flax/PLLA biocomposites. Compos Sci Technol 2010;70(11):1612–20. https://doi.org/10.1016/j.compscitech.2010.06.001.
[66] Almansour FA, Dhakal HN, Zhang ZY. Effect of water absorption on Mode I interlaminar fracture toughness of flax/basalt reinforced vinyl ester hybrid composites. Compos Struct 2017;168:813–25. https://doi.org/10.1016/j.compstruct.2017.02.081.
[67] Kim J-K, Mai Y-W. Measurements of interface/interlaminar properties. In: Kim Jang-Kyo, Mai Yiu-Wing, Mai Yiu-Wing, editors. Engineered interfaces in fiber reinforced composites. Elsevier; 1998. p. 43–92.
[68] Huang Y, Young RJ. Analysis of the fragmentation test for carbon-fibre/epoxy model composites by means of Raman

spectroscopy. Compos Sci Technol 1994;52(4):505–17. https://doi.org/10.1016/0266-3538(94)90033-7.
[69] Tsirka K, Tzounis L, Avgeropoulos A, Liebscher M, Mechtcherine V, Paipetis AS. Optimal synergy between micro and nano scale: hierarchical all carbon composite fibers for enhanced stiffness, interfacial shear strength and Raman strain sensing. Compos Sci Technol 2018;165:240–9. https://doi.org/10.1016/j.compscitech.2018.07.003.
[70] Seghini MC, Touchard F, Sarasini F, Chocinski-Arnault L, Mellier D, Tirillò J. Interfacial adhesion assessment in flax/epoxy and in flax/vinylester composites by single yarn fragmentation test: correlation with micro-CT analysis. Compos Part A Appl Sci Manuf 2018;113(7):66–75. https://doi.org/10.1016/j.compositesa.2018.07.015.
[71] Kelly A. Interface effects and the work of fracture of a fibrous composite. Proc R Soc Lond A 1970;319(1536):95–116. https://doi.org/10.1098/rspa.1970.0168.
[72] Boll DJ, Jensen RM, Cordner L, Bascom WD. Compression behavior of single carbon filaments embedded in an epoxy polymer. J Compos Mater 1990;24(2):208–19. https://doi.org/10.1177/002199839002400205.
[73] Budiman BA, Suharto D, Kishimoto K, Triawan F, Takahashi K, Inaba K. Single fiber fragmentation test for evaluating fiber-matrix interfacial strength: testing procedure and its improvements. In: Seminar Nasional Tahunan Teknik Mesin XV (SNTTM XV); 2016 Oct 5.
[74] Khan Z, Yousif BF, Islam M. Fracture behaviour of bamboo fiber reinforced epoxy composites. Compos B Eng 2017;116:186–99. https://doi.org/10.1016/j.compositesb.2017.02.015.
[75] Feih S, Wonsyld K, Minzari D, Westermann P, Lilholt H. Testing procedure for the single fiber fragmentation test.
[76] Rich MJ, Drzal LT, Hunston D, Holmes G, McDonough W. Round robin assessment of the single fiber fragmentation test. In: The American Society for Composites 17th Technical Conference; 2002 Oct 21.
[77] Krishnan P. Evaluation and methods of interfacial properties in fiber-reinforced composites. In: Mechanical and physical testing of biocomposites, fibre-reinforced composites and hybrid composites. Elsevier; 2019. p. 343–85.
[78] Hsueh C-H. Fibre pullout against push-down for fibre-reinforced composites with frictional interfaces. J Mater Sci 1990;25(2):811–7. https://doi.org/10.1007/BF03372167.
[79] ASTM D 3518. Standard test method for in-plane shear response of polymer matrix composite materials by tensile test of a ±45° laminate. West Conshohocken, PA: ASTM International. https://doi.org/10.1520/D3518_D3518M-18.
[80] ASTM D 3039. Test method for tensile properties of polymer matrix composite materials. West Conshohocken, PA: ASTM International. https://doi.org/10.1520/D3039_D3039M-17.
[81] ISO 19927:2018, Fibre-reinforced plastic composites. Determination of inter-laminar strength and modulus by double beam shear test.
[82] Merzkirch M, Foecke T. Investigation of the interlaminar shear properties of fiber-reinforced polymers via flexural testing using digital image correlation. Matls Perf Charact 2020;9(5):20190206. https://doi.org/10.1520/mpc20190206.
[83] Kim WC, Dharan CKH. Analysis of five-point bending for determination of the interlaminar shear strength of unidirectional composite materials. Compos Struct 1995;30(3):241–51. https://doi.org/10.1016/0263-8223(94)00015-8.
[84] Johnson WS, Masters JE, O'Brien TK, Lee SM. An edge crack torsion method for mode III delamination fracture testing. J Compos Technol Res 1993;15(3):193. https://doi.org/10.1520/CTR10369J.
[85] Ahmadi-Moghadam B, Taheri F. Influence of graphene nanoplatelets on modes I, II and III interlaminar fracture toughness of fiber-reinforced polymer composites. Eng Fract Mech 2015;143:97–107. https://doi.org/10.1016/j.engfracmech.2015.06.026.
[86] Mehrabadi FA, Khoshravan M. Mode III interlaminar fracture and damage characterization in woven fabric-reinforced glass/epoxy composite laminates. J Compos Mater 2013;47(13):1583–92. https://doi.org/10.1177/0021998312449770.
[87] de Morais AB, Pereira AB, de Moura MFSF, Magalhães AG. Mode III interlaminar fracture of carbon/epoxy laminates using the edge crack torsion (ECT) test. Compos Sci Technol 2009;69(5):670–6. https://doi.org/10.1016/j.compscitech.2008.12.019.
[88] Drzal LT, Madhukar M. Fibre-matrix adhesion and its relationship to composite mechanical properties. J Mater Sci 1993;28(3):569–610. https://doi.org/10.1007/BF01151234.
[89] Sivakumar D, Ng LF, Zalani NFM, Selamat MZ, Ab Ghani AF, Fadzullah SHSM. Influence of kenaf fabric on the tensile performance of environmentally sustainable fibre metal laminates. Alex Eng J 2018;57(4):4003–8. https://doi.org/10.1016/j.aej.2018.02.010.
[90] Cui W, Wisnom MR, Jones M. Effect of specimen size on interlaminar shear strength of unidirectional carbon fibre-epoxy. Compos Eng 1994;4(3):299–307. https://doi.org/10.1016/0961-9526(94)90080-9.
[91] Inkson BJ. Scanning electron microscopy (SEM) and transmission electron microscopy (TEM) for materials characterization. In: Hübschen Gerhard, Altpeter Iris, Tschuncky Ralf, Herrmann Hans-Georg, editors. Materials characterization using nondestructive evaluation (NDE) methods. Elsevier; 2016. p. 17–43.
[92] Sair S, Oushabi A, Kammouni A, Tanane O, Abboud Y, Oudrhiri Hassani F, et al. Effect of surface modification on morphological, mechanical and thermal conductivity of hemp fiber: characterization of the interface of hemp –Polyurethane composite. Case Stud Therm Eng 2017;10(7):550–9. https://doi.org/10.1016/j.csite.2017.10.012.
[93] Valantin C, Benoit R, D MP, Lacroix F, Gomez E, Phalip P, et al. SEM-EDX analysis and TOF-SIMS 3D imaging of a textile/rubber interface undergoing fatigue loading. Appl Surf Sci 2016;360:623–33. https://doi.org/10.1016/j.apsusc.2015.11.027.
[94] Wu Q, Li M, Gu Y, Wang S, Zhang Z. Imaging the interphase of carbon fiber composites using transmission electron microscopy: preparations by focused ion beam, ion beam etching, and ultramicrotomy. Chin J Aeronaut 2015;28(5):1529–38. https://doi.org/10.1016/j.cja.2015.05.005.
[95] Ciprari D, Jacob K, Tannenbaum R. Characterization of polymer nanocomposite interphase and its impact on mechanical properties. Macromolecules 2006;39(19):6565–73. https://doi.org/10.1021/ma0602270.
[96] Nasrollahzadeh M, Atarod M, Sajjadi M, Sajadi SM, Issaabadi Z. Plant-mediated green synthesis of nanostructures: mechanisms, characterization, and applications. In: An introduction to green nanotechnology. Elsevier; 2019. p. 199–322.
[97] Mirau PA. Solid-state NMR characterization of polymer interfaces. In: Webb GA, editor. Modern magnetic resonance. Dordrecht: Springer Netherlands; 2006. p. 575–81.
[98] Aljarrah MT, Abdelal NR. Improvement of the mode I interlaminar fracture toughness of carbon fiber composite reinforced with electrospun nylon nanofiber. Compos B Eng 2019;165:379–85. https://doi.org/10.1016/j.compositesb.2019.01.065.

[99] Prasad V, Joseph MA, Sekar K. Investigation of mechanical, thermal and water absorption properties of flax fibre reinforced epoxy composite with nano TiO_2 addition. Compos Part A Appl Sci Manuf 2018;115:360–70. https://doi.org/10.1016/j.compositesa.2018.09.031.
[100] Wagner HD, Vaia RA. Nanocomposites: issues at the interface. Mater Today 2004;7(11):38–42. https://doi.org/10.1016/S1369-7021(04)00507-3.
[101] Quan Z, Larimore Z, Qin X, Yu J, Mirotznik M, Byun J-H, et al. Microstructural characterization of additively manufactured multi-directional preforms and composites via X-ray micro-computed tomography. Compos Sci Technol 2016;131(10):48–60. https://doi.org/10.1016/j.compscitech.2016.05.015.
[102] Naresh K, Khan KA, Umer R, Cantwell WJ. The use of X-ray computed tomography for design and process modeling of aerospace composites: a review. Mater Des 2020;190(2):108553. https://doi.org/10.1016/j.matdes.2020.108553.
[103] Watanabe T, Takeichi Y, Niwa Y, Hojo M, Kimura M. Nanoscale in situ observations of crack initiation and propagation in carbon fiber/epoxy composites using synchrotron radiation X-ray computed tomography. Compos Sci Technol 2020;197:108244. https://doi.org/10.1016/j.compscitech.2020.108244.
[104] Garcea SC, Wang Y, Withers PJ. X-ray computed tomography of polymer composites. Compos Sci Technol 2018;156:305–19. https://doi.org/10.1016/j.compscitech.2017.10.023.
[105] Goumri M, Venturini JW, Bakour A, Khenfouch M, Baitoul M. Tuning the luminescence and optical properties of graphene oxide and reduced graphene oxide functionnalized with PVA. Appl Phys A 2016;122(3):351. https://doi.org/10.1007/s00339-016-9725-3.
[106] Kim H-I, Han W, Choi W-K, Park S-J, An K-H, Kim B-J. Effects of maleic anhydride content on mechanical properties of carbon fibers-reinforced maleic anhydride-grafted-polypropylene matrix composites. Carbon Lett 2016;20:39–46. https://doi.org/10.5714/CL.2016.20.039.
[107] Mwaikambo LY, Ansell MP. Chemical modification of hemp, sisal, jute, and kapok fibers by alkalization. J Appl Polym Sci 2002;84(12):2222–34. https://doi.org/10.1002/app.10460.
[108] Arrakhiz FZ, El Achaby M, Kakou AC, Vaudreuil S, Benmoussa K, Bouhfid R, et al. Mechanical properties of high density polyethylene reinforced with chemically modified coir fibers: impact of chemical treatments. Mater Des (1980-2015) 2012;37:379–83. https://doi.org/10.1016/j.matdes.2012.01.020.
[109] Sudhakara P, Jagadeesh D, Wang Y, Prasad CV, Devi APK, Balakrishnan G, et al. Fabrication of borassus fruit lignocellulose fiber/PP composites and comparison with jute, sisal and coir fibers. Carbohydr Polym 2013;98(1):1002–10. https://doi.org/10.1016/j.carbpol.2013.06.080.
[110] Xia X, Liu W, Zhou L, Hua Z, Liu H, He S. Modification of flax fiber surface and its compatibilization in polylactic acid/flax composites. Iran Polym J 2016;25(1):25–35. https://doi.org/10.1007/s13726-015-0395-3.
[111] Li J, Qiao Y, Li D, Zhang S, Liu P. Improving interfacial and mechanical properties of glass fabric/polyphenylene sulfide composites via grafting multi-walled carbon nanotubes. RSC Adv 2019;9(56):32634–43. https://doi.org/10.1039/C9RA05805B.
[112] Wang A, Xian G, Li H. Effects of fiber surface grafting with nano-clay on the hydrothermal ageing behaviors of flax fiber/epoxy composite plates. Polymers (Basel) 2019;11(8). https://doi.org/10.3390/polym11081278.
[113] Nakajima K, Wang D, Nishi T. AFM characterization of polymer nanocomposites. In: Mittal V, editor. Characterization techniques for polymer nanocomposites. Weinheim, Germany: Wiley-VCH Verlag GmbH & Co. KGaA; 2012. p. 185–228.
[114] Choudhury NR, Kannan AG, Dutta NK. Novel nanocomposites and hybrids for lubricating coating applications. In: Friedrich K, Schlarb AK, editors. Tribology of polymeric nanocomposites: friction and wear of bulk materials and coatings. Oxford: Elsevier; 2008. p. 501–42.
[115] Monclus MA, Young TJ, Di Maio D. AFM indentation method used for elastic modulus characterization of interfaces and thin layers. J Mater Sci 2010;45(12):3190–7. https://doi.org/10.1007/s10853-010-4326-6.
[116] Cech V, Palesch E, Lukes J. The glass fiber–polymer matrix interface/interphase characterized by nanoscale imaging techniques. Compos Sci Technol 2013;83:22–6. https://doi.org/10.1016/j.compscitech.2013.04.014.
[117] Wang Y, Hahn TH. AFM characterization of the interfacial properties of carbon fiber reinforced polymer composites subjected to hygrothermal treatments. Compos Sci Technol 2007;67(1):92–101. https://doi.org/10.1016/j.compscitech.2006.03.030.
[118] Molazemhosseini A, Tourani H, Naimi-Jamal MR, Khavandi A. Nanoindentation and nanoscratching responses of PEEK based hybrid composites reinforced with short carbon fibers and nano-silica. Polym Test 2013;32(3):525–34. https://doi.org/10.1016/j.polymertesting.2013.02.001.
[119] Enrique-Jimenez P, Quiles-Díaz S, Salavagione HJ, Fernández-Blázquez JP, Monclús MA, Guzman de Villoria R, et al. Nanoindentation mapping of multiscale composites of graphene-reinforced polypropylene and carbon fibres. Compos Sci Technol 2019;169:151–7. https://doi.org/10.1016/j.compscitech.2018.11.009.
[120] Cross WM, Kjerengtroen L, Kellar JJ. Interphase variation in silane-treated glass-fiber-reinforced epoxy composites. J Adhes Sci Technol 2005;19(3–5):279–90. https://doi.org/10.1163/1568561054352649.
[121] Gao S-L, Mäder E. Characterisation of interphase nanoscale property variations in glass fibre reinforced polypropylene and epoxy resin composites. Compos Part A Appl Sci Manuf 2002;33(4):559–76. https://doi.org/10.1016/S1359-835X(01)00134-8.
[122] Li Q, Li Y, Zhou L. Nanoscale evaluation of multi-layer interfacial mechanical properties of sisal fiber reinforced composites by nanoindentation technique. Compos Sci Technol 2017;152(3–4):211–21. https://doi.org/10.1016/j.compscitech.2017.09.030.
[123] Konstantopoulos G, Koumoulos EP, Charitidis CA. Classification of mechanism of reinforcement in the fiber-matrix interface: application of Machine Learning on nanoindentation data. Mater Des 2020;192(1):108705. https://doi.org/10.1016/j.matdes.2020.108705.
[124] Fritz NK, Kopp R, Nason AK, Ni X, Lee J, Stein IY, et al. New interlaminar features and void distributions in advanced aerospace-grade composites revealed via automated algorithms using micro-computed tomography. Compos Sci Technol 2020;193:108132. https://doi.org/10.1016/j.compscitech.2020.108132.
[125] Guo Q, Yao W, Li W, Gupta N. Constitutive models for the structural analysis of composite materials for the finite element analysis: a review of recent practices. Compos Struct 2021;260(1):113267. https://doi.org/10.1016/j.compstruct.2020.113267.
[126] Springer M, Turon A, Pettermann HE. A thermo–mechanical cyclic cohesive zone model for variable amplitude loading and mixed–mode behavior. Int J Solid Struct 2019;159(2):257–71. https://doi.org/10.1016/j.ijsolstr.2018.10.004.

[127] de Moura MFSF, Chousal JAG. Cohesive and continuum damage models applied to fracture characterization of bonded joints. Int J Mech Sci 2006;48(5):493–503. https://doi.org/10.1016/j.ijmecsci.2005.12.008.
[128] Tserpes KI, Koumpias AS. Comparison between a cohesive zone model and a continuum damage model in predicting mode-I fracture behavior of adhesively bonded joints. Comput Model Eng Sci 2014;83(2):169–82. https://doi.org/10.32604/cmes.2012.083.169.
[129] Babaei R, Farrokhabadi A. Prediction of debonding growth in two-dimensional RVEs using an extended interface element based on continuum damage mechanics concept. Compos Struct 2020;238:111981. https://doi.org/10.1016/j.compstruct.2020.111981.
[130] Wang L, Zheng C, Luo H, Wei S, Wei Z. Continuum damage modeling and progressive failure analysis of carbon fiber/epoxy composite pressure vessel. Compos Struct 2015;134(3):475–82. https://doi.org/10.1016/j.compstruct.2015.08.107.
[131] Maimí P, Camanho PP, Mayugo JA, Dávila CG. A continuum damage model for composite laminates: part I – constitutive model. Mech Mater 2007;39(10):897–908. https://doi.org/10.1016/j.mechmat.2007.03.005.
[132] Maimí P, Camanho PP, Mayugo JA, Dávila CG. A continuum damage model for composite laminates: part II – computational implementation and validation. Mech Mater 2007;39(10):909–19. https://doi.org/10.1016/j.mechmat.2007.03.006.
[133] González EV, Maimí P, Camanho PP, Turon A, Mayugo JA. Simulation of drop-weight impact and compression after impact tests on composite laminates. Compos Struct 2012;94(11):3364–78. https://doi.org/10.1016/j.compstruct.2012.05.015.
[134] Maimí P, Mayugo JA, Camanho PP. A three-dimensional damage model for transversely isotropic composite laminates. J Compos Mater 2008;42(25):2717–45. https://doi.org/10.1177/0021998308094965.
[135] Salavatian M, Smith LV. An investigation of matrix damage in composite laminates using continuum damage mechanics. Compos Struct 2015;131(3):565–73. https://doi.org/10.1016/j.compstruct.2015.06.012.
[136] Melro AR, Camanho PP, Andrade Pires FM, Pinho ST. Numerical simulation of the non-linear deformation of 5-harness satin weaves. Comput Mater Sci 2012;61:116–26. https://doi.org/10.1016/j.commatsci.2012.04.010.
[137] Sun X, Tong L, Wood MDK, Mai Y-W. Effect of stitch distribution on mode I delamination toughness of laminated DCB specimens. Compos Sci Technol 2004;64(7–8):967–81. https://doi.org/10.1016/j.compscitech.2003.07.004.
[138] Iwahori Y, Nakane K, Watanabe N. DCB test simulation of stitched CFRP laminates using interlaminar tension test results. Compos Sci Technol 2009;69(14):2315–22. https://doi.org/10.1016/j.compscitech.2008.12.018.
[139] Tan KT, Watanabe N, Sano M, Iwahori Y, Hoshi H. Interlaminar fracture toughness of vectran-stitched composites - experimental and computational analysis. J Compos Mater 2010;44(26):3203–29. https://doi.org/10.1177/0021998310369581.
[140] Ravandi M, Teo WS, Yong MS, Tay TE. Prediction of Mode I interlaminar fracture toughness of stitched flax fiber composites. J Mater Sci 2018;53(6):4173–88. https://doi.org/10.1007/s10853-017-1859-y.
[141] Yamanaka T, Ghiasi H, Heidari-Rarani M, Lessard L, Feret V, Hubert P. Multiscale finite element analysis of mode I delamination growth in a fabric composite. Compos Struct 2015;133(14):157–65. https://doi.org/10.1016/j.compstruct.2015.07.094.
[142] Abdel Wahab MM. Simulating mode I fatigue crack propagation in adhesively-bonded composite joints. In: Fatigue and fracture of adhesively-bonded composite joints. Elsevier; 2015. p. 323–44.
[143] Sun CT, Jin Z-H. Cohesive zone model. In: Sun CT, Jin Z-H, editors. Fracture mechanics. Elsevier; 2012. p. 227–46.
[144] Heidari-Rarani M, Ghasemi AR. Appropriate shape of cohesive zone model for delamination propagation in ENF specimens with R-curve effects. Theor Appl Fract Mech 2017;90:174–81. https://doi.org/10.1016/j.tafmec.2017.04.009.
[145] Jia Y, Yan W, Liu H-Y. Carbon fibre pullout under the influence of residual thermal stresses in polymer matrix composites. Comput Mater Sci 2012;62:79–86. https://doi.org/10.1016/j.commatsci.2012.05.019.
[146] Madadi H, Naghdinasab M, Farrokhabadi A. Numerical investigation of matrix cracking propagation in cross-ply laminated composites subjected to three-point bending load using concurrent multiscale model. Fatigue Fract Eng Mater Struct 2020;43(6):1159–69. https://doi.org/10.1111/ffe.13186.
[147] Low KO, Teng SM, Johar M, Israr HA, Wong KJ. Mode I delamination behaviour of carbon/epoxy composite at different displacement rates. Compos B Eng 2019;176:107293. https://doi.org/10.1016/j.compositesb.2019.107293.
[148] Aveiga D, Ribeiro ML. A delamination propagation model for fiber reinforced laminated composite materials. Math Probl Eng 2018;2018(3):1–9. https://doi.org/10.1155/2018/1861268.
[149] Pike MG, Oskay C. XFEM modeling of short microfiber reinforced composites with cohesive interfaces. Finite Elem Anal Des 2015;106:16–31. https://doi.org/10.1016/j.finel.2015.07.007.
[150] Zhuang F, Chen P, Arteiro A, Camanho PP. Mesoscale modelling of damage in half-hole pin bearing composite laminate specimens. Compos Struct 2019;214:191–213. https://doi.org/10.1016/j.compstruct.2019.01.062.
[151] Camanho PP, Bessa MA, Catalanotti G, Vogler M, Rolfes R. Modeling the inelastic deformation and fracture of polymer composites – part II: smeared crack model. Mech Mater 2013;59:36–49. https://doi.org/10.1016/j.mechmat.2012.12.001.
[152] Zhuang F, Arteiro A, Furtado C, Chen P, Camanho PP. Mesoscale modelling of damage in single- and double-shear composite bolted joints. Compos Struct 2019;226(2):111210. https://doi.org/10.1016/j.compstruct.2019.111210.
[153] Alfano G, Sacco E. Combining interface damage and friction in a cohesive-zone model. Int J Numer Methods Eng 2006;68(5):542–82. https://doi.org/10.1002/nme.1728.
[154] Sugiman S, Ahmad H. Comparison of cohesive zone and continuum damage approach in predicting the static failure of adhesively bonded single lap joints. J Adhes Sci Technol 2017;31(5):552–70. https://doi.org/10.1080/01694243.2016.1222048.
[155] Tsai JH, Patra A, Wetherhold R. Finite element simulation of shaped ductile fiber pullout using a mixed cohesive zone/friction interface model. Compos Part A Appl Sci Manuf 2005;36(6):827–38. https://doi.org/10.1016/j.compositesa.2004.10.025.
[156] Zhi C, Long H, Miao M. Influence of microbond test parameters on interfacial shear strength of fiber reinforced polymer-matrix composites. Compos Part A Appl Sci Manuf 2017;100:55–63. https://doi.org/10.1016/j.compositesa.2017.05.004.
[157] Nian G, Li Q, Xu Q, Qu S. A cohesive zone model incorporating a Coulomb friction law for fiber-reinforced composites. Compos Sci Technol 2018;157(13):195–201. https://doi.org/10.1016/j.compscitech.2018.01.037.

[158] Lin G, Geubelle PH, Sottos NR. Simulation of fiber debonding with friction in a model composite pushout test. Int J Solid Struct 2001;38(46–47):8547–62. https://doi.org/10.1016/S0020-7683(01)00085-3.
[159] Chen X, Beyerlein IJ, Brinson LC. Curved-fiber pull-out model for nanocomposites. Part 1: bonded stage formulation. Mech Mater 2009;41(3):279–92. https://doi.org/10.1016/j.mechmat.2008.12.004.
[160] Chen X, Beyerlein IJ, Brinson LC. Curved-fiber pull-out model for nanocomposites. Part 2: interfacial debonding and sliding. Mech Mater 2009;41(3):293–307. https://doi.org/10.1016/j.mechmat.2008.12.002.
[161] Sliseris J, Yan L, Kasal B. Numerical modelling of flax short fibre reinforced and flax fibre fabric reinforced polymer composites. Compos B Eng 2016;89:143–54. https://doi.org/10.1016/j.compositesb.2015.11.038.
[162] Ismail Y, Sheng Y, Yang D, Ye J. Discrete element modelling of unidirectional fibre-reinforced polymers under transverse tension. Compos B Eng 2015;73:118–25. https://doi.org/10.1016/j.compositesb.2014.12.024.
[163] Lisjak A, Grasselli G. A review of discrete modeling techniques for fracturing processes in discontinuous rock masses. J Rock Mech Geotech Eng 2014;6(4):301–14. https://doi.org/10.1016/j.jrmge.2013.12.007.
[164] Adcock SA, McCammon JA. Molecular dynamics: survey of methods for simulating the activity of proteins. Chem Rev 2006;106(5):1589–615. https://doi.org/10.1021/cr040426m.
[165] Li Y, Wang Q, Wang S. A review on enhancement of mechanical and tribological properties of polymer composites reinforced by carbon nanotubes and graphene sheet: molecular dynamics simulations. Compos B Eng 2019;160:348–61. https://doi.org/10.1016/j.compositesb.2018.12.026.
[166] Xiong QL, Meguid SA. Atomistic investigation of the interfacial mechanical characteristics of carbon nanotube reinforced epoxy composite. Eur Polym J 2015;69:1–15. https://doi.org/10.1016/j.eurpolymj.2015.05.006.
[167] Tam L-h, Zhou A, Yu Z, Qiu Q, Lau D. Understanding the effect of temperature on the interfacial behavior of CFRP-wood composite via molecular dynamics simulations. Compos B Eng 2017;109:227–37. https://doi.org/10.1016/j.compositesb.2016.10.030.
[168] Xiao Y, Xian G. Effects of moisture ingress on the bond between carbon fiber and epoxy resin investigated with molecular dynamics simulation. Polym Compos 2018;39(S4):E2074–83. https://doi.org/10.1002/pc.24459.
[169] Ansari R, Rouhi S, Ajori S. On the interfacial properties of polymers/functionalized single-walled carbon nanotubes. Braz J Phys 2016;46(3):361–9. https://doi.org/10.1007/s13538-016-0410-y.
[170] Rouhi S. Molecular dynamics simulation of the adsorption of polymer chains on CNTs, BNNTs and GaNNTs. Fibers Polym 2016;17(3):333–42. https://doi.org/10.1007/s12221-016-5676-8.
[171] Tam L-h, He L, Wu C. Molecular dynamics study on the effect of salt environment on interfacial structure, stress, and adhesion of carbon fiber/epoxy interface. Compos Interfaces 2019;26(5):431–47. https://doi.org/10.1080/09276440.2018.1506901.
[172] Stoffels MT, Staiger MP, Bishop CM. Reduced interfacial adhesion in glass fibre-epoxy composites due to water absorption via molecular dynamics simulations. Compos Part A Appl Sci Manuf 2019;118:99–105. https://doi.org/10.1016/j.compositesa.2018.12.018.
[173] Mani S, Cosgrove DJ, Voth GA. Anisotropic motions of fibrils dictated by their orientations in the lamella: a coarse-grained model of a plant cell wall. J Phys Chem B 2020;124(17):3527–39. https://doi.org/10.1021/acs.jpcb.0c01697.
[174] Glass DC, Moritsugu K, Cheng X, Smith JC. REACH coarse-grained simulation of a cellulose fiber. Biomacromolecules 2012;13(9):2634–44. https://doi.org/10.1021/bm300460f.
[175] Cui J, Yu Z, Lau D. Effect of acetyl group on mechanical properties of chitin/chitosan nanocrystal: a molecular dynamics study. Int J Mol Sci 2016;17(1). https://doi.org/10.3390/ijms17010061.
[176] Yang C, Han R, Nie M, Wang Q. Interfacial reinforcement mechanism in poly(lactic acid)/natural fiber biocomposites featuring ZnO nanowires at the interface. Mater Des 2020;186(12):108332. https://doi.org/10.1016/j.matdes.2019.108332.
[177] Yao Z, Wang C, Lu R, Su S, Qin J, Wang Y, et al. Fracture investigation of functionalized carbon nanotubes-grown carbon fiber fabrics/epoxy composites. Compos Sci Technol 2020;195:108161. https://doi.org/10.1016/j.compscitech.2020.108161.

Miss Silu Huang is a doctoral student at Technical University of Braunschweig. She received the Master of Science and Bachelor of Science from Hefei Technology of University in China. Her research interests include mechanical characterization and long-term durability of hybrid fibre reinforced polymer composites and their FRP-timber hybrid structures.

Dr. Qiuni Fu was awarded PhD degree in the area of composite structures from Nanyang Technological University, Singapore. She received the Master of Science and Bachelor of Civil Engineering from Chongqing University, China. Dr. Fu is a post-doc research fellow at TU Braunschweig. Her research interests include hybrid composite materials and structures, and their life prediction.

Prof. Dr. Libo Yan was awarded PhD degree in the area of fibre reinforced polymer composites and concrete hybrid structures from The University of Auckland, New Zealand. He received the Master of Science in Structural Engineering from Cardiff University with the Distinction award. Presently, Dr. Yan is working as Senior Scientist and Junior Research Group Leader at Fraunhofer Institute for Wood Research WKI and a Professor at Technical University of Braunschweig in Germany. His research interests include fibre reinforced polymer composites, bio-composites, sustainable hybrid composites and materials, durability and life prediction of composite materials and structures, recycling and reuse of different materials.

Prof. Dr. Bohumil Kasal is the Director of Fraunhofer Institute for Wood Research Wilhelm-Klauditz-Institut. Professor Kasal currently also holds a Chair in Organic and Wood-based Construction Materials at the Technische Universität Braunschweig, Germany, and he holds professorships at the Czech Technical University in Prague and the University of Primorska, Slovenia. Professor Kasal's research is focused on wood structures under natural hazard loads, the combination of wood and high-strength fibre reinforced polymer composites, and the in-situ evaluation of wood structures.